THE UNIVERSITY OF HULL

Electronic Structure and Optical Properties of
Sb-Based Self-Assembled Quantum Dots for the Mid-Infrared
Range

being a Thesis submitted for the Degree of
Doctor of Philosophy
in the University of Hull

by

Gik Hong Yeap, BEng. (Lincoln), MSc. (Hull)

JUNE 2009

To my late parents,
my wife, Foong Foong Ooi,
siblings, colleagues, and friends

ACKNOWLEDGEMENT

First of all, I would like to thank my supervisor, Dr. Igor E. Itskevich for guiding and helping me in this research project. Igor has given me a lot of guidance as well as very useful ideas to work on the research project. The interest, enthusiasm and patient that he presented while guiding me in the research is very appreciated. It would be a very difficult task for me without his guidance and help. Second, I would like to thank Professor Stephanie K. Haywood for given me such a great opportunity to further my study in Optoelectronics Group and for her advice and encouragement as my second supervisor.

Next, I would like to thank all the parties involved in the DOMINO project. The involvement in the DOMINO project has provided me the direction and input to this thesis. I am also would like to express my extended appreciation to Dr. Sergey Rybchenko and Dr. Rita Gupta who given me a lot of advice and information regarding the modelling and theories behind the modelling. I also would like to thank Dr. Khue Tian Lai for his advice in doing research and experimental works. Also not forgotten is Dr. Alvin Chin Hon Lim who helped me a lot in the *Matlab* programming, which plays an important role in this research project.

I am also would like to take this opportunity to thank Mr. Peter Carrington and Professor Antony Krier for providing me with their InSb/InAs samples for my experimental work and useful discussions on the SAQD systems. Last but not least, I would like to thank my wife for being very tolerating and supportive throughout my university years. Finally, I would like to thank my late parents and other family members for their support and encouragement.

The guidance, helps, understanding, support and encouragement from all the above mentioned people have provided me the courage and strength to embark on this thesis. Thank you once again.

ABSTRACT

Quantum dots (QDs) are zero-dimensional nanostructures that confined carriers in three dimensions comparable to their de Broglie wavelengths. Therefore, carriers exhibit δ-shaped energy levels and densities of states. Due to their band structure, QD systems show significant advantages as active regions in laser cavities, both in term of lower threshold current densities and better thermal behaviour. The most studied system being InAs/GaAs system but the antimonide-based (Sb-based) material system has been paid much attention due to their potential for optical devices in the 3-5 μm (0.25-0.40 eV) spectral regions and motivated by feasibility of active medium in high speed electronic and long wavelength photonic devices.

In most cases, QDs structures had been obtained with an intrinsic elastic strain field arising from the lattice mismatch between the matrix and QD materials. The strain field plays a very significant role in the fabrication of the self-assembled QDs (SAQDs). Strain fields inside SAQD structures strongly affect the electronic band structure, which in turn, strongly affects the performance of optoelectronic devices. Therefore, knowledge and determination of the strain field in the dots and surrounding matrix is crucial in order to obtain a well ordered SAQDs structure. While knowledge and determination of the electronic structure calculation are necessary for further device modelling to improve the performance of the devices.

Numerical work based on continuum-elasticity based on Finite Element Method (FEM) and standard-deformation-potential theory has been carried out to investigate the effect of strain on the band structure for InSb-based SAQD systems with type-I and type-II band alignment. The effect of elastic anisotropy on both strain distribution and band edges profile is also performed. Next, multi-band $k{\cdot}p$ method is used to model the electronic structure of InSb-based SAQD systems.

The results from the modelling show that the strain-modified band profile of the zinc-blende III-V compound semiconductor SAQDs is not very sensitive to the details of the dot shape and the major governing parameter of the geometry is the aspect ratio of the dot. The modelling results also reveal that there are ***no*** appropriate material

combinations for zinc-blende III-V compound semiconductors that would applicable for the MIR 3-5 μm (0.25-0.40 eV) emission range when type-I band alignment is possible. This leads to the investigation of type-II broken gap $InAs_xSb_{(1-x)}$/InAs SAQDs.

Finally, the optical properties of the InSb-based SAQDs are investigated by means of the photoluminescence (PL) measurement using Fourier transform infrared (FT-IR) spectroscopy. The PL results are analysed and compared to the modelling results.

TABLE OF CONTENT

Acknowledgement		i
Abstract		ii
Table Of Content		iv
		Page
Chapter 1	**Introduction**	**1**
	References	7
Chapter 2	**Background Theory**	**9**
	2.0 Introduction	9
	2.1 Quantum Mechanics	9
	2.2 General Solid State Physics	11
	2.2.1 Bravais Lattice and Zinc-Blende Structure	11
	2.2.2 The Reciprocal Lattice and Brillouin Zone	13
	2.2.3 Energy Band Structure	15
	2.2.4 Bloch Theorem	16
	2.2.5 The ***k·p*** Model	17
	2.2.6 Effective Mass	18
	2.3 General Theory of Semiconductors	19
	2.3.1 III-V Compound Semiconductors	19
	2.3.2 Energy Band Structure of GaAs, GaSb, InAs and InSb	20
	References	22
Chapter 3	**Literature Review**	**23**
	3.0 Introduction	23
	3.1 Semiconductor Heterostructures	23
	3.2 Quantum Confinement in Semiconductors	26
	3.3 Quantum Dots	27
	3.3.1 The Fabrications of QDs	27
	3.4 Sb-Based SAQDs for the Mid-Infrared	29
	3.5 Modelling of SAQDs	31
	References	33
Chapter 4	**Research Methods**	**36**
	4.0 Introduction	36
	4.1 Modelling Methods	36
	4.1.1 Modelling of the Strain Fields	37
	4.1.1.1 Numerical calculation of Strain fields	39
	4.1.1.1.1 2-D Axial Symmetry Model	41
	4.1.1.1.2 3-D Model	42
	4.1.1.2 Analytical Approach of Elasticity Problem	43
	4.1.1.3 Modelling The Lattice Mismatch	44
	4.1.2 Strain Modified Band Profile	45
	4.1.3 Electronic Structure	49
	4.1.3.1 Temperature Dependence Modelling of Electronic Structure	50
	4.2 Sample Growth and Structural Characterisation,	51

4.2.1 Molecular Beam Epitaxy (MBE) 51
4.2.2 Epitaxial Growth Monitoring 54
4.2.3 InSb/GaSb SAQD System Sample Growth and Structural Characterisation 55
4.2.4 InSb/InAs SAQD System Sample Growth and Structural Characterisation 58
4.3 Experimental Study 59
4.3.1 Photoluminescence Measurement 59
4.3.2 Principle Operation of FT-IR PL Measurement 62
4.3.3 FT-IR PL Measurement Procedures 63
4.3.4 Advantages of FT-IR PL Spectroscopy 64
References 66

Chapter 5 Preliminary Study of Strain Distribution and Strain-Modified Band Profile in SAQDs 70
5.0 Introduction 70
5.1 Strain Field Calculation 71
5.1.1 Literature Results 71
5.1.2 2-D Axial Symmetry Model for InSb/GaSb SAQD System 72
5.1.2.1 ANSYS Model 73
5.1.2.2 ANSYS vs Comsol Multiphysics 76
5.1.3 3-Dimensional Model vs 2-Dimensional Model 78
5.1.4 Effects of Anisotropy 79
5.2 Strain Effects on Band edges 80
5.3 Summary 84
References 85

Chapter 6 Important of Aspect Ratio Over Shape in Determining the Quantization Potential of Self-Assembled Zinc-Blende III-V Quantum Dots 86
6.0 Introduction 86
6.1 Ellipsoidal Quantum Dots 87
6.1.1 General Trends in Strain Distribution and Strain-Modified Band Profile for Ellipsoidal QD 88
6.2 Realistic QD Shapes 93
6.2.1 General Trends in Strain Distribution and Strain-Modified Band Profile for Realistic QD Shape 93
6.3 Effect of Wetting Layer 100
6.4 Ellipsoidal Model 102
6.4.1 Growth Plain Orientation 103
6.4.2 Comparison to the Similar-Elasticity Approximation 105
6.5 Application of Ellipsoidal Model 107
6.5.1 InGaSb QD in GaSb Matrix 107
6.5.1.1 Strain and Strain-Modified Band Profile 109
6.5.1.2 Electron/Hole Levels 114
6.5.1.3 Optical Properties 115
6.5.1.4 L-Band Related Transitions in InSb/GaSb SAQD heterostructure 116
6.5.2 InAsSb QD in InP Matrix 117
6.5.3 InAsSb QD in InAs Matrix 117
6.6 Summary 118
References 120

Chapter 7 **Strained Type-II $InAs_xSb_{1-x}$/InAs SAQDs for MIR Applications** **122**
7.0 Introduction 122
7.1 Strain and Strain-Modified Band Profile 123
7.2 Energy Levels 129
7.3 Experimental Results 133
7.3.1 Power Dependent PL 134
7.3.2 Temperature Dependent PL 135
7.4 Summary 139
References 141

Chapter 8 **Conclusions and Future Development of the Model** **142**
8.1 Conclusions 142
8.2 Future Development of the Model 144
References 146

Appendix 1 - Strain Tensor for Oblate Ellipsoid 147
Appendix 2 - List of Publications and Conference Presentations 150

CHAPTER 1

INTRODUCTION

The production and study of quantum dots (QDs) structures is one of the main directions of contemporary semiconductor physics in order to realize novel devices that make use of low-dimensional confinement effects and their unique electronics properties [1]. Nowadays, the growth and characterization of self-assembled semiconductor QDs are of strong interest and much attention has been devoted. The maturation and advancement of epitaxial crystal growth techniques such as Molecular Beam Epitaxy (MBE) [2–4] and Metal-Organic Vapour Phase Epitaxy (MOVPE) [3,4] have led to the ability to fabricate semiconductor-based devices with dimensions so small so that quantum mechanical effects dominate their behaviour. The current epitaxial crystal growth techniques also possess the ability and flexibility to vary the composition, layer thicknesses, doping and strain in the semiconductor heterostructures. This flexibility has enabled the electronic and optical properties of a heterostructure, and subsequently the properties of the device upon which the structure is based, to be tailored for various applications through the 'band structure engineering'.

There are three important approaches in 'band structure engineering' in order to improve the performance in electronic and optical devices; which involve:

(a) alloying of two or more semiconductor,
(b) use of heterostructures to cause quantum confinement, and
(c) built-in strain via lattice mismatched materials.

Alloying enables the band gap and subsequently the optical property of a bulk semiconductor material to be altered. The initial use of heterostructures has led to the realisation of quantum well (QW) structure where the motion of carriers is effectively restricted to a plane. The confinement of carrier along the growth direction in QW resulted in structural, electronic and optical properties that are unique and different from the macroscopic bulk materials.

The ultimate conclusion of the concept of quantum confinement in heterostructures is the quantum dot (QD) heterostructure. In a QD, the carriers are

confined in all three spatial dimensions and hence exhibit an atomic-like energy states and a density of states (DOS) that resembles a series of delta functions. Potential applications therefore include temperature-independent, low threshold current density and high efficiency semiconductor QD devices.

The built-in strain via lattice mismatched materials has enabled the fabrication of QDs by self-assembling Stranski-Krastanow epitaxial growth technique. To date, these self-assembled quantum dots (SAQDs) exhibit the best characteristic as compared to QDs obtained via other methods.

Most of the study of SAQDs heterostructure had concentrated on InAs/GaAs system, which of interest in the near-infrared region. The studies involved both experimental and theoretical studies. The early works can be found in Ref. [1] and references therein, while the recent works can be found in Ref. [5-6] and references therein. These dots have formed the basis of novel generations of optoelectronic devices such as lasers [7-10] and amplifiers [11] for data and telecommunication applications. The lasing wavelength between 1.1-1.5 μm has been achieved with low transparency current density, low internal losses, high output power, high internal quantum efficiency and pulsed operation at room temperature. The advantages of QD amplifier are reduced chirp, larger saturated gain, and no cross gain modulation. High-temperature infrared photodetectors also have been achieved [12-13]. For recent reviews on the advances, challenges, achievements and new physics of the SAQDs devices, see e.g. Ref. [14-18] and references therein.

However, for novel optoelectronic devices such as long wavelength infrared lasers and detectors, the 3-5 μm (0.25-0.40 eV) window of the mid-infrared (MIR) wavelength range is the window of choice for the devices development due to the low CO_2 and H_2O absorption. Therefore, it is desirable to extend the emission wavelength into MIR (3-5 μm) region where the environmental gas sensing, medical diagnostic and military countermeasures find applications [19].

Among the III-V semiconductor compounds, InSb has the smallest bandgaps, which mean applications involving the longest wavelengths of any of the III-V family of semiconductor compounds. Therefore, the Sb-based material system has attracted

much attention due to their potential for optical devices in the 3-5 μm (0.25-0.40 eV) spectral regions.

Sb-based heterostructures grown on GaSb or InAs substrates, exhibit a number of unique possibilities among III-V compound semiconductors in term of band structure engineering because it is the only III-V technology exhibiting inter-band transitions in the MIR region. However, Sb-based compounds remain relatively unexplored in comparison with other III-V compounds. The earliest literature on Sb-based SAQDs dated back around the end of 1995. By analogy with the InAs/GaAs system, most work has been carried out on the InSb/GaSb system [20-27].

Despite being investigated for more than a decade, there is still lack of knowledge on the electronic, optical, morphological, as well as structural properties of Sb-based SAQDs heterostructures. In order to investigate the feasibility of Sb-based SAQDs for MIR nanophotonic devices, a consortium of six multidisciplinary and complementary partners has been established and the project is named DOMINO. The main objective of the project is to develop a model for semiconductor lasers based on SAQDs and use it to investigate or demonstrate the feasibility of type-I Sb-based SAQDs nano-photonic lasers operating continuous-wave at room temperature in the 3-5 μm wavelength range and understand the characteristics of such devices.

As part of the research consortium, we are mainly in charge of the electronic structure modelling and some preliminary device characterisations. The outcomes from these modelling and preliminary characterisations formed the basis of this thesis. The focus of this thesis is on modelling of the strain field and electronic structure of the InSb-based SAQDs and relates them to the optical properties of the dot, investigated by using the photoluminescence (PL) technique. Knowledge of the electronic structure is necessary for theoretical description of the electronic properties of QDs and for fabrication of nano-devices with designed properties. In this work, the finite element method (FEM) is used to model the strain distribution and energy levels of a selection of semiconductor QD structures. The method is initially developed for application in macroscopic engineering structural analysis. Due to its versatility numerical procedure for the solution of partial differential equations (PDEs), it has found applications in a range of other scientific fields including medical research [28,29], geology [30] as well as quantum physics [31,32].

The popularity of FEM is mainly due to:

(a) the ability to handle geometrically complicated domains; where finite differences method often fails,

(b) straightforward error-analysis, and

(c) ease in constructing higher order approximations.

Most finite element analysis is performed numerically, and a range of packages for applying the procedure, including ANSYS, Diffpack, Abacus and Comsol Multiphysics are commercially available. Comsol Multiphysics has been the preferred package for the work presented in this thesis. Comsol Multiphysics features state-of-the-art solvers that address complex problems quickly and accurately. Its intuitive structure is designed to provide ease of use and flexibility. Most phenomena can be easily modelled through the predefined modelling templates. The most important feature of Comsol Multiphysics is that two or more physical phenomenon can be analysed using the same model through the multiphysics-coupling feature. This convenient is accelerated by the advancement and achievement in the computing with more powerful processor and higher memory capacity.

In general, two SAQD systems are being study in detail in this thesis, namely InSb/GaSb and $InAs_xSb_{(1-x)}$/InAs systems. More detailed descriptions about these two systems will be provided later in the relevant chapter. Other material systems such as InAs/GaAs, InAsSb/InP and InGaSb/GaSb are also being considered.

This thesis contains the outcome of the project, including analyses and discussions based on the results. Following the introduction, an overview of basic quantum mechanics and properties of semiconductors is outlined in Chapter 2. The content of this chapter is the preamble to the main subject matter of the whole project and introduces concepts upon which the main theory is based. The relevant literature specific to Sb-based SAQDs is reviewed in Chapter 3. The main focus is on the work being done and theoretical models of the band structure. Other related subjects such as quantum confinement in semiconductor heterostructures and fabrication method of QDs are also reviewed.

Chapter 4 contains the details of the methodology of the theoretical calculations and experimental methods for QDs heterostructures. The strain-field modelling by

using FEM in 2-D axial symmetry as well as 3-D model by using ANSYS and Comsol Multiphysics FEM packages is outlined. The strain-induced band profile calculations based upon model-solid theory and standard-deformation-potential, as well as multi-band strain dependent *k·p* model for electronic structure calculation are presented. Knowledge of the electronic structure is necessary for theoretical description of the electronic properties of QDs and for fabrication of nano-devices with designed properties. This is followed by the description of the samples growth techniques. After that, the PL measurement setup and procedures are outlined. The introduction of Fourier Transform Infrared (FT-IR) Spectroscopy and its principle of operation as well as the advantages of FT-IR spectroscopy are also addressed.

Chapter 5 gives the preliminary comparison of strain fields obtained from ANSYS and Comsol Multiphysics FEM packages as well as 2-D axial symmetry and 3-D models. The main purpose of the studies in this chapter is to validate the modelling method and to determine the reliability of the Comsol Multiphysics FEM package.

The detail strain distribution and the resulting confinement potential for ellipsoid- and other realistic-shaped InAs/GaAs SAQDs of various aspect ratios are analysed as a benchmark model in Chapter 6. The InAs/GaAs SAQDs system is the well studied system so far. Starting with the simplest example of a spherical dot (i.e. ellipsoid of AR=1); then the effect of increasing AR is examined. For comparison, the same trends are analysed for more complicated shapes (i.e. lens-, truncated cone-, and pyramid-shapes). Here, a simple analytical ellipsoidal model is proposed for the characterisation of the quantisation potential of zinc-blende III-V SAQDs. The ellipsoidal model was then applied to several SAQD material combinations in order to determine the systems that would be available for MIR applications. From this study, we found that there are ***no*** appropriate material combinations that would applicable for the MIR 3-5 μm (0.25-0.40 eV) emission range. All of them produce SAQDs with band gap much larger than the MIR 0.25-0.40 eV range, when type-I band alignment is possible. Hence, for use in the MIR-range devices, alternative SAQD designs need to be considered. This leads to the study of type-II system in Chapter 7.

In Chapter 7, we examine the type-II broken-gap $InAs_xSb_{(1-x)}$/InAs SAQDs. Intense PL at the room temperature in the 3.9-4.3 μm (0.29-0.32 eV) wavelength range had been observed. This system would prove extremely useful for MIR applications if

validated by both experimental and theoretical results. Final conclusions, recommendations and suggestion for future development of the model are presented in Chapter 8.

References:

[1] D. Bimberg, M. Grundmann, and N. N. Ledentsov, *Quantum Dot Heterostructures* (John Wiley & Sons, 1999).

[2] S. Franchi, G. Trevisi, L. Seravalli, and P. Frigeri, 2003, Prog. Cryst. Growth Charact. Mat. **47**, 166 (2003).

[3] K. Seshan, *Handbook of Thin Film Deposition Processes and Techniques: Principles, Methods, Equipment and Application*, (UK: William Andrew Inc., 2001).

[4] V. M. Ustinov, A. E. Zhukov, A. Yu. Egorov, and N. A. Maleev, *Quantum Dot Lasers*, (Oxford: Oxford University Press, 2003).

[5] B. A. Joyce, P. C. Kelires, A. G. Naumovets, and D. D. Vvedensky, eds., *Quantum Dots: Fundamentals, Applications and Frontiers*, (Amsterdam: Springer, 2005).

[6] Z. M. Wang, ed., *Self-Assembled Quantum Dots*, (New York: Springer, 2008).

[7] N.N. Ledentsov, A.R. Kovsh, A.E. Zhukov, N.A. Maleev, S.S. Mikhrin, A.P. Vasil'ev, E.S. Semenova, M.V. Maximov, Yu.M. Shernyakov, N.V. Kryzhanovskaya, V.M. Ustinov and D. Bimberg, Electronics Letters **39**, 1126 (2003).

[8] N.N. Ledentsov, A.E. Zhukov, V.M. Ustinov, M.V. Maximov, Yu.M. Shernyakov, N.V. Kryzhanovskaya, I. N. Kaiander, D. Ouyang, R. Sellin, N. D. Zakharov, P. Werner, V. A. Shchukin, A. R. Kovsh, and D. Bimberg, Phys. Scr. **T114**, 37 (2004).

[9] R. L Sellin, Ch. Ribbat, M. Grundmann, N. N. Ledentsov, and D. Bimberg, Appl. Phys. Lett. **78**, 1207 (2001).

[10] R. L Sellin, Ch. Ribbat, D. Bimberg, F. Rinnev, H. Konstanzer, M. T. Kelemen, and M. Mikulla, Elect. Lett. **38**, 883 (2002).

[11] V. Cesari, W. Langbein, P. Borri, M. Rossetti, A. Fiore, S. Mikhrin, I. Krestnikov, and A. Kovsh, Optoelectronics **1**, 298 (2008).

[12] L. Jiang, S. S. Li, N. –T. Yeh, J. –I. Chyi, C. E. Ross, and K. S. Jones, Appl. Phys. Lett. **82**, 1986 (2003).

[13] S. Chakrabarti, A. D. Stiff-Roberts, X. H. Su, P. Bhattacharya, G. Ariyawansa, and A. G. U. Perera, J. Phys. D: Appl. Phys. **38**, 2135 (2005).

[14] P. Bhattacharya, S. Ghosh, and A. D. Stiff-Roberts, Annu. Rev. Mater. Res. **34**, 1 (2004).

[15] M. Henini and M. Bugajski, Microelect. J. **36**, 950 (2005).

[16] D. Bimberg, J. Phys. D: Appl. Phys. **38**, 2055 (2005).

[17] D. J. Mowbray and M. S. Skolnick, J. Phys. D: Appl. Phys. **38**, 2059 (2005).

[18] A. Rogalski, J. Antoszewski, and L. Faraone, J. Appl. Phys. **105**, 091101 (2009).

[19] A. Krier, Ed., *Mid-infrared Semiconductor Optoelectronics*, (London: Springer-Verlag, 2006).

[20] N. Bertru, O. Brandt, M. Wassermeier, and K. Ploog, Appl. Phys. Lett. **68**, 31 (1996).

[21] A. F. Tsarsul'nikov, N. N. Ledentsov, M. V. Maksimov, B. Ya. Mel'tser, P. V. Neklyudov, S. V. Shaposhnikov, B. V. Volovik, I. L. Krestnikov, A. V. Sakharov, N. A. Bert, P. S. Kop'ev, Zh. I. Alferov, and D. Bimberg, Semiconductors **31**, 55 (1997).

[22] A. F. Tsarsul'nikov, S. V. Ivanov, P. S. Kop'ev, A. K. Kryganovskii, N. N. Ledentsov, M. V. Maksimov, B. Ya. Mel'tser, P. V. Nekludov, A. A. Suvorova, A. N. Titkov, B. V. Volovik, M. Grundmann, D. Bimberg, and Zh. I. Alferov, J. Elect. Materials **27**, 414 (1998).

[23] E. Alphandéry, R. J. Nicholas, N. J. Mason, and B. Zhang, P. Möck, and G. R. Booker, Appl. Phys. Lett. 74, 2041 (1999).

[24] P. Möck, G.R. Booker, N.J. Mason, R.J. Nicholas, E. Alphandéry, T. Topuria, N.D. Browning, Mat. Sci. Eng. B **80**, 112 (2001).

[25] E. Alphandéry, R. J. Nicholas, N. J. Mason, S. G. Lyapin, and P. C. Klipstein, Phys. Rev. B **65**, 115322 (2002).

[26] R.A. Child, R.J. Nicholas, N.J. Mason, E. Alphandéry, Physica E **13**, 241 (2002).

[27] R. A. Child, R. J. Nicholas, N. J. Mason, P. A. Shields, J. –P. R. Wells, I. V. Bradley, J. Phillips, and B. N. Murdin, Phys. Rev. B **68**, 165307 (2003)

[28] N. Curtis, K. Kupczik, P. O'Higgins, M. Moazen, and M. Fagan, Anatomical Record **291**, 491 (2008).

[29] M. Moazen, N. Curtis, P. O'Higgins, M. E. H. Jones, S. E. Evans, M. J. Fagan, Proc. R. Soc. B **276**, 39 (2008).

[30] T. Hantschel, A. I. Kauerauf, and B. Wygrala, Marine and Petroleum Geology **17**, 815 (2000).

[31] B. Jogai, J. Appl. Phys. **88**, 5050 (2000).

[32] S. Rahman, J. Gorman, C. H. W. Barnes, D. A. Williams, and H. P. Langtangen, Phys. Rev. B **73**, 233307 (2006).

CHAPTER 2

BACKGROUND THEORY

2.0 INTRODUCTION

The background study will involve a few areas of study due to the project require essential background in physics of semiconductors. Therefore, the background study includes the subjects of quantum mechanics, general solid state physics and physics of semiconductor.

2.1 QUANTUM MECHANICS

Quantum mechanics is a fundamental physical theory that deals with the motion of bodies and associated physical quantities such as energy and momentum. It arose from an accumulation of evidence that many physical phenomena occurring at the atomic scale could not be explained within the framework of classical physics, in the sense that it provides descriptions and explainations for many phenomena those classical theories simply cannot explain. The details about the evolution of the quantum theories can be found in the introductory text books to the topic [1,2].

In quantum mechanics, the state of a system is described by a wave function. This is the most basic term in quantum mechanics that is being used most of the time, describing the state of a physical system. Without knowledge of wave function, it will not be easy to learn or understand about quantum mechanics. For all independent and identical systems of which consisting a particle moving under some influence of external force, the properties of these systems can be described by a single wave function $\Psi(x, y, z, t)$ which contains all the information that can be known about them.

Generally, quantum mechanics does not assign definite values to observables. Instead, it makes predictions about probability distributions, which are the probability of obtaining each of the possible outcomes from measuring an observable. These measurements are limited in accuracy by the uncertainty principle, $\Delta x \Delta p_x \geq \hbar/2$. The expected value of some observation is calculated by operating on the wavefunction with

the operator, A, corresponding to the observable, a. The operation to obtain the expected value is analogous to a standard weighted average,

$$\langle a \rangle = \int \Psi^* A \Psi \, dV, \tag{2.1}$$

where a is a possible observation of the operator A. Also, the probabilities will depend on the quantum state at the instant of the measurement. There are, however, certain states that are associated with a definite value of a particular observable. These are known as "eigenstates" of the observable. For example, the solutions of the Time-Independent Schrödinger Equation are definite values.

Before outlining the development of the Time-Independent Schrödinger Equation, it is very useful to know that there is a differential operator associated with every physical observable in quantum mechanics. For example, associated with the linear momentum, p, is simply $-i\hbar\nabla$. The same relationship holds between the quantum mechanical operators as that between the corresponding classical physical quantities, which known as Corresponding Principle. A list of physical observables and their corresponding quantum mechanical operator expressions is presented in Table 2.1.

Physical Quantity	***Operator***
Momemtum, p	$-i\hbar\nabla$
Position, r	R
Kinetic energy, T	$-\hbar^2/2m\nabla^2$
Potential energy, V	$V(r)$
Total energy, H	$-\hbar^2/2m\nabla^2 + V(r)$

Table 2.1 : Classical Physical Observables and Their Associated Quantum Mechanical Operators.

The Time-Independent Schrödinger Equation is shown below:

$$\left[-\frac{\hbar^2}{2m}\nabla^2 + V(r)\right]\psi(r) = E\psi(r) \tag{2.2}$$

$$H = -\frac{\hbar^2}{2m}\nabla^2 + V(r) \tag{2.3}$$

The term in the bracket is called the Hamiltonian operator of the particle and is denoted by H, $\psi(r)$ is the wavefunction and E is the eigenenergy of a particle in an eigenstate.

The wave function is linear and homogeneous so that the superposition principle holds. This means that for a given system with solutions of wave equation Ψ_1 and Ψ_2, then $(c_1\Psi_1 + c_2\Psi_2)$, where c_1 and c_2 are constants, must also be a solution. Also, the wave function and its space derivative ($\partial\Psi/\partial x + \partial\Psi/\partial y + \partial\Psi/\partial z$) are continuous, finite and single valued. Otherwise, the second derivative of wave function will be infinite at the point where $\nabla\Psi$ changes discontinuously and there will be no solution for the Schrödinger Equation.

2.2 GENERAL SOLID STATE PHYSICS

The underlying elements of solid state physics that are required to understand the the electronic states in semiconductors are summarized here. A more thorough and first principle description of the following summary may be found in such excellent introductory texts like *C. Kittel*, 2005 [3]; *H. T. Grahn*, 1996 [4], *K. F. Brennan*, 1999 [5] and *P. Y. Yu and M. Cardona*, 2001 [6].

2.2.1 BRAVAIS LATTICE and ZINC-BLENDE STRUCTURE

Lattice constant of a compound semiconductor is one of the most important parameters to be considered in designing semiconductor based optoelectronic devices. The lattice constant is the constant distance between unit cells in a crystal lattice. A lattice is the term given to a spatially periodic array of points. If a group of atoms that have consistent composition, arrangement and orientation (a basis) is attached to all of the points in the lattice, the latter which is a purely mathematical construct, will allow a crystal to be described. The lattice is therefore an infinitive array of discrete points with an arrangement and orientation that appears equivalent regardless of the point from which it is viewed. The set of lattice geometries that can provide a description of any perfect crystal, provided the correct basis is attached at each site, are commonly referred to as Bravais lattices.

The points in the Bravais lattice written in terms of primitive translation vectors, a_i are:

$$r' = r + n_1a_1 + n_2a_2 + n_3a_3$$
$$= r + R \qquad (2.4)$$

Here, the n_i represent arbitrary integers and the a_i do not all lie on the same plane. The equivalence of points r and r' in an infinite lattice make it clear that a single grouping of atoms, repeated throughout that entire crystal, will fill the lattice. This group is called a unit cell.

An example of a Bravais lattice is the face centered cubic (fcc) lattice as shown in Figure 2.1.

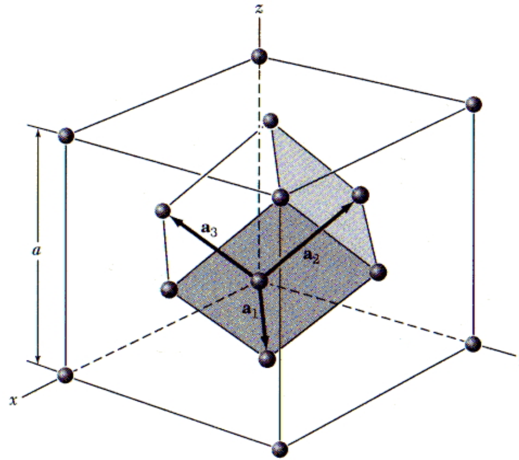

Figure 2.1 : The Unit Cell of a fcc Bravais Lattice. Reproduced from Ref. [3].

The primitive translation vectors of the fcc Bravais lattice are:

$$a_1 = \tfrac{1}{2}a(j+k) \qquad (2.5a)$$

$$a_2 = \tfrac{1}{2}a(k+i) \qquad (2.5b)$$

$$a_3 = \tfrac{1}{2}a(i+j) \qquad (2.5c)$$

where i, j and k represent orthonormal vectors along the Cartesian axes x, y and z respectively and a is defined as the lattice constant. The crystal lattice translation vectors R of Equation 2.4 define the Bravais lattice if the primitive vectors are defined correctly.

The zinc-blende structure is named after the cubic phase of ZnS, in German Zinkblende (in English spalerite). It corresponds to the diamond structure with two different atoms forming the basis, e.g., zinc and sulphur. Zinc-blende structure has eight atoms of two different species in a unit cell. The structure consists of two fcc lattices separated from each other along the [111] axis by a quarter of the diagonal

length. Zn atoms are placed on one fcc lattice and S atoms on the other fcc lattice as shown in Figure 2.2.

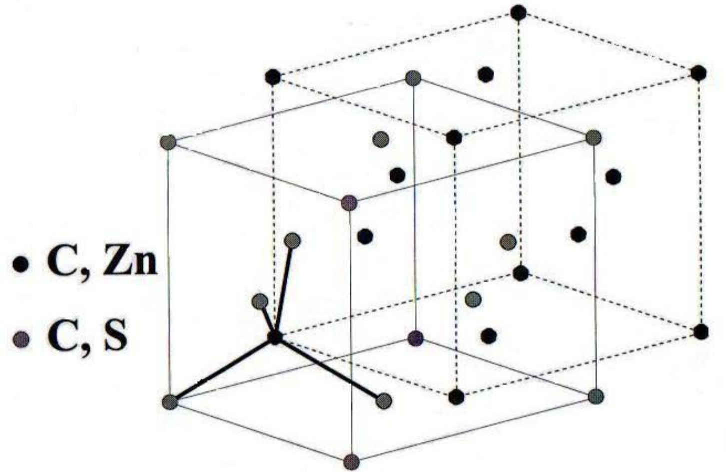

Figure 2.2 : The Zinc-Blende Crystal Structure. Reproduced from Ref. [4].

Each atom of one kind has four nearest neighbours of the opposite kind. The Zn atoms are at the positions (0,0,0), (0,½,½), (½,0,½), and (½,½,0), and the S atoms at (¼,¼,¼), (¼,¾,¾), (¾,¼,¾), and (¾,¾,¼). This structure is the most common lattice for binary compounds with covalent bonding such III-V and some II-VI compound semiconductors.

2.2.2 The RECIPROCAL LATTICE and BRILLOUIN ZONE

The periodicity and symmetry of the lattice play a fundamental role in introducing the concepts of the reciprocal lattice and the Brillouin zone, and allows one to specify the energy levels in a semiconductor in terms of the energy versus momentum picture. In general, the plane wave will not have the periodicity of the lattice. That is the Equation 2.6 is not generally true.

$$e^{ik.r} = e^{ik.(r+R)} \tag{2.6}$$

However, there exist a set of wavevectors for which Equation (2.6) holds true and consequently exhibit the periodicity of the lattice. These wavevectors are known as reciprocal lattice vectors (RLV) and by Equation 2.6:

$$G.R = 2\pi n \tag{2.7}$$

where n is an integer and G is an RLV. The entire set of G can be constructed in terms of primitive vectors, b_i in reciprocal space:

$$G = \sum_{i=1}^{3} M_i b_i \qquad (2.8)$$

where M_i denote integers. Whereas the primitive vectors, b_i of the reciprocal lattice are constructed from the primitive translation vectors, a_i using the transformation:

$$b_i = 2\pi \frac{a_j \times a_k}{a_i \cdot (a_j \times a_k)} \qquad (2.9)$$

where *i, j* and *k* are cyclically interchanged and Equality 2.9 must satisfy the condition:

$$b_i . a_j = 2\pi\delta_{ij} \qquad (2.10)$$

and this implies for every lattice point G that

$$exp(iG.R) = 1 \qquad (2.11)$$

for all vectors G of the reciprocal lattice. The reciprocal lattice of a Bravais lattice is again a Bravais lattice.

In general, the first Brillouin zone can be defined as the Weiner-Seitz cell for the reciprocal lattice. The Weiner-Seitz cell can be constructed by bisecting the nearest RLVs with perpendicular planes and taking the smallest polyhedron bounded by these planes. The further Brillioun zones can be constructed in a similar fashion by bisecting the next nearest RLVs. The first Brillioun zone for an fcc crystal is an truncated octahedron as shown in Figure 2.3.

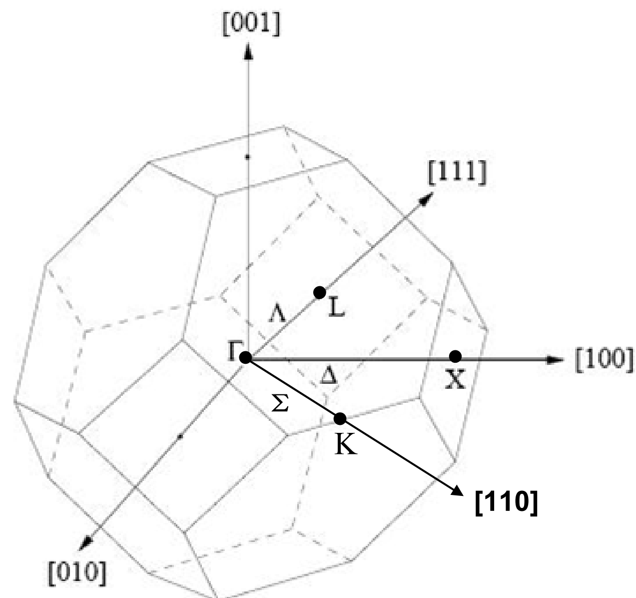

Figure 2.3 : The First Brillioun Zone of Face Centered Cubic Crystal. After Ref. [4].

The first Brilloun zone contains a number of points of higher symmetry, which are particularly useful in describing the band structure. The *Γ*-point denotes the centre of the Brillioun zone and it is the highest symmetry point. The other three high symmetry points in the first Brillouin zone of the fcc lattice are *X*-, *L*- and *K*-point, which connected to the *Γ*-point at [100], [111] and [110] direction, respectively. The connecting lines between these high symmetry points to the *Γ*-point are denoted as *Λ*, *Δ* and *Σ*, respectively.

The Brillioun zone plays an important role in solid-state physics since it defines the set of all *k* vectors for the energy gap in the *E*(*k*) spectrum. The detail about the energy band structure is presented next.

2.2.3 ENERGY BAND STRUCTURE

As a result of the laws of quantum mechanics, electrons in isolated atoms can have only certain discrete energy values. As these isolated atoms are brought together to form a crystal, the electrons become restricted not to a single energy level, but rather to ranges of allowed energies, or bands called the valence band and the conduction band. These two bands are separated by an energy band gap, which is a very important characteristic of a semiconductor material.

Within these energy gaps no allowed energy states are available; so called forbidden bands. This energy band structure of the semiconductor is determined by its periodic potential and symmetry. The valence band is the highest occupied band just below the fundamental bandgap, while the conduction band is the lowest unoccupied band just above the fundamental bandgap. These are the most important bands to consider for semiconductors because many electrical and optical properties of semiconductors are determined by the band structure in the vicinity of the bandgap.

Figure 2.4 shows the typical band structure of semiconductors. Semiconductors can be divided into direct band gap and indirect band gap semiconductors. The direct band gap semiconductors are semiconductors with both the valence band maxima and conduction band minima occur at the same wavevectors; which is the centre of the Brillouin zone. The valence band maxima and conduction band minima of an indirect band gap semiconductors occur at different locations of the Brillouin zone. The

conduction band of the direct gap semiconductor is shown in the solid line, while the conduction band of the indirect semiconductor is shown in the dashed line.

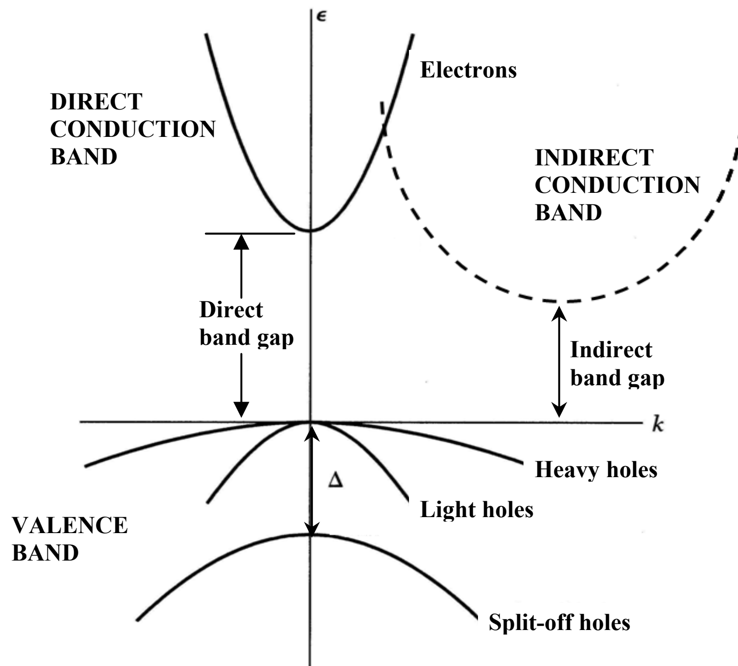

Figure 2.4 : Typical band structure of semiconductors.

The valence band has a more complicated structure due to the degeneracy of the top of valence band states. The coupling between the orbital angular momentum of valence band states and electronic spin resulting in a splitting of the top of valence band into heavy hole, light hole and split off bands while the bottom of the conduction band has no degeneracy.

2.2.4 BLOCH THEOREM

The Bloch theorem states that the eigenfuctions of a Hamiltonian H(r) with V(r+R) = V(r) can be chosen as:

$$\Psi_k(\mathrm{r}) = u_k(\mathrm{r})e^{ik.r}, \quad (2.12)$$

where $u_k(\mathrm{r+R}) = u_k(\mathrm{r})$ (2.13)

are the Bloch functions, which exhibit the same translational symmetry as the crystal structure. k denotes the crystal wavevector of the electron moving in the crystal potential.

A Bloch function can always be decomposed into a sum of travelling waves and cell periodic part, which can be readily assembled into localized wave packets to represent electrons and holes that propagate through the potential field of the ion cores. Therefore, it is the ideal basis set for models such as the ***k.p*** model.

2.2.5 The k·p MODEL

The ***k·p*** model is a semiemperical method to calculate the band structure and wave functions in the vicinity of a given point, k_0, in great detail with the aid of perturbation theory. It is a semiemperical extension of the effective mass approximation. Hence it maintains the ideas of simplicity, good agreement with the true band structure, and the smallest possible set of parameters that need to be determined by experiment (or by comparison with the first principles calculations). The method works well near band extrema, the point of interest when discussing optoelectronic properties. The one electron Schrödinger equation in a periodic potential $V(r)$ is given by

$$H\psi = \left[\frac{p^2}{2m} + V(r)\right]\psi = E\psi \;. \tag{2.14}$$

The electronic wavefunctions in a periodic potential satisfy Bloch's theorem:

$$\psi_{n,k}(r) = e^{ik\bullet r}u_{nk}(r) \tag{2.15}$$

i.e. that they may be separated into a slowly varying envelop function, with wavevector k, and a cell-periodic Bloch function u_{nk} (r). The band index n runs over a complete set of bands. Substituting Eq. (2.15) into Eq. (2.14) gives [6,9,10]:

$$\left\{\frac{p^2}{2m} + \frac{\hbar}{m}k \bullet p + \frac{\hbar^2 k^2}{2m} + V(r)\right\}u_{nk}(r) = E_n(k)u_{nk}(r). \tag{2.16}$$

For any given k, the set of all u_{nk} (r) is complete for functions having the periodicity of $V(r)$. At $k = k_0$, Eq. (2.16) reduces to [6]:

$$\left(\frac{p^2}{2m} + V(r)\right) u_{n0} = E_{n0}u_{n0} \qquad (n = 1,2,3,.....). \tag{2.17}$$

The solution of Eq. (2.17) form a complete and orthonormal set of basis functions. The band index n runs over a complete set of bands. Once E_{n0} and u_{n0} are known, the terms $\hbar \boldsymbol{k}\cdot\boldsymbol{p}/m$ and $\hbar^2k^2/(2m)$ can be treated as perturbation in Eq. (2.16). Since the perturbation terms are proportional to k, ***k·p*** method works best for small values of k [6,9,10].

The usual practice in calculating the electronic structure using ***k·p*** method

involves approximation in limiting the band index n to certain number of bands of interest. For example, the 8-band model, which explicitly includes eight bands around the Γ-point of the Brillouin zone, namely, electron, heavy-, light-, and spin orbit split-off hole bands (each of them is double degenerate due to the spin, and treats all other bands as remote). This approach is called Kane's [9,10] model and it has shown to be very predictive for the III-V compound semiconductors.

Suppose one is mainly interested in the six valence bands and ignores the coupling to the two degenerate conduction bands with both spins, one arrives at the 6-band Luttinger-Kohn's model [11,12]. For most III-V semiconductors, the split-off bands are several hundred milielectron volts (meV) below the heavy-hole and light-hole bands. Since the energy range of interest is only several tens of meV, it is usual to assume that the split-off bands can be ignored. Then the ***k·p*** method reduces to 4-band Luttinger-Kohn's model [11]. Due to the decoupling of the conduction band and valence bands, the electron level has to be calculated by using the single band effective mass approximation when determining the transition energy. The effective mass approximation also can be used to determine the energy levels for the degenerate valence bands for simplicity.

In the Luttinger-Kohn model (4-band and 6-band), only interactions within the valence bands are treated exactly, while Kane (8-band) treats the ***k·p*** interactions within the valence and conduction bands together.

2.2.6 EFFECTIVE MASS

The energy of a free electron is given by

$$E_n(k) = \frac{\hbar^2 k^2}{2m} \tag{2.18}$$

The energy of an electron in a solid near a maximum and minimum of the band structure can be expanded in a power series of k. Since the first derivative vanishes near a maximum or minimum of the band structure, the leading term will be of order k^2. In this sense, charge carriers in a solid can be described as free electrons with an effective mass, which is determined by the curvature of the band structure in the vicinity of the energy gap. Then Equation 2.18 becomes:

$$E_n(k) = \frac{\hbar^2 k^2}{2m^*} \tag{2.19}$$

where m^* is the effective mass of the electron in the crystal.

The use of an effective mass is an especially useful technique for describing the motion of an electron in a crystal. Effective mass model enables us to account for the effect of the ionic potential on the electron dynamics by simply changing the mass of the electron in all the equations describing its behaviour and subsequently reduce the complicated electron moving problem to a simple free particle problem with a modified mass.

2.3 GENERAL THEORY of SEMICONDUCTORS

Generally, semiconductors are solids with a finite energy gap between 0-4 eV, which results in a moderate conductivity (10^{-9}-10^{2} (Ωcm^{-1})) and moderate carrier density ($<10^{17}$ cm^{-3}) at room temperature [4]. Germanium (Ge) and silicon (Si) are typical elementary semiconductors, while III-V and II-VI compounds, such as gallium arsenide (GaAs) and zinc oxide (ZnO), are typical compounds semiconductors.

As mentioned before, all semiconductors can be classified either as direct gap or indirect gap semiconductors. The optical properties of direct gap semiconductors differ considerably from those of indirect gap semiconductors. In direct band gap semiconductors, the momentum of both the electrons and holes are equal or zero. Hence, the radiative recombination due to the interband transitions is highly probable. This makes the direct band gap semiconductors superior for light emitting applications.

2.3.1 III-V COMPOUND SEMICONDUCTORS

Most of the III-V semiconductors such as GaAs, GaSb, InAs and InSb exist in zinc-blende structure. Ga and In belong to the third column while As and Sb belong to the fifth column of the periodic table. Similar to ZnS, zinc-blende III-V compound semiconductors have eight atoms of two different species in a unit cell. The group III atoms are at the positions (0,0,0), (0,½,½), (½,0,½), and (½,½,0), and the group V atoms at (¼,¼,¼), (¼,¾,¾), (¾,¼,¾), and (¾,¾,¼). Unlike the diamond structure, the zinc-blende structure does not have inversion symmetry. As the zinc-blende III-V compound

semiconductors lack inversion symmetry, the dielectric polarisation under an externally applied stress or electric field can develop. This is known as the piezoelectric effect.

Experimental and theoretical investigations into zinc-blende III-V compound semiconductors have continued to increase over the past few decades since 1950s. This is because these substances possess electronic and optoelectronic properties which can be exploited in a range of different devices. One of the advantages is that they have a range of electric properties (e.g. band gap values) as well as a range of lattice parameters, so that there is flexibility in influencing both properties and growth characteristics by choice of substrate and overgrowth.

This flexibility is accelerated by the use of ternary or quaternary alloys, which provides further band structure modifications and varies the energy band edge between the two or more binary III-V constituents. The wealth of work, particularly on the electronic band structure of such materials through the so called 'band gap engineering', provides an excellent starting point to develop artificial materials through heterostructures design (Chapter 3). Through this band gap engineering and the use of heterostructures, the electronic and optical properties of the semiconductor devices can be tailored for specific applications.

2.3.2 ENERGY BAND STRUCTURE of GaAs, GaSb, InAs and InSb

The zinc blende III-V compound semiconductors that will be focused on in this thesis are GaAs, GaSb, InAs and InSb. The electronic band structures of these compound semiconductors are shown in Figure 2.5.

As shown in the figure, the overall band structures are very similar, except for the different energy scales. All these semiconductors are direct gap where both the conduction band minima and valence band maxima are at the Γ-point. Besides the lowest conduction band minima at Γ-point, there are also two higher sets of minima at L- and X- point. The valence band has common structure characteristics for all zinc blende III-V compound semiconductors.

The band gap data for GaAs, GaSb, InAs and InSb at the three symmetry points is listed in Table 2.2. As can be seen from Table 2.2, the L- and X-band energy gap are

much higher than the Γ-band energy gap except the L-band energy gap for GaSb, where the difference is only ~85 meV. This may lead to the Γ-L crossover due to the strain effect (detail in Chapter 6).

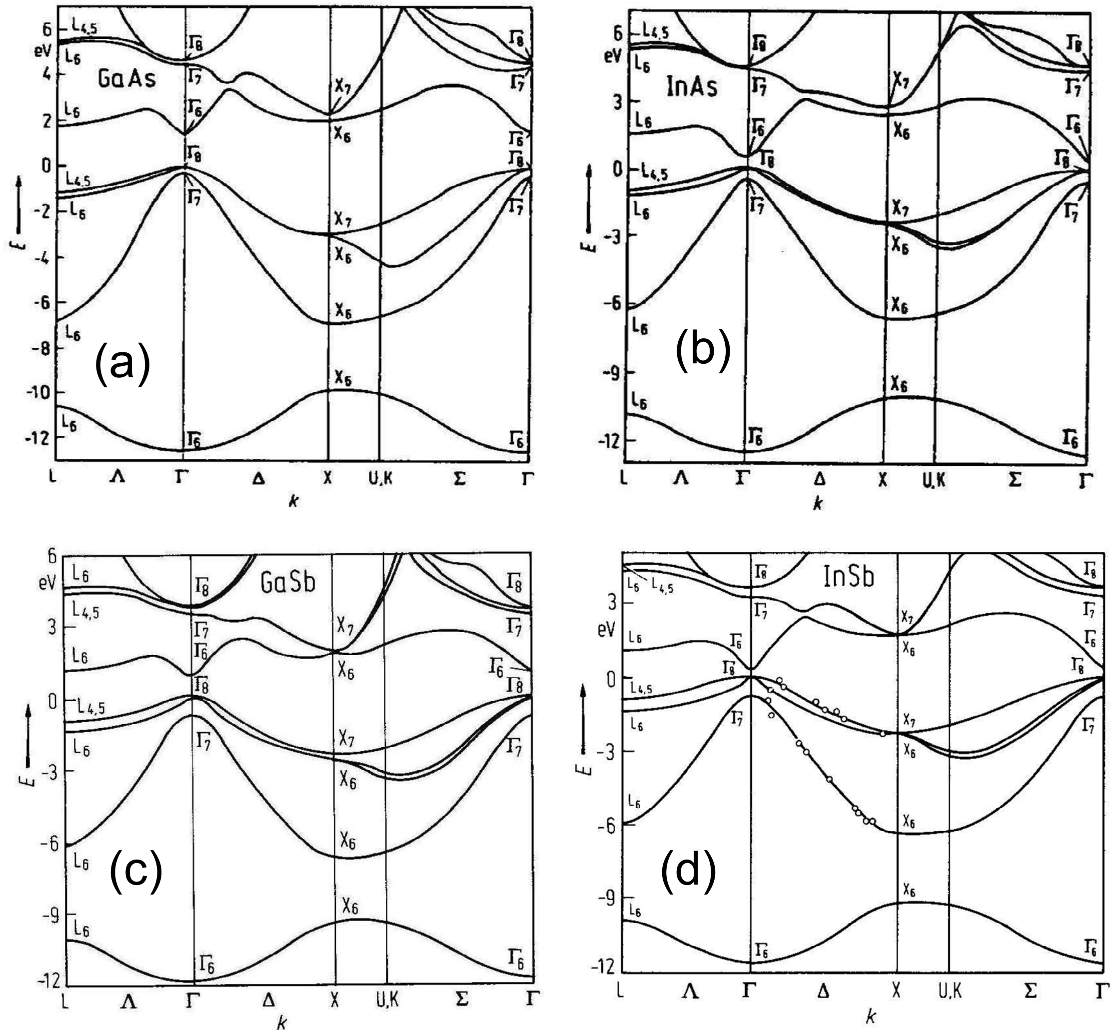

Figure 2.5 : Energy band structure for (a) GaAs, (b) InAs, (c) GaSb, and (d) InSb. Reproduced from Ref. [7].

Material	E_g (Γ)	E_g (L)	E_g (X)
GaAs	1.424	1.708	1.9
GaSb	0.725	0.81	1.032
InAs	0.355	1.43	2.0
InSb	0.17	1.0	1.7

Table 2.2 : Band gap data for GaAs, GaSb, InAs and InSb at 300K [8].

References:

[1] R. L. Liboff, *Introductory Quantum Mechanics*, (San Francisco: Holden-Day, Inc., 1980).

[2] B. H. Bransden, and C. J. Joachain, *Introduction to Quantum Mechanics*, (Essex: Longman Scientific and Technical, 1992).

[3] C. Kittel, *Introduction to Solid State Physics*, 8th edition, (USA: John Wiley and Sons Inc., 2005)

[4] H. T. Grahn, *Introduction to Semiconductor Physics*, (Singapore: World Scientific Publishing Co. Pte Ltd., 1999)

[5] K. F. Brennan, *Physics of Semiconductor With Applications To Optoelectronic Devices*, (Cambridge, UK: Cambridge University Press, 1999).

[6] P. Y. Yu and M. Cardona, *Fundamental of Semiconductors: Physics and Materials Properties*, 3rd edition, (Berlin: Springer-Verlag, 2001).

[7] O. Madelung and M. Schulz, Ed., *Semiconductor: Intrinsic Properties of Group IV Elements and III-V, II-Vi and I-VII Compounds*, Landolt-Börnstein Series Vol. 22 (Springer-Verlag, Berlin, 1987).

[8] S. Tiwari and D. J. Frank, Appl. Phys. Lett. **60**, 630 (1992).

[9] E. O. Kane, *The k·p method*, Chapter 3, in R. K. Willardson and A. C. Beer, Eds., *Semiconductors and semimetals*, Vol. 1, (New York: Academic, 1966).

[10] E. O. Kane, *Energy Band Theory*, Chapter 4A, in W. Paul, Ed., *Handbook on Semiconductors*, Vol. 1, (Amsterdam: North-Holland Publishing Company, 1982).

[11] J. M. Luttinger and W. Kohn, Phys. Rev. **97**, 869 (1955).

[12] S. L. Chuang, *Physics of Optoelectronic Devices*, (New York: Wiley, 1995).

CHAPTER 3

LITERATURE REVIEW

3.0 INTRODUCTION

This chapter has two main objectives: first, it aims to review the developments leading to the use of SAQDs in otptoelectronic devices. Second, it surveys the established methods used in studies of the electronic structure of SAQDs and other low dimensional structures. The chapter begins with a discussion about the development of low dimensional structures and of the use of heterostructures to cause quantum confinement of the charge carriers. Next, fabrication techniques for QDs are outlined along with previous work on Sb-based SAQDs. Finally, a survey of theoretical work on QD electronic properties is given.

3.1 SEMICONDUCTOR HETEROSTRUCTURES

When two different semiconductor materials with different electronic properties are grown on top of each other, a semiconductor heterostructure is formed. The interface between these two materials is then known as a heterojunction and the electronic properties of the heterostructure are determined by this heterojunction.

Heterostructures can be realised from various combination of semiconductors and their alloys [1]. Figure 3.1 shows the band gap as a function of the lattice constant for the III-V semiconductors at 0K. The connecting curves represent band gaps for the ternary alloys. Solid lines denote the Γ-valley direct gap semiconductors while X-valley and L-valley indirect gaps are indicated by the dashed and dotted lines, respectively. The III-V compound semiconductors and their alloys offer a wide range of material combinations in heterostructures and hence the possibility of 'band structure engineering'.

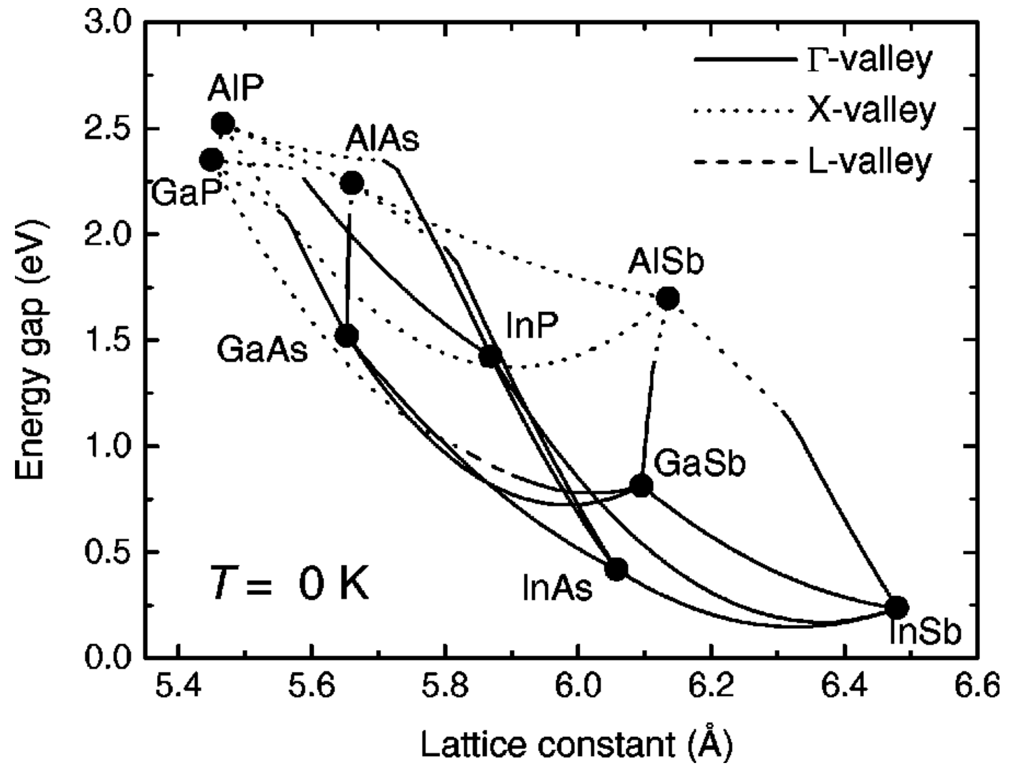

Figure 3.1 : Lowest band gap as a function of lattice constant for III-V compound semiconductors (Filled circle) and their ternary alloys (lines) at 0K. The solid, dotted and dashed lines represent the Γ-, X-, and L-valley gaps, respectively. Reproduced from Ref. [1].

As a result of the different in energy gap, semiconductor heterostructures exhibit an abrupt discontinuity in both conduction band and valence bands at the heterojunction. Figure 3.2 shows the various types of band alignment that can be formed in semiconductor heterostructures consisting of two semiconductors of different band gap E_g^1 and E_g^2. E_c, E_v, ΔE_c, and ΔE_v are the conduction band, valence band, conduction band offset and valence band offset energies, respectively.

The different band alignments arising from the relative energy position of the valence and conduction bands at the interface can result in a lower potential for both electrons and holes in one material (i.e., type-I lineup in Figure 3.2(a)) or a lower potential for electrons in one material and for holes in the other material (i.e., type-II lineup in Figure 3.2 (b) and (c)). In band structure terminology, the type-I systems can be considered as direct in the real space whereas the type-II systems are indirect in real space.

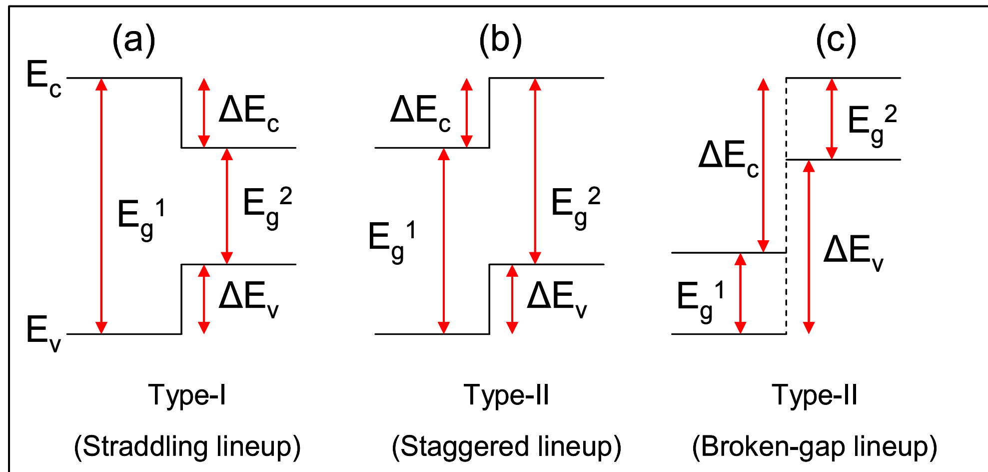

Figure 3.2 : Schematic diagrams of the types of band alignment at a heterojunction.

Figure 3.3 below summarises the unstrained band alignments as a function of the lattice constant for III-V compound semiconductors as well as elementary Si and Ge semiconductors [2]. The figure consolidates data involving discontinuities, barrier heights, and band gap under unstrained conditions. The circles indicate the band edges of the binary semiconductors and the lines shown the band edges of the ternary alloys. The two end points of each ternary line are the binary constituents of that ternary. The band-edge discontinuity between two semiconductor alloys may be found from the difference in energy between their band-edge energies.

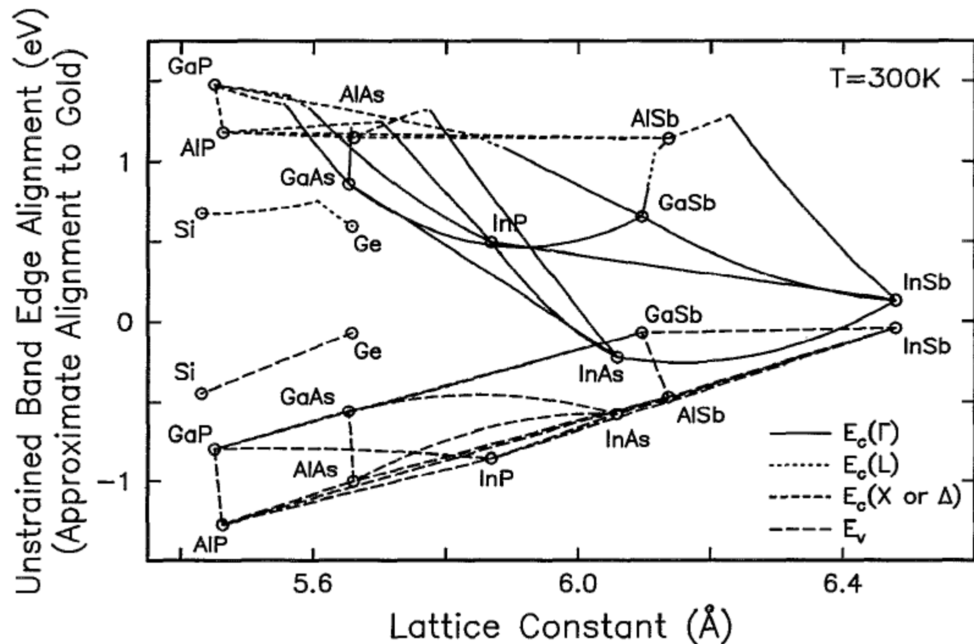

Figure 3.3 : The unstrained conduction band-edge and valence band-edge energies plotted as a function of the lattice constant of semiconductors, approximately aligned to gold. Reproduced from Ref. [2]

For alloyed QDs, the average valence band position for the $A_{(1-x)}B_x$ solid solution with lattice constants a_A and a_B is given by [3]:

$$E_{v,av}^{AB}(x) = xE_{v,av}^{B} + (1-x)E_{v,av}^{A} + 3x(1-x)\left(a_v^A - a_v^B\right)\frac{(a_B - a_A)}{a_{AB}}, \quad (3.1)$$

where the lattice constant for the alloy is $a_{AB} = a_A(1-x) + a_B x$. Here, $E_{v,av}^{A}$ and $E_{v,av}^{B}$ are average valence band positions in pure compounds, a_v^A and a_v^B are hydrostatic deformation potentials for the valence bands in A and B. The band gaps of the bulk unstrained alloy are approximated by a quadratic dependence with "bowing" parameter c_α:

$$E_{g,\alpha}^{AB}(x) = (1-x)E_{g,\alpha}^{A} + xE_{g,\alpha}^{B} - c_\alpha x(1-x). \quad (3.2)$$

The deformation potentials for the alloyed QDs were linearly interpolated.

3.2 QUANTUM CONFINEMENT IN SEMICONDUCTORS

The use of heterostructures has led to the realisation of quantum well (QW) structures. A QW is a quasi-two-dimensional system as the motion of carriers is effectively restricted to a plane. The confinement of carrier along the growth direction in a QW results in structural, electronic and optical properties that are unique and different from the macroscopic bulk materials. The density of states (DOS) in a QW also differs from those of bulk materials. Figure 3.4 shows the evolution of the density of states as the effective dimensionality of the system reduces. As more dimensions are confined, the DOS becomes less continuous, and eventually becomes a delta-function in the zero-dimensional QD. QDs are often referred to as artificial atoms due to the discrete energy level structure.

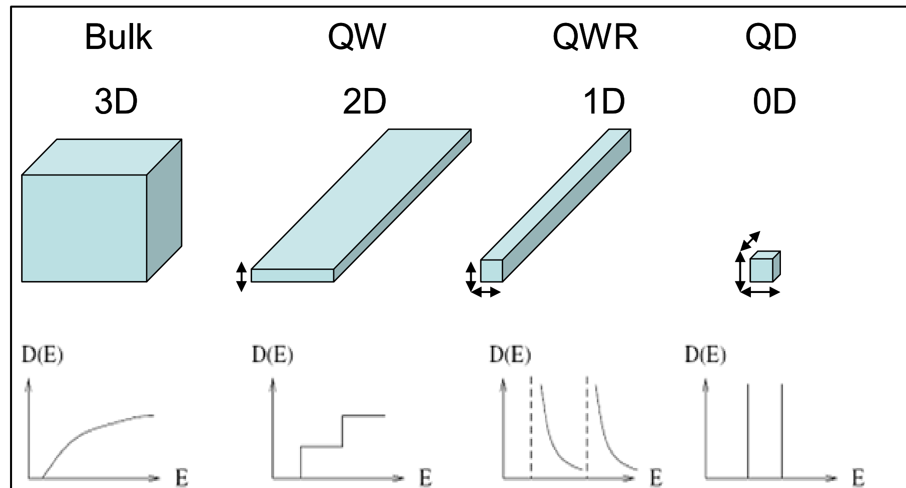

Figure 3.4: Density of states for various dimensional systems. After Ref. [4].

3.3 QUANTUM DOTS

QDs are zero-dimensional nanostructures that confine carriers in all three spatial dimensions. They possess strong application potential for electronic and optoelectronic devices due to their unique atomic-like electronic characteristics from the 3-D quantum confinement resulting in a δ-shaped DOS and atomic-like energy levels with spacings typically exceeding k_BT at room temperature. These unique behaviours of the QDs were predicted theoretically by *Arakawa and Sakaki* in 1982 [4]. It is believed that the δ-function like DOS and the enhanced electron and hole wavefunctions overlap in a QD may result in decreased threshold current densities, higher temperature stability of the threshold current, as well as higher differential gain for a QD laser. The first such QD lasers were created in 1994, with threshold current of 120 A/cm^2 at 77K [5].

Since the first demonstration of the QD lasers, further improvements have been achieved and other QD devices have been realised. The strong interest in semiconductor QDs is motivated by the feasibility of active media in future high speed electronic and photonic devices, both in term of lower threshold current densities, better thermal behaviour, high differential gain and longer device lifetime with important societal impact such as photonic sensors for environment monitoring [5,6], lasers [7-10], optical amplifier [11], photodetectors [12], and light emitting diodes (LEDs) [13]. Semiconductor QDs have also found application in quantum computing, quantum information processing and quantum cryptography [14-17].

3.3.1 THE FABRICATION of QDs

Conventionally, the fabrication of the QDs involves patterning of QWs by using electron beam lithography combined with wet chemical etching [18], or selective growth on a patterned substrate [19]. All these techniques have inherent limitations on the dimensions of QDs that can be fabricated, as a result of the finite resolution of the patterning mechanism and instabilities of the selective growth process. Additionally, the patterning and etching procedures often produce contamination and poor interface quality. In order to obtain QD devices that perform as predicted, uniform QDs with good control of size and other parameters is essential.

An alternative approach to growth is by the self-assembly epitaxial growth technique of highly strained semiconductors. Self-assembly is a phenomenon by which

nanostructures spontaneously form on surfaces during epitaxial growth. In general, the epitaxy growth of nanostructures can be categorised into three growth modes as shown in Figure 3.5, named after their original investigators as follow:

(a) Frank-van de Merwe (FvDM) growth,
(b) Volmer-Weber (VW) growth is a growth, and
(c) Stranski-Krastanow (SK) growth.

Frank-van de Merwe (FvDM) growth is a layer by layer growth mode, in which deposition of a material on a substrate leads to formation of a 2D epilayer. Volmer-Weber (VW) growth is a growth mode in which 3D islands are grown directly onto the substrate. Stranski-Krastanow (SK) growth involves an initial layer by layer growth until a critical thickness after which island begins to form on the 'wetting layer'.

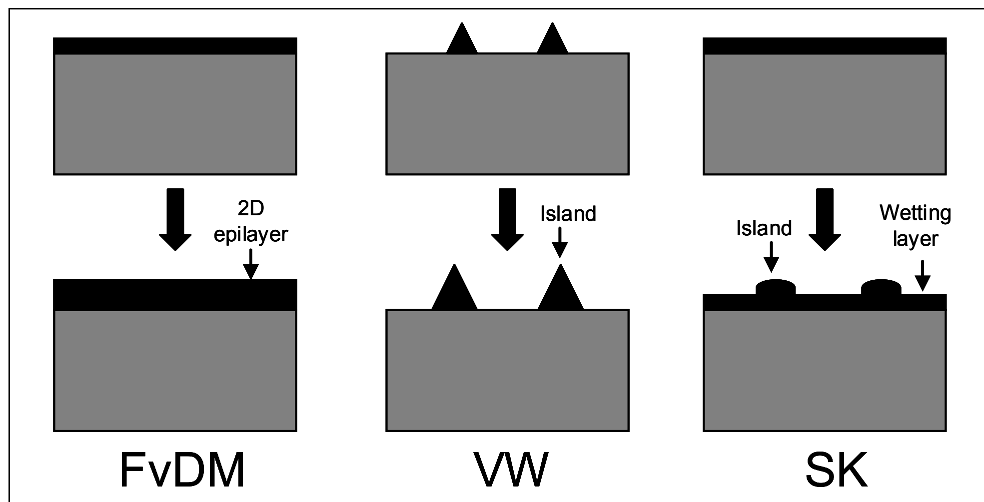

Figure 3.5 : Types of epitaxial growth mode.

The growth mode is determined by the strain (degree of lattice mismatch) and interface energies within the system. In lattice matched (hence minimal strain) systems, the sum of the surface and interface energies determines whether the deposited material wets the surface or forms islands. If the deposited material wets the surface, then the epitaxial growth is in FvDM growth mode. On the other hand, VW take place if the deposited material tends to form islands on the surface. In a lattice mismatched system, both FvDM and SK growth mode can occur. If the epilayer is thinner than a certain critical thickness, the growth mode is FvDM growth. If the growth continues, the strain builds up until a critical epilayer thickness at which formation of 3D islands becomes energetically more favourable, relaxation of the strain occurs and these small islands of nanometer range in size form, which can often be regular in size and shape. These

islands also can confine carriers in all three spatial dimensions. The formation of coherent and defect free QDs via SK growth is currently the most favourable fabrication technique. The QD structures grown via self-assembly in the SK mode are known as SAQDs.

3.4 Sb-BASED SAQDs for the MID-INFRARED

For novel optoelectronic devices such as long wavelength infrared lasers and detectors, the 3-5 μm (0.25-0.40 eV) window of the mid-infrared (MIR) wavelength range is the window of choice for device development due to the low CO_2 and H_2O absorption. Although experimental demonstration and theoretical modelling of a semiconductor laser based on QDs has recently been accomplished and many research papers have been published, there is lack of suitable laser diodes operating in the 3-5 μm (0.25-0.40 eV) domain. QW lasers reached mass production within a very few years of their introduction because of their low cost, high performance and high reliability. However there is no QW laser diode is able to operate continuous wave at room temperature at 3-5 μm wavelength range [10].

As mentioned earlier, a consortium of six multidisciplinary and complementary partners (including Hull) named DOMINO was established in order to investigate the feasibility of Sb-based SAQDs for MIR nanophotonic devices. The fundamental objective of the DOMINO project was to create a new class of nano-photonic devices, namely Sb-based quantum dot laser diodes, emitting continuous wave at room temperature in the MIR 3-5 μm wavelength range utilising type-I band alignment. The initial chosen SAQD system in this project was InSb/GaSb. Another goal of DOMINO project was to obtain a clear picture of the structural, electronic and optical properties of this SAQD. These properties are a prerequisite to obtaining reliable and high performance light emitting devices.

The Sb-based material system recieved much attention due to its potential for optical devices in the 3-5 μm (0.25-0.40 eV) spectral region and motivated by the feasibility of its use as the active medium in high speed electronic and long wavelength photonic devices. Sb-based III-V compounds have the smallest bandgaps, which means applications involving the longest wavelengths, of any of the III-V family of semiconductor compounds. The bandgaps of the Sb family extend from 1.6 eV for AlSb

to 0.14 eV for InSb at room temperature [20] and their ternary compounds such as indium thallium antimonide are able to extend the wavelength >11μm. The small bandgap materials are of interest for many devices, including tandem solar cells and thermo-photovoltaics. Their high electron mobilities, also a consequence of the small band gaps, make these materials potentially useful for cryogenic ultrahigh-speed electronic devices. Thus the Sb-containing semiconductor compounds are very promising for infrared detectors and emitters ranging from 1.3 to 1.55 μm range, which is of interest for fiber optic systems, through the 3-5 μm range (of interest for chemical sensor systems, infrared countermeasures, and future extremely long distance communication systems using non-SiO_2 fibers) and even into the 8-12 μm regime of interest for night vision and infrared imaging applications [21].

In spite of this promise, Sb-related devices and particularly QD devices remain relatively unexplored in comparison with those based on other III-V compounds. The earliest literature on Sb-based SAQDs dates from around the end of 1995. By analogy with the InAs/GaAs system, most work has been carried out on the InSb/GaSb system [22-29]. These nanostructures are grown via the SK growth mode. Their morphological and optical properties were not suitable for device applications as the QDs densities are as low as 10^9dot/cm^2, with typically large dot lateral size (50-100 nm). These nanostructures exhibit PL emission only at low temperature and between 0.68-0.75 eV depending on the growth conditions. However, room temperature electroluminescence between 0.48-0.73 eV has been observed from coupled QDs and QWs in the InAs/InSb/GaSb material system [30,31].

Other Sb-based SAQD systems that are being studied include InSb/GaAs [32-35], for which PL had been observed in the range 1.1-1.5 eV, GaSb/GaAs [32,33,36] and AlSb/GaAs [32,33], where emission has been observed around 1.16 eV and 1.26 eV, respectively. InAsSb/InP systems have also been studied and PL was observed around 0.56-0.73 eV [37–43]. A type-II InAsSb/InAs system showed MIR emission at 0.286 eV and 0.316 eV, which was reported as from the ground and first excited state, respectively [40,41]. The same group has also studied a quaternary alloy system, InAsSbP/GaAs but only low temperature emission around 0.75 eV was observed.

An interesting result was published by *Ivanov et al.* [42-45] from the Ioffe Physico-Technical Institute. They reported the formation of QD-like InSb

submonolayers (SML) inserted within an InAs matrix by briefly exposing the InAs rich growth surface with a Sb flux, exploiting a very strong Sb-to-As exchange reaction [42,43]. Further deposition of 1–2 monolayer (ML) of InSb on such QD-like nanostructures leads to the formation of true QDs [44,45]. By using this technique, they report a density of ~10^{12} dot/cm^2 of extremely small QD–like structures (lateral size ~2.5 nm). These islands show PL between 3.9-4.3 μm, but if a thicker layer is deposited (even 1-2 MLs of InSb), growth of non-coherent islands is observed, with consequent dramatic change in optical properties.

Cornet et al. [46] have carried out theoretical study on the InAsSb/InP QD system and predicted an emission wavelength of about 5 μm at room temperature. However, *Pryor and Pistol* [47] have predicted a contrasting result in the same year, where the band gap of the InAsSb/InP QD system increased beyond this wavelength. *Shusterman et al.* [48] reported the formation of InSb quantum dots by droplet heteroepitaxy using an MOVPE system. They studied different surfaces (InAs, GaAs and GaSb) and found a PL emission around 4 μm at 10 K for InSb/GaAs QDs. From these studies, only As-terminated surfaces seem to be suitable to achieve high density and luminescence in the MIR region.

These latest results clearly show that not only is interest in the fabrication of Sb-based SAQDs for MIR applications growing, but also that unusual deposition techniques are required to obtain high performances suitable for device applications from such materials. In addition, investigations of QDs heterostructures have shown that, although some of the anticipated benefits of QDs have indeed been realised in particular in terms of device performance, the properties of the actual QD systems often differ notably from the theoretical model. Their properties can thus depart from the predictions and refinements of the theoretical models become necessary.

3.5 MODELLING OF SAQDs

In order to utilise fully the unique properties of QDs, knowledge of the electronic structure is not only of fundamental interest but it is also necessary for theoretical description of the electronic properties of QDs and the fabrication of nano-devices with properties designed for a specific application.

Various approaches have been used to perform theoretical modelling of SAQDs systems, ranging from first principle calculations to empirical models. Empirical models are more widely used as compared to first principle calculations as they are less computationally demanding. One of the most widely used empirical models is the multiband effective mass approximation, which is also known as the envelope function approximation (EFA) or multiband ***k·p*** model. It was originally developed by *Luttinger and Kohn* for analysing hole states around defects and/or impurities in semiconductors [49]. It has later been heuristically generalised to include the conduction band and applied to semiconductor heterostructures where the carrier confinement is due to the material dependence of band edges and strain effects. The EFA or multiband ***k.p*** model has been used for the modelling of a wide range of III-V compound semiconductor QWs [50,51], quantum wires (QWRs) [52,53] and QDs [54-56]. The model parameters originate still always from fitting the pertinent bulk materials to experimental or theoretical band gap and effective mass values.

In this thesis, the geometry of the SAQDs structure consists of piecewise continuous material regions, where each partial volume of a semiconductor is modelled with the pertinent bulk band parameters. It is assumed that the electron and hole confinement potential is a gentle perturbation on the pertinent bulk reference potential.

The strain field plays a very significant role in the fabrication of SAQDs. Strain fields inside SAQD structures strongly affect the electronic band structure, which in turn, strongly affects the performance of the optoelectronic devices. It is well known that strain will modify energy gaps and remove degeneracy. The strain induced band lineups can be calculated based on the model solid theory proposed by Van de Walle [57] and standard-deformation-potential theory [58]. The single particle states can be calculated by using strain dependent ***k·p*** method [59].

References:

[1] I. Vurgaftman, J. R. Meyer, and L. R. Ram-Mohan, J. Appl. Phys. **89**, 5815 (2001).

[2] S. Tiwari and D. J. Frank, Appl. Phys. Lett. **60**, 630 (1992).

[3] C. G. Van de Walle, Phys. Rev. B **39**, 1871 (1989).

[4] Y. Arakawa and H. Sakaki, Appl. Phys. Lett. **40**, 939 (1982).

[5] N. Kirstaedter, N. N. Ledentsov, M. Grundmann, D. Bimberg, V. M. Ustinov, S. S. Ruvimov, M. V. Maximov, P. S. Kop'ev, Zh. I. Alferov, U. Richter, P. Werner, U. Gösele, and J. Heydenreich, Electron. Lett. **30**, 1416 (1994).

[6] Z. Zhao, M. Arrandale, O. Vassiltsova, M. A. Petrukhina, and M. A. Carpenter, Proc. IMechE Vol. 221 Part N: J. Nanoengineering and Nanosystems, 73 (2008).

[7] N. Yamamoto, K. Akahane, S. –I. Gozu, A. Ueta, and N. Ohtani, Physica E **32**, 516 (2006).

[8] D. G. Deppe and D. L. Huffaker, Appl. Phys. Lett. **77**, 3325 (2000).

[9] V. M. Ustinov and A. E. Zhukov, Semicond. Sci. Technol. **15**, R41 (2000).

[10] M. Henini and M. Bugajski, Microelectronics Journal **36**, 950 (2005).

[11] T. W. Berg and J. Mørk, IEEE J. Quantum Electron. **40**, 1527 (2004).

[12] S. Chakrabarti, A. D. Stiff-Roberts, X. H. Su, P. Bhattacharya, G. Ariyawansa, and A. G. U. Perera, J. Phys. D: Appl. Phys. **38**, 2135 (2005).

[13] A. Krier and X. L. Huang, Physica E **15**, 159 (2002).

[14] Z. Yuan, Science **195**, 102 (2002).

[14] D. P. DiVincenzo, D. Bacon, J. Kempe, G. Burkard, and K. B. Whaley, Nature **408**, 339 (2000).

[16] M. Bayer, P. Hawrylak, K. Hinzer, S. Fafard, M. Korkusinski, Z. R. Wasilewski, O. Stern, and A. Forchel, Science **291**, 451 (2001).

[17] G. Bester, J. Shumway, and A. Zunger, Phys. Rev. Lett. **93**, 047401 (2004)

[18] R. Steffen, Th. Koch, J. Oshinowo, F. Faller, and A. Forchel, Appl. Phys. Lett. **68**, 223 (1996).

[19] T. Fukui, S. Ando, Y. Tokura, and T. Toriyama, Appl. Phys. Lett. **58**, 2018 (1991).

[20] R. M. Biefeld, Materials Science and Engineering: R: Reports **36**, 105 (2002).

[21] S. J. Kim, *Real-Time Characterization of III-V Compound Semiconductor Epitaxy: Application to '6.1' Materials*. (USA: North Carolina State University, PhD diss., 2004).

[22] N. Bertru, O. Brandt, M. Wassermeier, and K. Ploog, Appl. Phys. Lett. **68**, 31 (1996).

[23] A. F. Tsarsul'nikov, N. N. Ledentsov, M. V. Maksimov, B. Ya. Mel'tser, P. V. Neklyudov, S. V. Shaposhnikov, B. V. Volovik, I. L. Krestnikov, A. V. Sakharov, N. A. Bert, P. S. Kop'ev, Zh. I. Alferov, and D. Bimberg, Semiconductors **31**, 55 (1997).

[24] A. F. Tsarsul'nikov, S. V. Ivanov, P. S. Kop'ev, A. K. Kryganovskii, N. N. Ledentsov, M. V. Maksimov, B. Ya. Mel'tser, P. V. Nekludov, A. A. Suvorova, A. N. Titkov, B. V. Volovik, M. Grundmann, D. Bimberg, and Zh. I. Alferov, J. Elect. Materials **27**, 414 (1998).

[25] E. Alphandéry, R. J. Nicholas, N. J. Mason, and B. Zhang, P. Möck, and G. R. Booker, Appl. Phys. Lett. 74, 2041 (1999).

[26] P. Möck, G.R. Booker, N.J. Mason, R.J. Nicholas, E. Alphandéry, T. Topuria, N.D. Browning, Mat. Sci. Eng. B **80**, 112 (2001).

[27] E. Alphandéry, R. J. Nicholas, N. J. Mason, S. G. Lyapin, and P. C. Klipstein, Phys. Rev. B **65**, 115322 (2002).

[28] R.A. Child, R.J. Nicholas, N.J. Mason, E. Alphandéry, Physica E **13**, 241 (2002).

[29] R. A. Child, R. J. Nicholas, N. J. Mason, P. A. Shields, J. –P. R. Wells, I. V. Bradley, J. Phillips, and B. N. Murdin, Phys. Rev. B **68**, 165307 (2003)

[30] P. A. Shields, C. W. Bumby, L. J. Li, and R. J. Nicholas, J. Appl. Phys. **96**, 2725 (2004).

[31] R.J. Nicholas, P.A. Shields, R.A. Child, L.J. Li, E. Alphandéry, N.J. Mason, C. Bumby, Physica E **20**, 204 (2004).

[32] E. R. Glaser, B. R. Bennett, B. V. Shanabrook, and R. Magno, Appl. Phys. Lett. **68**, 3614 (1996).

[33] B. R. Bennett, B. V. Shanabrook, P. M. Thibado, L. J. Whitman, and R. Magno, J. Cryst. Growth **175/176**, 888 (1997).

[34] A. F. Tsarsul'nikov, N. N. Ledentsov, M. V. Maksimov, B. Ya. Mel'tser, P. V. Neklyudov, S. V. Shaposhnikov, B. V. Volovik, I. L. Krestnikov, A. V. Sakharov, N. A. Bert, P. S. Kop'ev, Zh. I. Alferov, and D. Bimberg, Semiconductors **31**, 55 (1997).

[35] A. Krier, X. L. Huang, and A. Hammiche, J. Phys. D: Appl. Phys. **34**, 874 (2001).

[36] M. Hayne, J. Maes, S. Bersier, V. V. Moshchalkov, A. Schliwa, L. Müller-Kirsch, C. Kapteyn, R. Heitz, and D. Bimberg, Appl. Phys. Lett. **82**, 4355 (2003).

[37] J. C. Ferrer, F. Peiró, A. Cornet, J. R. Morante, T. Uztmeier, G. Armelles, and F. Briones, Appl. Phys. Lett. **69**, 3887 (1996).

[38] Y. Qiu, D. Uhl, and S. Keo, Appl. Phys. Lett. **84**, 263 (2004).

[39] Y. Qiu and D. Uhl, Appl. Phys. Lett. **84**, 1510 (2004).
[40] A. Krier, X. L. Huang, and A. Hammiche, Appl. Phys. Lett. **77**, 3791 (2000).
[41] A. Krier and X. L. Huang, Physica E **15**, 159 (2002)
[42] S. V. Ivanov, A. N. Semenov, V. A. Solov'ev, O. G. Lyublinskaya, Ya. V. Terent'ev, B. Ya. Meltser, L. G. Prokopova, A. A. Sitnikova, A. A. Usikova, A. A. Toropov, and P. S. Kop'ev, J. Cryst. Growth **278**, 72 (2005).
[43] V. A. Solov'ev, O. G. Lyublinskaya, A. N. Semenov, B. Ya. Meltser, D. D. Solnyshkov, Ya. V. Terent'ev, L. A. Prokopova, A. A. Toropov, S. V. Ivanov, and P. S. Kop'ev, Appl. Phys. Lett. **86**, 011109 (2005).
[44] S. V. Ivanov, A. N. Semenov, O. G. Lyublinskaya, B. Ya. Meltser, V. A. Solov'ev, Ya. V. Terent'ev, A. A. Sitnikova, and P. S. Kop'ev, Proceeding of the 12th International Conference on Narrow Gap Semiconductors, Toulouse, 2005
[45] A. N. Semenov, V. A. Solov'ev, B. Ya. Meltser, O. G. Lyublinskaya, Ya. V. Terent'ev, A. A. Sitnikova, and S. V. Ivanov, Acta Physica Polonica A **108**, 859 (2005)
[46] C. Cornet, f. Doré, A. Ballestar, J. Even, N. Bertru, A. Le Corre, and S. Loualiche, J. Appl. Phys. **98**, 126105 (2005)。
[47] C. E. Pryor and M-. E. Pistol, Phys. Rev. B **72**, 205311 (2005).
[48] S. Shusterman, Y. Paltiel, A. Sher, V. Ezersky, Y. Rosenwaks, J. Cryst. Growth, **291**, 363 (2006).
[49] J. M. Luttinger and W. Kohn, Phys. Rev. **97**, 869 (1955).
[50] A. T. Meney, B. Gonul, and E. P. O'Reilly, Phys. Rev. B **50**, 10893 (1994).
[51] J. Los, A. Fasolino, nd A. Catellani, Phys. Rev. B **53**, 4630 (1996).
[52] P. C. Sercel and K. J. Vahala, Phys. Rev. B. **42**, 3690 (1990).
[53] O. Stier and D. Bimberg, Phys. Rev. B. **55**, 7726 (1997).
[54] M. Holm, M. –E. Pistol, and C. Pryor, J. Appl. Phys. **92**, 932 (2002).
[55] R. Heitz, O. Stier, I. Mukhametzhanov, A. Madhukar, and D. Bimberg, Phys. Rev. B. **62**, 11017 (2000).
[56] E. P. Pokatilov, V. A. Fonoberov, V. M. Fomin, and J. T. Devreese, Phys. Rev. B. **64**, 245328 (2001).
[67] C. G. Van de Walle, Phys. Rev. B **39, 1**871 (1989).
[58] S. –H. Wei and A. Zunger, Phys. Rev. B **49**, 14337 (1994).
[59] C. Pryor, M. –E. Pistol, and L. Samuelson, Phys. Rev. B **56**, 10404 (1997).

CHAPTER 4

RESEARCH METHODS

4.0 INTRODUCTION

This research concerns both theoretical and experimental works. The details of the methodology of the theoretical calculations and experimental methods for QDs structures are outlined in this chapter. First, the strain-field calculation using finite element method (FEM) is outlined, followed by the strain-induced band profile calculations based upon model-solid theory and standard-deformation-potential. Finally, the 6-band strain dependent ***k·p*** model for electronic structure calculation is addressed. Knowledge of the electronic structure is necessary for theoretical description of the electronic properties of QDs and for fabrication of nano-devices with designed properties. Experimental study is concerning the optical studies of self-assembled SAQDs. PL measurement setup and procedures also will be described in this chapter. The PL measurement is carried out by utilising FTIR spectroscopy.

4.1 MODELLING METHODS

The modelling consists of three distinct steps. The strain distribution for the dot and surrounding matrix is obtained using FEM in the continuum-elasticity approximation. Next, standard deformation-potential theory is used to obtain the strain-modified band profile. After that, the size quantisation energy for holes is calculated using the 6-band ***k·p*** method and anisotropic effective mass approximation for electron levels. The effect of piezoelectricity was not included because the dot sizes considered here are very small. The material parameters used in the modelling listed in Table 4.1 were taken from Ref. [1], unless noted otherwise. Note also that all band energies and eigenenergies in our paper are given with respect to the valence band edge for unstrained InSb, as in Ref. [1].

Parameters	InSb	GaSb	InAs	GaAs
a (Å)	6.4794	6.0959	6.0583	5.65325
E_g^{Γ} (eV)	0.235	0.812	0.417	1.519
Δ (eV)	0.81	0.76	0.39	0.341
m_e^*	0.0135	0.039	0.026	0.067
γ_1	34.8	13.4	20.0	6.98
γ_2	15.5	4.7	8.5	2.06
γ_3	16.5	6.0	9.2	2.93
E_P (eV)	23.3	27.0	21.5	28.8
VBO (eV)	0	-0.03	-0.59	-0.8
a_c (eV)	-6.94	-7.5	-5.08	-7.17
a_v (eV)	-0.36	-0.8	-1.0	-1.16
b (eV)	-2.0	-2.0	-1.8	-2.0
d (eV)	-4.7	-4.7	-3.6	-4.8
c_{11} (GPa)	68.47	88.42	83.29	122.1
c_{12} (GPa)	37.35	40.26	45.26	56.6
c_{44} (GPa)	31.11	43.22	39.59	60.0

Table 4.1 : Band structures parameters for InSb, GaSb, InAs, and GaAs. [1]

4.1.1 MODELLING OF THE STRAIN FIELDS

Various techniques have been used for studying the strain fields in SAQDs and the surrounding matrix. They range from an analytical continuum approach based on Eshelby's inclusion theory [2,3] to atomistic approach utilizing valence force field model with Keating potential. [4-7] For numerical approaches based on the continuum-elasticity approximation, both the finite difference method [8,9] and the FEM [2,10-15] have been used. Previous studies have shown that the continuum-elasticity approximation is applicable at the nanoscale even though it was developed for macroscopic structures. The modelling results compare well with the data obtained from transmission electron microscopy (TEM) imaging. [16,17] The flexibility of FEM meshing enables us to analyse SAQDs of arbitrary shape and material composition with acceptable computational cost.

Solution of full 3-D problems is computationally expensive and memory consuming. Therefore, many of previous studies simplify the problem geometry into 2D

axial symmetric geometry e.g. conical shape [14,15,17] and lens shape [18]. Nevertheless, the use of 2-D axial symmetric model would be an appropriate simplification and approximation with reasonable accuracy but there are a few drawbacks, namely, only the strain in a single plane can be studied. Further more it may not represent the pyramidal or truncated pyramidal shape very well and it overlooks the symmetry property of zinc-blende crystal structure of semiconductor materials.

With more powerful desktop computers, having faster multicore processors and higher memory capacity, the modelling of full 3-D models has become viable. In this work, the numerical FEM modelling of the strain field was performed using 2-D axial symmetry model during the preliminary stage. The purpose of this preliminary stage is to verify the validity of the modelling approach. After that, the full 3-D model is used to perform the modelling of the strain field for the SAQD systems of interest, i.e. InSb/GaSb and $InAs_xSb_{(1-x)}$/InAs system.

The strain distribution is determined using continuum elasticity theory by minimizing the total elastic energy for a cubic symmetry crystal [19,20]. To characterize the strain variation with QD shape, which also takes into account the strain redistribution between matrix and inclusion, we have calculated the elastic energy density. Elastic (strain) energy can be expressed as:

$$F = \tfrac{1}{2} c_{11}\left(e_{xx}^2 + e_{yy}^2 + e_{zz}^2\right) + c_{12}\left(e_{xx}e_{yy} + e_{xx}e_{zz} + e_{yy}e_{zz}\right) + 2c_{44}\left(e_{xy}^2 + e_{xz}^2 + e_{yz}^2\right)$$

$$= \tfrac{1}{2}\left(ke_A^2 + \mu_1(e_{E1}^2 + e_{E2}^2) + \mu_2(e_{T1}^2 + e_{T2}^2 + e_{T3}^2)\right) \qquad (4.1)$$

The fist equality is a standard form of elastic free energy [21]. The second equality presents the same in a diagonal form. The latter can be obtained from symmetry arguments on base of irreducible representations of cubic group [22] or directly from Eq. (4.1) and the definition of $F = 1/2\,\sigma_{ij}e_{ij}$ (see Eq. 4.16). The diagonal representation of elastic energy is more convenient for the present analysis because it uses the same symmetrised strain components as the deformation potential theory, as follows:

$e_A = e_{xx} + e_{yy} + e_{zz}$ (hydrostatic strain component), (4.2)

$e_{E1} = e_{xx} - e_{yy}$ (orthorhombic shear strain components), (4.3)

$e_{E2} = \tfrac{1}{\sqrt{3}}\left(2e_{zz} - e_{xx} - e_{yy}\right)$ (tetragonal shear strain components), and (4.4)

$e_{T1} = 2e_{xy}$, $e_{T2} = 2e_{xz}$, $e_{T3} = 2e_{yz}$ (rhombohedral/trigonal shear strain component).(4.5)

Without any external forces, the lattice mismatch between the matrix and dot materials is the sole cause of strains throughout the system. The strain is given in terms of the displacement vector as follows:

$$e_{ij} = \frac{1}{2}\left(\partial_i u_j + \partial_j u_i\right) \tag{4.6}$$

where $u_{i,j}$ is the displacement vector. The total elastic energy, F is minimised with respect to $u_{i,j}$ throughout the entire solution space. From the resulting $u_{i,j}$, e_{ij} can be readily calculated using Equation 4.6.

4.1.1.1 NUMERICAL MODELLING OF STRAIN FIELD

The strain distribution for arbitrary QD shape treated in the anisotropic continuum-elasticity is available only by numerical methods. A standard FEM is employed, which allows accounting of a realistic cubic elastic anisotropy and the difference in elastic constants of dot and matrix materials. The comparison of the continuum elasticity approach with more realistic atomistic elasticity for strain calculation in QD has revealed a good correspondence of both methods [23]. The discrepancies were observed only within one interatomic distance around the heterointerface, which became essential only for extremely small QD sizes.

In FEM, the degree of freedom (DOF) or the translation displacements are expressed as an interpolation of nodal displacements by the shape functions as follows if we consider a 2-D model [24]:

$$\begin{Bmatrix} u_x \\ u_y \end{Bmatrix} = [N]\{u\}_e \tag{4.7}$$

where, $$[N] = \begin{bmatrix} N_1 & 0 & N_2 & 0 & N_3 & 0 & N_4 & 0 \\ 0 & N_1 & 0 & N_2 & 0 & N_3 & 0 & N_4 \end{bmatrix} \tag{4.8}$$

is the shape function matrix and

$$\{u\}_e^T = \{u_{x1} \quad u_{y1} \quad u_{x2} \quad u_{y2} \quad u_{x3} \quad u_{y3} \quad u_{x4} \quad u_{y4}\} \tag{4.9}$$

are nodal displacements.

The shape function N_j take the usual form of a bi-linear, quadrilateral element as [24]:

$$N_j = \frac{1}{4}(1+\xi_j\xi)(1+\eta_j\eta) \tag{4.10}$$

where ξ and η are the natural coordinates.

The general equation of motion can be obtained by using Langrange's equation, which takes the general form of

$$\frac{d}{dt}\left(\frac{\partial T}{\partial q_j}\right)+\frac{\partial D}{\partial q_j}+\frac{\partial U}{\partial q_j}=Q_{j,} \qquad j = 1,2,\ldots\ldots,n \tag{4.11}$$

where T is the kinetic energy of the system, U is the strain energy of the system, D is a dissipation function, q_j are the generalized displacements, and Q_j are the generalized forces. However, since the problem here is a static problem, the terms involving the kinetic energy can be omitted. There is also no need for dissipation function since we assume that the structural damping of the material used can be neglected. Therefore, Equation (4.7) is substituted into the general constitutive equation

$$\sigma = Ce + e_{th}(e_0) \tag{4.12}$$

where, C = matrix containing material properties,

$e_{th}(e_0)$ = thermal strain (initial strain).

Equation (4.12) is further used in the Langrange equation in (4.11), gives the final form of the equation for each element

$$[k]_e\{u\}_e = \{f\}_e \tag{4.13}$$

where $[k]_e$ = element stiffness matrix,

$\{u\}_e$ = element displacement vector, and

$\{f\}_e$ = element force vector.

The matrix equations for all the elements are assembled to give

$$[K]\{u\} = \{f\} \tag{4.14}$$

where $[K]$ = global stiffness matrix,

$\{u\}$= global displacement vector, and

$\{f\}$ = global force vector

Two FEM packages, ANSYS and Comsol Multiphysics, were used to perform the modelling. To start off, the calculation is performed with the following simplifications:

- Single isolated QD, which ignores the dot to dot elastic interactions in multiple dots structure.
- Assuming infinite matrix in which the outer boundaries are strain free.
- Geometry simplification such as 2-D axisymmetric model of conical and truncated conical shape QD.
- Assuming isotropic materials for both the QDs and the matrix. The material parameters used in the isotropic approximation are listed in Table 4.2 below.

Parameters	InSb [25]	GaSb [25]	InAs [24]	GaAs [24]
Young's Modulus (GPa)	40.9	63.1	51.3	85.5
Poisson's ratio	0.35	0.31	0.354	0.316

Table 4.2 : Material parameter for InSb, GaSb, InAs, and GaAs used in isotropic model.

Comparisons between the strain field obtained by using ANSYS and Comsol Multiphysics are carried out. In addition, comparison between the results obtained from 2-D and 3-D model by using Comsol Multiphysics is also performed. Investigation of the effects of island shape, size and height on the strain field are also carried. The analysis of using isotropic properties and anisotropic properties of the SAQDs systems is also carried out.

4.1.1.1.1 2-D Axial Symmetry Model

The 2-D axial symmetry model is sufficient to provide an insight picture of stress and strain characteristic of the QD with less intensive computation and memory consumption but it only reflects the stress and strain characteristics in one plane. The FEM modelling was carried out for two types of island shapes shown in Figure 4.1 below; one conical dot and one truncated cone with four types of structures. The substrate thickness was chosen to be 50 nm. Dot height, h = 6 nm, dot half-width, e = 12 nm, and substrate half-width, l = 50 nm have been kept constant. In the truncated conical case, the island top surface half-width, e' = 6 nm. For the model containing a wetting layer, the thickness of the wetting layer is taken to be 1 nm and for the models that contain the cap layer and the structure containing both a wetting layer and a cap layer, the whole structure is taken to be 100 nm. A 2-D section of half the sample, as

shown in Figure 4.1, is modelled and the axial symmetry about the cone axis is incorporated into the calculations to represent the 3-D sample.

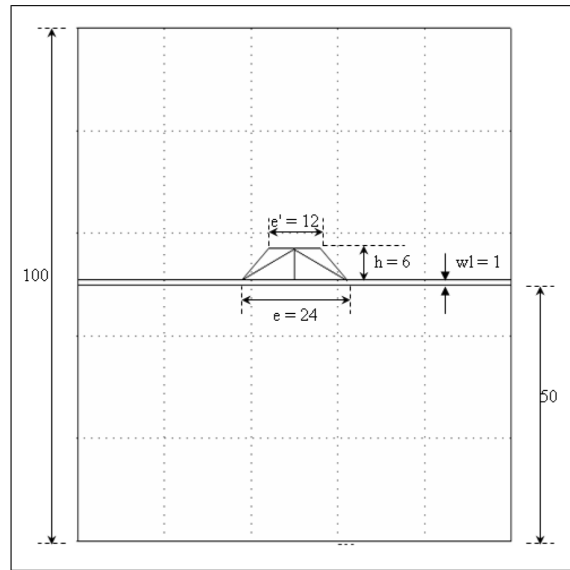

Figure 4.1 : Schematic View of the Dots Studied by FEM Calculations

The calculation is performed for various structures, such as:

- Substrate and dot; uncapped
- Substrate, wetting layer and dot; uncapped
- Substrate, dot and capped
- Substrate, wetting layer, dot and capped

4.1.1.1.2 3-D Model

The 2-D axial symmetric model described in the previous section is capable of modelling a conical or truncated conical shaped dot effectively. However, it would be insufficient for modelling the highly asymmetric dot shapes such as a pyramidal dot. Besides, one is not able to study the stress or strain distribution in any other arbitrary plane of the basic unit of the QD structure in a 2-D model. Having a 3-D model, however, allows the analysis of the stress and/or strain distribution in any arbitrary plane of the QD heterostructure to be performed.

The FEM formulation for 3-D model is similar to the 2-D case. The displacements are also interpolated from the nodal displacements using the shape

functions [24]. The 3-D elements have three degrees of freedom per node as opposed to the two degrees of freedom in the 2-D elements. The shape functions for 3-D model with trilinear, quadrilateral 8 nodes element in terms of natural coordinates take on the form [24]:

$$N_j = \frac{1}{8}\left(1 + \xi_j \xi\right)\left(1 + \eta_j \eta\right)\left(1 + \zeta_j \zeta\right). \quad (4.15)$$

The same method as in 2-D case is used to obtain the FE equations.

4.1.1.2 ANALYTICAL APPROACH TO THE ELASTICITY PROBLEM

For the ellipsoidal QD, we have used the analytical approach to the elastic problem in parallel with the FEM. The relevance of the approximation of the QD shape by ellipsoid will be discussed in Chapter 6. At this step we would like just to point out two important properties of ellipsoidal shape.

First, an elastic problem of ellipsoidal inclusion has a simple algebraic solution in the isotropic elasticity approximation. This is a well-known solution by *Eshelby* [3]. It provides a strain distribution inside the inclusion and at the heterointerface, which is a usual practical concern for quantisation potential analysis. Thus, the extensive numerical calculations are not necessary and a broad range of material parameters is easily available for analysis.

Second, when the results of modelling are expressed in the form of some characteristic values of band edges within the QD (for example, as an effective confinement potential which can be later applied for the estimation of quantised electron /hole levels), the ellipsoidal model naturally provides a single-valued result which is connected to the homogeneous strain condition within the ellipsoidal inclusion [3]. Otherwise, for any other shape, the strain and hence the strain-induced band shifts, are varied across the QD, and the effective potential can be estimated only through some kind of numerical averaging over the QD volume.

The relevant expressions for six components of strain tensor adopted for the case of oblate ellipsoid are outlined in Appendix 1. These expressions present a basis for elastic calculations within proposed isotropic ellipsoidal (IE) model. They take as parameters the elastic constants of the matrix and inclusion (QD) materials in the

isotropic approximation. We remind that isotropic elasticity requires only two independent elastic modules (bulk and shear modules or Lame coefficients) instead three in cubic anisotropy. Thus, a way of how the cubic elastic symmetry can be adopted in isotropic approximation needs some justification. It is known that Hook's law can be presented for cubic symmetry in the following form [21,26]:

$$\begin{aligned}\sigma_{ij} &= ke + 2\mu_1 {}^{/}e_{ij} \quad (i = j) \\ &= 2\mu_2 {}^{/}e_{ij} \qquad\; (i \neq j)\end{aligned}, \tag{4.16}$$

where $k = (c_{11} + 2c_{12})/3$, $\mu_1 = (c_{11} - c_{12})/2$ and $\mu_2 = c_{44}$.

Here k and $\mu_{1,2}$ are bulk and shear moduli respectively; $e = e_{xx} + e_{yy} + e_{zz}$ and ${}^{/}e_{ij} = e_{ij} - \frac{1}{3}e\delta_{ij}$ are dilatational and deviatoric parts of the strain tensor; c_{ij} are three independent stiffness constants for cubic symmetry crystals. For the case of (001) growth plane, the $i \neq j$ components of strain tensor are identically zero [3] within the ellipsoidal QD, i.e. deformation is purely tetragonal. Hence, the k and μ_1 are naturally two independent elastic coefficients for isotropic approximation within QD. For the (111) growth plane the situation is similar, with μ_2 replacing μ_1. For any other growth direction, the bulk modulus stands but the shear moduli are not separable. A similar complication exists for the matrix material, where all the strain components are generally nonzero and some approximation for shear modulus is needed. In the present calculations, a direct averaging of shear modulus in matrix was employed as follows [27]:

$$\mu_a = \frac{1}{5}(c_{11} - c_{12}) + \frac{3}{5}c_{44} \ . \tag{4.17}$$

Once strain components are obtained, the calculation of strain-induced shifts/splitting of band edges is straightforward using Equation (4.20) in Section 4.1.2. We would like to note that condition of homogeneous hydrostatic plus tetragonal (e_{xx}=e_{yy}) (or hydrostatic plus trigonal for (111) plane) strain within oblate ellipsoid make these calculations very simple even for the valence band.

4.1.1.3 MODELLING THE LATTICE MISMATCH

The lattice mismatch between the two materials is responsible for the formation of QD island. For QD heterostructures with a uniform composition, the mismatch of the lattice constants of different crystals can be defined as

$$e_0 = \frac{a_d - a_m}{a_m} \quad (4.18)$$

where a_d and a_m are the lattice constants of the dot and matrix respectively. There is another definition of the lattice mismatch in QD heterostructures that also in use, which is

$$e_0 = \frac{a_m - a_d}{a_d} \quad (4.19)$$

The lattice mismatch can be regarded as a kind of eigenstrain that is commonly used in the mechanics of composite materials to simulate the thermal expansion, phase deformation or treated as the initial strain in the QD systems.

Both of the above definitions of the lattice mismatch are used in this thesis. In the model validation stage, the former definition is used as this is the definition often used in the literature. The latter definition is used for the actual modelling of the SAQD systems of interest in this thesis. This is because the latter definition is more straight forward and meaningful in defining the lattice mismatch of the strained heterostructures.

4.1.2 STRAIN MODIFIED BAND PROFILE

Strain changes the lattice constant and reduces the symmetry of the crystal and therefore, the band structure of semiconductors is altered by the presence of strain. It is well known that strain will modify energy gaps and removes degeneracy. The strain induced band lineups are calculated based on the model solid theory proposed by Van de Walle [28] and the standard-deformation-potential theory.

The introduction of homogeneous strain in bulk semiconductors changes the lattice parameter and in some cases, the symmetry of the material. These in turn produce significant changes in the electronic band structure. Homogeneous strained configuration can quite generally be divided into two configurations: the hydrostatic component that gives rise to a volume change without disturbing the symmetry and the shear component that in general reduces the symmetry present in the strain-free lattice. A homogeneous strain induces change in energy gaps and when the symmetry of the crystal is reduced, removes degeneracies.

The total effects of strain on the band edges can be described as follows [29]:

$$H_{total} = H_0 + H_S + H_{SO} \tag{4.20}$$

where, H_0 is the energy levels without strain and spin-orbit splitting, H_S is the term describing strain effects and H_{SO} include the effects of spin-orbit splitting.

The strain Hamiltonian, H_S for the i-th band at $\boldsymbol{k}$=0 can be written as [30,31]:

$$H_S^i = a_i(e_{xx} + e_{yy} + e_{zz}) - 3b_i\left[\left(L_X^2 - \tfrac{1}{3}\mathbf{L}^2\right)e_{zz} + c.p.\right] - \sqrt{3}d_i\left[\left(L_X L_Y + L_y L_X\right)e_{xy} + c.p.\right] \tag{4.21}$$

where, a_i is the hydrostatic deformation potential, while b_i and d_i are uniaxial deformation potentials for the *i*-th band. **L** is the angular momentum operator and the *c.p.* denotes cyclic permutations with respect to the indices x, y, and z.

The conduction band is assumed to be decoupled from the valence band. The energy minimum of *i*-th conduction band valley (i.e. $\boldsymbol{X}$, $\boldsymbol{L}$, or $\boldsymbol{\Gamma}$), $E_{c,\alpha}^i$, is determined by adding the shift of the minimum due to strain, $\Delta E_{c,\alpha}^i$, to the position of the conduction band minimum in bulk material, $E_{\alpha,av}^0$, where

$$E_{\alpha,av}^0 = E_{g,\alpha}^0 + \frac{\Delta}{3} + E_{v,av}, \text{ and}$$

$$E_{c,\alpha}^i = \Delta E_{c,\alpha}^i + E_{\alpha,av}^0. \tag{4.22}$$

$E_{v,av}$ is the average energy of valence band maxima at $\boldsymbol{\Gamma}$-point set on an absolute scale, while $E_{g,\alpha}^0$ is the band gap of type α in relaxed bulk material. The $\Delta E_{c,\alpha}^i$ can be written as [28,32]:

$$\Delta E_{c,\alpha}^i = \left[\Xi_d^\alpha \overleftrightarrow{1} + \Xi_u^\alpha \hat{a}_i \hat{a}_i\right] : \vec{e}, \tag{4.23}$$

where $\overleftrightarrow{1}$ is the unit tensor, $\vec{e}$ is the strain tensor, $\hat{a}_i$ is the unit vector to the *i*-th valley, and Ξ_d^α and Ξ_u^α are the deformation potentials for α conduction band. The degeneracies of $\boldsymbol{L}$- and $\boldsymbol{X}$-conduction band are usually split by non-hydrostatic strain. However, the conduction minima at $\boldsymbol{\Gamma}$-valley is only subject to hydrostatic strain shifts proportional to the fractional volume change as follow:

$$H_S^{c,\Gamma} = a_c\left(e_{xx} + e_{yy} + e_{zz}\right), \tag{4.24}$$

where a_c is the hydrostatic deformation-potential of a conduction band. a_c can also be denoted as

$$a_c = \Xi_d^\Gamma + \frac{1}{3}\Xi_u^\Gamma. \tag{4.25}$$

In the valence band, the orbital-strain Hamiltonian, H_S^V for a given band at the Γ-point is composed of hydrostatic, shear tetragonal, and shear rhombohedral strain components [29] as follow:

$$H_S^V = a_V\left(e_{xx}+e_{yy}+e_{zz}\right) - b\left[\begin{pmatrix} -2 & 0 & 0 \\ 0 & 1 & 0 \\ 0 & 0 & 1 \end{pmatrix} e_{xx} + \begin{pmatrix} 1 & 0 & 0 \\ 0 & -2 & 0 \\ 0 & 0 & 1 \end{pmatrix} e_{yy} + \begin{pmatrix} 1 & 0 & 0 \\ 0 & 1 & 0 \\ 0 & 0 & -2 \end{pmatrix} e_{zz}\right]$$
$$-\sqrt{3}d\left[\begin{pmatrix} 0 & -1 & 0 \\ -1 & 0 & 0 \\ 0 & 0 & 0 \end{pmatrix} e_{xy} + \begin{pmatrix} 0 & 0 & 0 \\ 0 & 0 & -1 \\ 0 & -1 & 0 \end{pmatrix} e_{yz} + \begin{pmatrix} 0 & 0 & -1 \\ 0 & 0 & 0 \\ -1 & 0 & 0 \end{pmatrix} e_{xz}\right] \tag{4.26}$$

where a_v is hydrostatic deformation potential, b and d are shear deformation potentials for valence band. Equation 4.26 can be further simplified, which gives:

$$H_S^V = a_V\left(e_{xx}+e_{yy}+e_{zz}\right) + \begin{bmatrix} b_{xx} & d_{xy} & d_{xz} & 0 & 0 & 0 \\ d_{xy} & b_{yy} & d_{yz} & 0 & 0 & 0 \\ d_{xz} & d_{yz} & b_{zz} & 0 & 0 & 0 \\ 0 & 0 & 0 & b_{xx} & d_{xy} & d_{xz} \\ 0 & 0 & 0 & d_{xy} & b_{yy} & d_{yz} \\ 0 & 0 & 0 & d_{xz} & d_{yz} & b_{zz} \end{bmatrix} \tag{4.27}$$

where, $b_{xx} = b(2e_{xx} - (e_{yy}+e_{zz}))$,

$b_{yy} = b(2e_{yy} - (e_{xx}+e_{zz}))$,

$b_{zz} = b(2e_{zz} - (e_{yy}+e_{xx}))$,

$d_{xy} = \sqrt{3}de_{xy}$,

$d_{xz} = \sqrt{3}de_{xz}$, and

$d_{yz} = \sqrt{3}de_{yz}$. (4.28)

The spin-orbit coupling Hamiltonian in the Cartesian representation (x↑, y↑, z↑, x↓, y↓, z↓) is not block diagonal, so a full 6x6 matrix has to be used to represent the spin-orbit Hamiltonian [29], that is:

$$H_{SO} = \frac{1}{3}\Delta\begin{bmatrix} 0 & -i & 0 & 0 & 0 & 1 \\ i & 0 & 0 & 0 & 0 & -i \\ 0 & 0 & 0 & -1 & i & 0 \\ 0 & 0 & -1 & 0 & i & 0 \\ 0 & 0 & -i & -i & 0 & 0 \\ 1 & i & 0 & 0 & 0 & 0 \end{bmatrix} \tag{4.29}$$

where Δ is spin-orbit splitting energy.

In constructing the total Hamiltonian H_T, the assumption that the contributions from the elastic strain and the spin-orbit coupling are additive is made. Hence,

$$H_{total} = a_v\left(e_{xx} + e_{yy} + e_{zz}\right) + \begin{bmatrix} b_{xx} & -i\Delta/3 + d_{xy} & d_{xz} & 0 & 0 & \Delta/3 \\ i\Delta/3 + d_{xy} & b_{yy} & d_{yz} & 0 & 0 & -i\Delta/3 \\ d_{xz} & d_{yz} & b_{zz} & -\Delta/3 & i\Delta/3 & 0 \\ 0 & 0 & -\Delta/3 & b_{xx} & i\Delta/3 + d_{xy} & d_{xz} \\ 0 & 0 & -i\Delta/3 & -i\Delta/3 + d_{xy} & b_{yy} & d_{yz} \\ \Delta/3 & i\Delta/3 & 0 & d_{xz} & d_{yz} & b_{zz} \end{bmatrix} \quad (4.30)$$

Diagonalisation of Equation 4.30 yields the positions of the three degenerate valence bands (the light hole (E_{vlh}), heavy hole (E_{vhh}), and split-off (E_{vso}) band) at Γ-point of the QD structure subject to an arbitrary uniform deformation. These bands are strictly degenerate only in the absence of strain and spin-orbit splitting. The average of these bands is referred to as $E_{v,av}$. When no strain is present, spin-orbit effects raise E_{vlh} and E_{vhh} with respect to E_{vso}. Shear components (tetragonal and trigonal) of the strain lead to additional splitting, which interact with the spin-orbit splitting to produce the final valence bands positions.

For strain along [001] direction, the band edges at Γ-point are expressed as follows by taking $E_{v,av}$ as reference:

Conduction band,

$$E_c(\varepsilon) = E_{v,av} + \Delta/3 + E_g + a_c e_{hyd} \quad (4.31)$$

Heavy-hole energy band,

$$E_{vhh}(\varepsilon) = E_{v,av} + \Delta/3 + a_v e_{hyd} - be_{bi} \quad (4.32)$$

Light-hole energy band,

$$E_{vlh}(\varepsilon) = E_{v,av} - \Delta/6 + a_v e_{hyd} + \tfrac{1}{2}be_{bi} + \tfrac{1}{2}\sqrt{\Delta^2 + 2\Delta be_{bi} + 9\left(be_{bi}\right)^2} \quad (4.33)$$

Split off energy band,

$$E_{vso}(\varepsilon) = E_{v,av} - \Delta/6 + a_v e_{hyd} + \tfrac{1}{2}be_{bi} - \tfrac{1}{2}\sqrt{\Delta^2 + 2\Delta be_{bi} + 9\left(be_{bi}\right)^2} \quad (4.34)$$

where E_g is the unstrained bandgap, e_{hyd} is hydrostatic strain (i.e. $e_{hyd} = e_{xx}+e_{yy}+e_{zz}$) and e_{bi} is biaxial strain (i.e. $e_{bi} = e_{zz} - ½(e_{xx} + e_{yy})$).

4.1.3 ELECTRONIC STRUCTURE

The electronic structure is calculated in the envelope function approximation by decoupling the conduction and valence band. The wetting layer is not included in our calculation because the existence of the wetting layer is not clear. The piezoelectricity effect is not included either because the effect of piezoelectricity on the electronic structure would be unjustified because the dot size is small. The single particle electron state is calculated using a single band anisotropic effective mass approach; which the electron Hamiltonian is [33,34-36]:

$$H_e = E_C - \frac{\hbar^2}{2m_0}\gamma_c\left(\partial_x^2 + \partial_y^2 + \partial_z^2\right) + a_c(e_{xx} + e_{yy} + e_{zz}) \tag{4.35}$$

where $\gamma_c = \frac{m_0}{m^*} - E_P \frac{3E_g + 2\Delta}{3E_g\left(E_g + \Delta\right)}$ (4.36)

a_c is the conduction band hydrostatic deformation potential, e_{ij} are the strain components, m^* is the electron effective mass, E_g is the unstrained band gap, Δ is the spin orbit splitting energy and E_P is a parameter controlling the mixing of the conduction and valence band, related to momentum matrix element, P by

$$E_P = \frac{2m_0}{\hbar^2}P^2 \tag{4.37}$$

For valence band, the following 6X6 ***k·p*** Hamiltonian based on Luttinger-Kohn and Pikus-Bir theory is used [37-39].

$$H_h = H_0 + H_S \tag{4.38}$$

$$H_0 = \begin{pmatrix} -P+Q & -S^* & R & 0 & \sqrt{\frac{3}{2}}S & -\sqrt{2}Q \\ -S & -P-Q & 0 & R & -\sqrt{2}R & \frac{1}{\sqrt{2}}S \\ R^* & 0 & -P-Q & S^* & \frac{1}{\sqrt{2}}S^* & \sqrt{2}R^* \\ 0 & R^* & S & -P+Q & -\sqrt{2}Q & \sqrt{\frac{3}{2}}S^* \\ \sqrt{\frac{3}{2}}S^* & -\sqrt{2}R^* & \frac{1}{\sqrt{2}}S & \sqrt{2}Q & -P-\Delta & 0 \\ -\sqrt{2}Q & \frac{1}{\sqrt{2}}S^* & \sqrt{2}R & \sqrt{\frac{3}{2}}S & 0 & -P-\Delta \end{pmatrix}, \tag{4.39}$$

where

$$P = -E_v - \gamma_1\frac{\hbar^2}{2m_0}\left(\partial_x^2 + \partial_y^2 + \partial_z^2\right),$$

$$Q = -\gamma_2 \frac{\hbar^2}{2m_0}\left(\partial_x^2 + \partial_y^2 - 2\partial_z^2\right),$$

$$R = \sqrt{3}\frac{\hbar^2}{2m_0}\left[\gamma_2\left(\partial_x^2 - \partial_y^2\right) - 2i\gamma_3\partial_x\partial_y\right], \text{ and}$$

$$S = -\sqrt{3}\gamma_3 \frac{\hbar^2}{2m_0}\partial_z\left(\partial_x - i\partial_y\right), \tag{4.40}$$

where γ_i are the Luttinger parameters. The strain dependent coupling is given by

$$H_S = \begin{pmatrix} -p+q & -s^* & r & 0 & \sqrt{\frac{3}{2}}s & -\sqrt{2}q \\ -s & -p-q & 0 & r & -\sqrt{2}r & \frac{1}{\sqrt{2}}s \\ r^* & 0 & -p-q & s^* & \frac{1}{\sqrt{2}}s^* & \sqrt{2}r^* \\ 0 & r^* & s & -p+q & \sqrt{2}q & \sqrt{\frac{3}{2}}s^* \\ \sqrt{\frac{3}{2}}s^* & -\sqrt{2}r^* & \frac{1}{\sqrt{2}}s & \sqrt{2}q & -p & 0 \\ -\sqrt{2}q & \frac{1}{\sqrt{2}}s^* & \sqrt{2}r & \sqrt{\frac{3}{2}}s & 0 & -p \end{pmatrix}, \tag{4.41}$$

where

$$p = a_v\left(e_{xx} + e_{yy} + e_{zz}\right),$$

$$q = b\left[e_{zz} - \frac{1}{2}\left(e_{xx} + e_{yy}\right)\right],$$

$$r = \frac{\sqrt{3}}{2}b\left(e_{xx} - e_{yy}\right) - ide_{xy}, \text{ and}$$

$$s = -d\left(e_{xz} - ie_{yz}\right). \tag{4.42}$$

The material parameters used in the calculations were taken from Ref. [1] and listed in Table 4.1, unless noted otherwise.

4.1.3.1 TEMPERATURE DEPENDENT MODELLING of ELECTRONIC STRUCTURE

In performing the electronic structure modelling, temperature dependence of material parameters have to be taken into account in order to maintain the consistency between the theoretical and experimental results. The parameters that are temperature dependent include both direct and indirect energy gaps, which subsequently alter the effective mass; and lattice constant that subsequently resulting in the variation of the misfit strain in the SAQDs heterostructures and the band offset in alloyed SAQDs.

The E_p matrix element, Luttinger parameters and spin orbit splitting energy are taken to be temperature independence, which means that the temperature variation of the effective mass arises only through the temperature dependences of the energy gaps. The functional form of the energy gaps temperature dependency is often fitted to the empirical Varshni form [1,40]:

$$E_g(T) = E_g(T=0) - \frac{\alpha T^2}{T+\beta}, \tag{4.43}$$

where α and β are adjustable Varshni's parameters. The energy gap for III-V semiconductors decreases with increasing temperature as α is positive [1].

4.2 SAMPLE GROWTH AND STRUCTURAL CHARACTERISATION

There are two SAQD systems being studied in this thesis, namely InSb/GaSb and $InAs_xSb_{(1-x)}$/InAs. The InSb/GaSb sample was grown at the University of Montpellier 2, while the $InAs_xSb_{1-x}$/InAs samples were grown at the University of Lancaster. A brief discussion regarding the MBE growth of the samples will be given in this section. The SAQD structures have been grown by several epitaxial growth techniques such as MOVPE [41], Liquid Phase Epitaxy (LPE) [42], and MBE [43]. Both InSb/GaSb and InAsSb/InAs SAQDs being studied in this thesis were grown by MBE but by employing two different approaches. The InSb/GaSb sample was grown by University of Montpellier 2 under the DOMINO project FP6-017383, funded by the European Commission under the "Information Society Technologies" Programme of the 6th Framework programme (2002 - 2006). While, the InAsSb/InAs samples were grown in Department of Physics at the University of Lancaster. The overview of MBE growth techniques will be presented first. The details of the individual samples are outlined next.

4.2.1 MOLECULAR BEAM EPITAXY (MBE)

MBE established as the technique for growing thin layers of semiconductor material, specially containing three or four elements in the 1960s. But by the late 1980s, it was challenged by MOVPE as the best growth technique for this purpose [44]. However, it is very attractive for many applications due to it versatility [45]. The MBE system shown in Figure 4.2 and the simpler schematic of the growth chamber is shown in Figure 4.3.

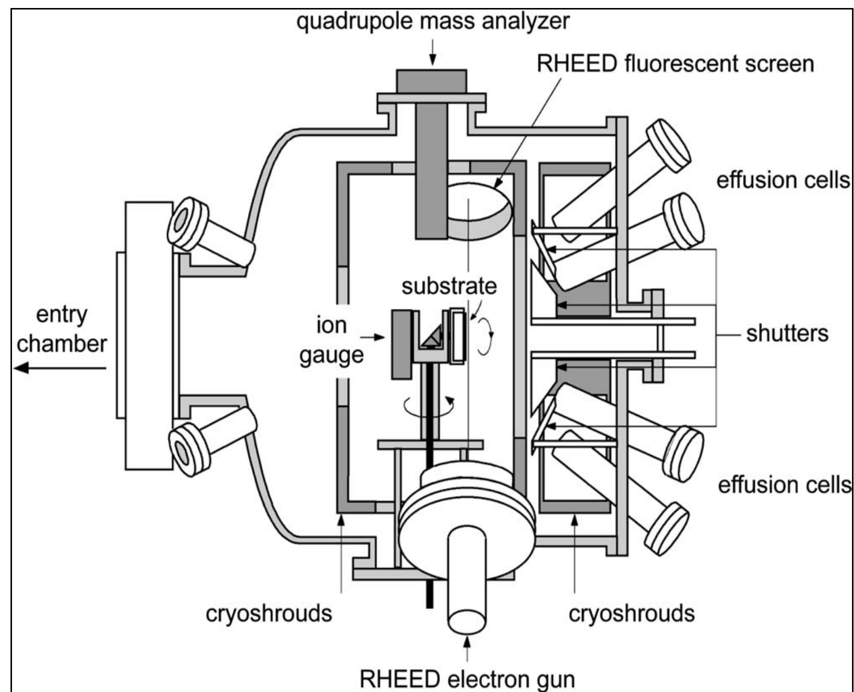

Figure 4.2 : MBE Growth System. Reproduced from Ref. [46].

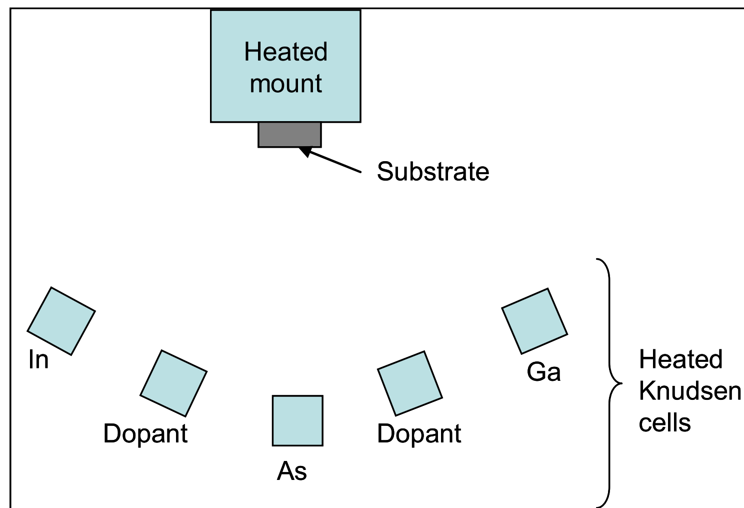

Figure 4.3 : Schematic Of The Growth Chamber. After Ref. [44].

In the growth chamber, the sample is held at a high temperature, which depends on the substrate material and epitaxial layer, in an ultra high vacuum (UHV) at very low background pressure of 10^{-10}-10^{-11} torr while molecular or atomic beams of the constituents impinge upon its surface. The UHV in the growth chamber keeps the background contamination level low and allow in-situ diagnostic techniques such as reflection high energy electron diffraction (RHEED) and Auger technique to be used [45-47]. Therefore, MBE requires a rather sophisticated setup such as clean room facility. Figure 4.4 shows an example of MBE facility.

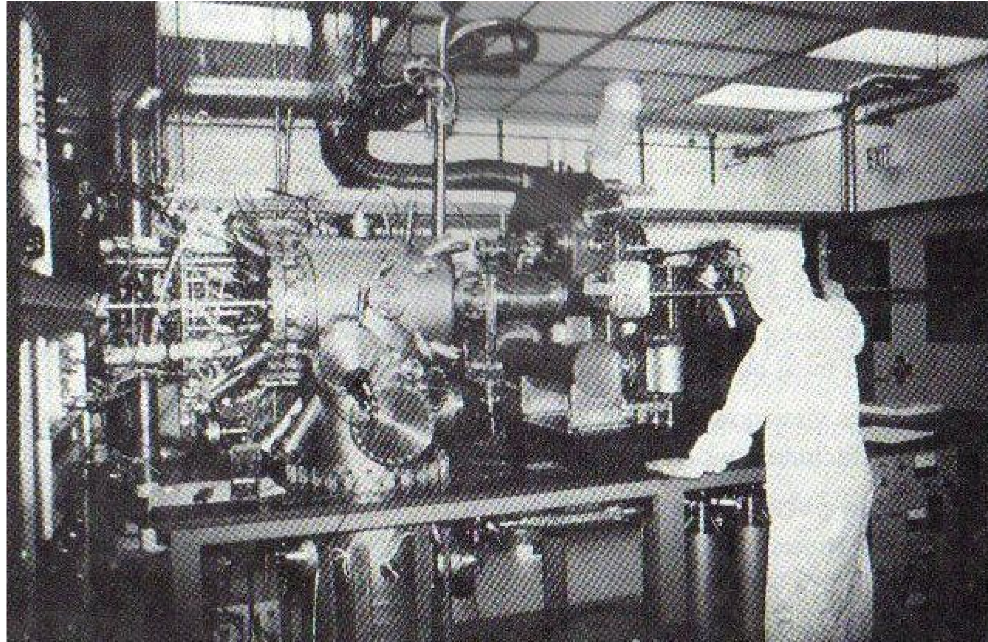

Figure 4.4 : Example of Molecular Beam Epitaxy Facility. Reproduced from Ref. [45].

The heated Knudsen cells (K-cell) provide stable atomic or molecular beams from it crucible which made from pyrolytic Boron Nitride (BN) or graphite, and the rotation of the substrate improve the deposition uniformity. The chemical composition and the doping level of the epilayer can be varied via the temperature of K-cells or the aperture of the shutter that allow rapid changing of beams and abrupt the interfaces and monolayer growth. The low temperature reduces the arrival rate of unwanted species and provides heat dissipation for both the K-cells and the substrate heater [47].

The growth rate of MBE is typically about 1 μm/hour which equal to a monolayer within shutter operating time of less than 1 second. MBE is capable in growing very thin layer at very high quality [44]. A comprehensive review and discussion on the basic features of the MBE growth of SAQDs can be found in Ref. [46]. MBE grown structures are characterised by low levels of unintentional impurities, atomically abrupt interfaces and controlled composition and doping profiles along the growth direction [46].

4.2.2 EPITAXIAL GROWTH MONITORING

Various tools exist to perform in-situ examination of the growth process. Some of these include Quadrupole Mass Analyzers (QMA) to monitor the vacuum environment, RHEED to study the growing surface and X-ray diffraction imaging.

RHEED [46,48] proved to be a powerful technique to analyse the profile of the surface layer during growth. It involves capturing information on the diffraction undergone by electrons impinging on the surface layer. A collimated electron beam generated by an electron gun impinges with a glancing angle onto the surface of the substrate. The electrons are diffracted by the crystal lattice and a diffraction pattern can be observed on the fluorescent screen.

Monitoring the RHEED intensity with time during growth can provide information on the mode of growth as shown in Figure 4.5. The intensities of the individual spots on the RHEED pattern oscillate in a periodic manner as a result of the relative surface coverage of the growing epilayer. Each full oscillation corresponds to a deposited atomic layer, and is dependent on material system, electron energy and incident angle.

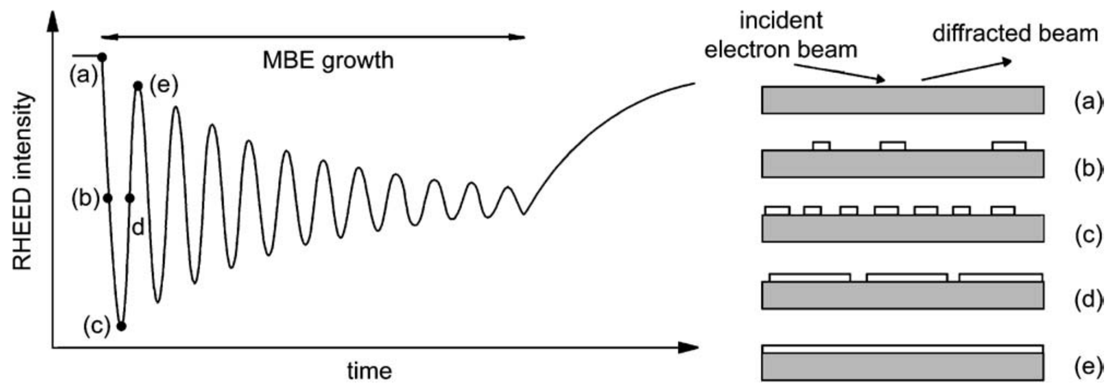

Figure 4.5 : Stages of layer-by-layer growth by nucleation of 2D islands and the corresponding intensity of the zero-order diffracted RHEED beam. Reproduced from Ref. [46].

Figure 4.6 encapsulates quite succinctly the use of RHEED in the growth of InAs/GaAs SAQDs. The initial layer by layer growth of GaAs followed by InAs causes streaks in the RHEED image, with the deposited layer growing with lattice parameter identical to that of the substrate. Beyond a critical thickness (e and f), the streaky pattern

changes and bright spots begin to appear. This indicates the formation of 3-D islands, SAQDs.

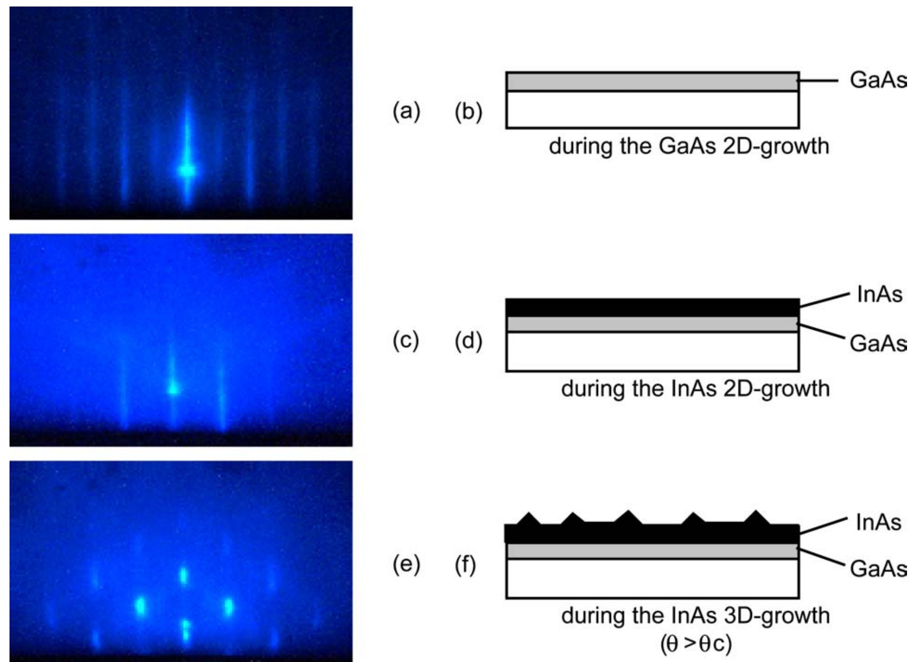

Figure 4.6 : RHEED patterns during deposition of InAs on a GaAs (100) buffer layer. Reproduced from Ref. [46].

4.2.3 InSb/GaSb SAQD SYSTEM SAMPLE GROWTH AND STRUCTURAL CHARACTERISATION

The alternative growth procedure was established in University of Montpellier 2 in order to increase the density of the dots as well as uniform distribution of the dot sizes. Only a brief outline regarding the growth will be given here. More detail discussions can be found in Ref. [49-52].

The samples were grown on GaSb (100) substrate by solid source MBE equipped with As- and Sb-valve cracker cells. Two types of samples have been fabricated in order to perform morphological, structural and optical investigation as shown in Figure 4.7. Uncapped InSb/GaSb dots were grown for direct observation of morphological properties using AFM. For structural and optical studies, the InSb QDs were embedded in a GaSb barrier between two AlGaSb as confining layer.

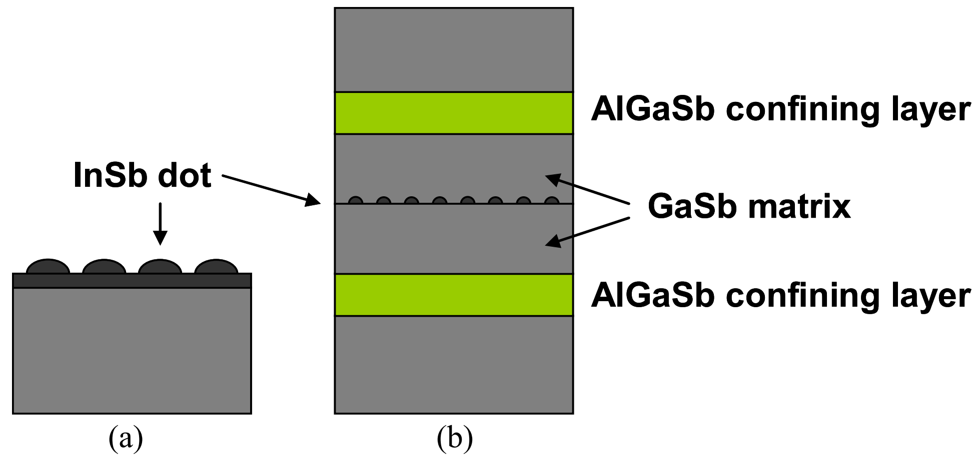

Figure 4.7 : Schematics of InSb/GaSb QDs structure for morphological, structural and optical studies. (a) Uncapped sample for direct morphological study. (b) Capped sample for structural and optical studies.

The growth starts by the *in situ* deoxydation of the GaSb substrate ~550 °C under Sb-flux. The growth temperature is then lowered to ~500 °C to grow a GaSb buffer layer. After completion of the GaSb lower barrier layer, the growth temperature is decreased below 300 °C. The necessary amount of In and Sb are deposited, resulting in a polycrystalline or amorphous film. The growth temperature is then increased and an annealing step is performed at an intermediate temperature of ~400 °C to allow dot formation for ~20-50 s. For uncapped dots, the growth process terminates here. Whereas the growth temperature is then increased to ~500 °C to complete the capping and confining layer for capped sample.

The morphological and structural properties of the InSb/GaSb SAQDs grown from this alternative procedure have been studied by atomic force microscopy (AFM) and transmission electron microscopy (TEM) [49-52]. The AFM investigations were performed by Ioffe Physico-Technical Institute. Figure 4.8 shows the AFM image for the uncapped dot along with the size distribution of the dot. The typical lateral size is ~10-20 nm and the height of the dots is ~1-3 nm. The density of these dots is ~$8x10^{10}$ cm^{-2} and the size distribution is clearly monomodal as shown in Figure 4.8.

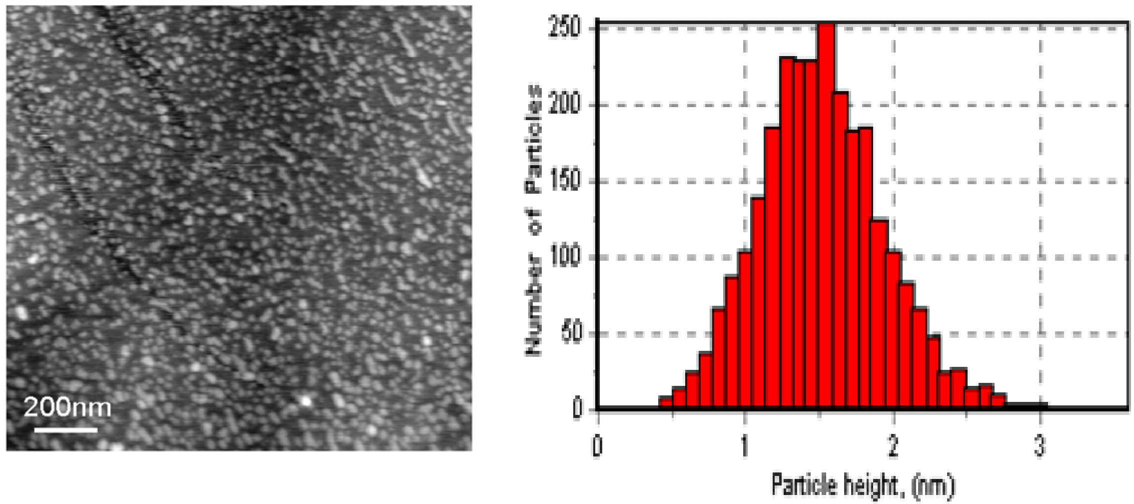

Figure 4.8 : AFM image and the corresponding size distribution of InSb/GaSb SAQD sample grown via alternative two-step procedure.

The structural properties of the capped samples were investigated by using TEM at Paul-Drude-Institute. The bright-field TEM image of sample V384 which containing 3 ML InSb SAQDs is shown in Figure 4.9(a). It shows the existence of a high density small dots and the sample is free of any extended defects.

In order to determine the size and uniformity of the dots, the TEM measurements were performed in a tilted configuration and the resulted bright-field image is shown in Figure 4.9(b). From Figure 4.9(b), the well separated dots are visible by the effect of the strain field on diffracted intensity. The results confirm that the dots are perfectly strained and the average size of the dots is about 10 nm.

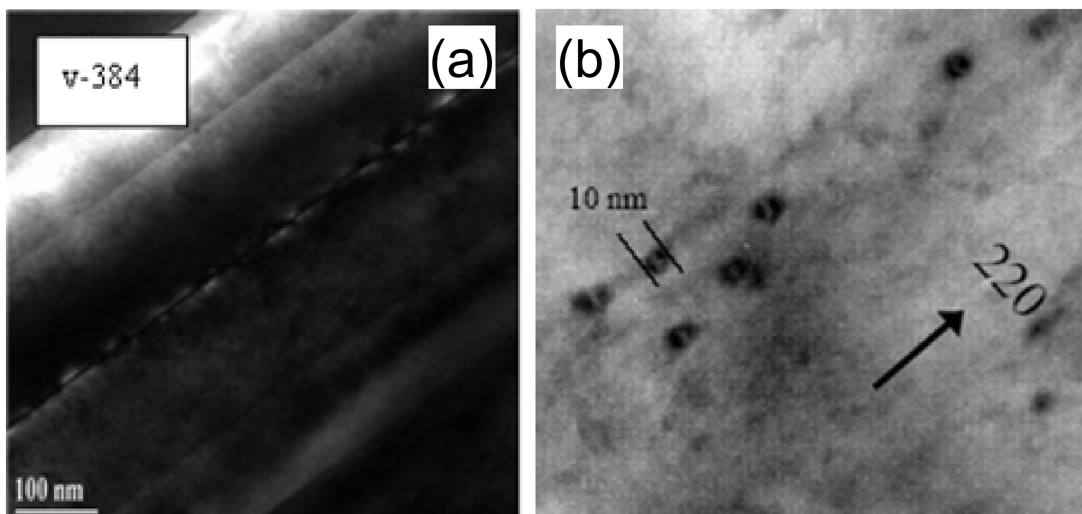

Figure 4.9 : TEM images of buried 3ML InSb QDs (V384). (a) Cross-sectional bright-field. (b) Projectional view of tilted QDs layer to visualise the isolated dots.

Comparison between uncapped and capped nanostructures showed that the buried islands exhibit spherical shape, whereas the uncapped appear as very flat structures. The size of buried dots is also much smaller that the uncapped dots. The uncapped dots are mostly relaxed while buried dots are perfectly strained, even if the same growth conditions are used.

4.2.4 InSb/InAs SAQD SYSTEM SAMPLE GROWTH AND STRUCTURAL CHARACTERISATION

The InSb/InAs SAQDs samples investigated in the thesis were grown on n-InAs (001) substrates using a VG-V80 MBE reactor. Two (Vecco) valved cracker cells were used to provide Sb_2 and As_2 fluxes and a thermal effusion K-cell was used to provide In flux. In situ RHEED was employed to control surface reconstruction. The substrate temperature was measured using an infrared pyrometer calibrated using surface reconstructions under a fixed As flux. The samples contained ten InSb QD layers separated by 8 nm InAs barriers and capped with a 100 nm thick InAs layer as shown in Figure 4.10.

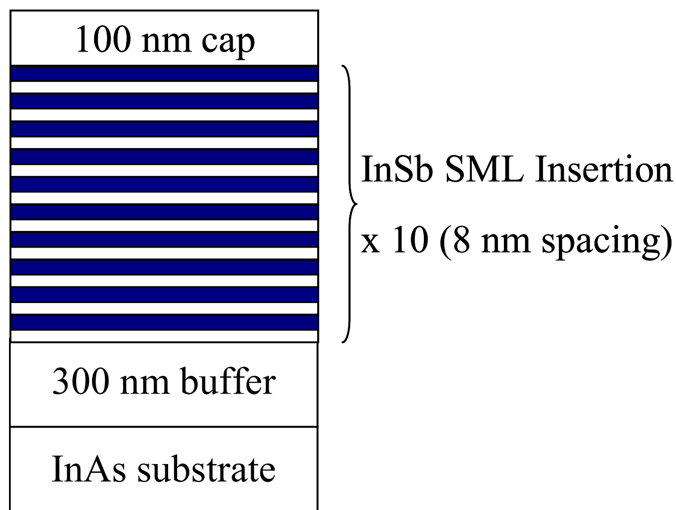

Figure 4.10 : InSb/InAs SML SAQD sample growth

The QDs in the first two samples (A0150 and A0160) were grown by briefly exposing the InAs growth surface to an Sb_2 flux for 20 seconds, exploiting a very efficient Sb-to-As anion exchange reaction [53] as shown in Figure 4.11. A0150 and A0160 were grown at 450 °C and 345 °C respectively. The dots in the third sample, A0224, were grown using Sb/As exchange at 430 °C, followed by additional migrant

enhanced epitaxy (MEE) deposition of 0.7 ML of InSb [54]. This enables growth of larger dots at high growth temperatures which are required for efficient MIR devices.

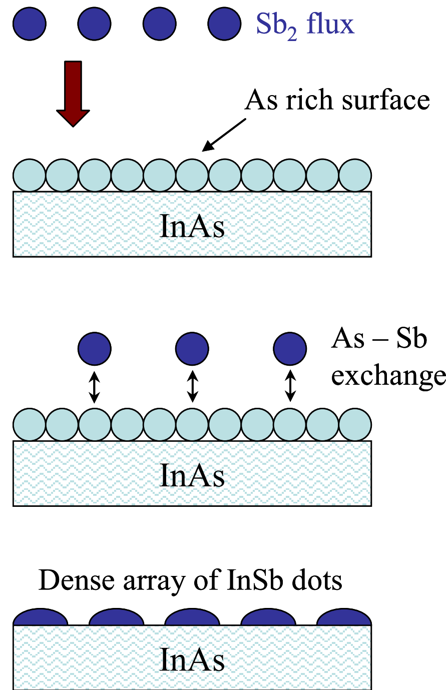

Figure 4.11 : InSb SML SAQD growth mechanism

TEM studies revealed the presence of a dense array (~10^{12} cm^{-2}) of very small (~2.5 nm) nanometer-sized InSb islands within the InSb insertion [54]. The lateral size distribution and density of the islands were found to be practically the same to the structures grown by using Sb_4 and As_4 fluxes as in Ref. [55].

4.3 EXPERIMENTAL STUDY

One of the aims of the project was to study the optical properties of the SAQD samples using experimental techniques. The experimental work on the project focuses on studying the optical properties of the SAQDs by means of PL spectroscopy.

4.3.1 PHOTOLUMINESCENCE MEASUREMENT

PL is a luminescence technique use for investigating both intrinsic electronic transitions and electronic transitions at impurities and defects in semiconductors and insulators [46,47]. It is a noncontact, nondestructive technique that requires no sample preparation.

PL is the optical radiation emitted by a semiconducting crystal after excitation with incident light source (usually a laser). Most of the light results from the difference in energy of the excited electron (in the conduction energy band) returning to its ground state (valence energy band). The PL spectra have narrow bands (peaks) which make analysis possible. The PL is a complementary technique to the absorption spectra. The positions of the PL peaks are related to the energy of each excited level and can be used as a sensitive probe to find impurities and other defects in semiconductors.

The spectrum of the photoluminescence (*PL spectrum*) and also the dependence of its intensity on the irradiation intensity and device temperature can deliver important information for device characterization. In particular, PL spectra and their intensity dependencies can allow one

- to determine the bandgap energy and/or the wavelength of maximum gain
- to determine the composition of ternary or quaternary layers
- to determine impurity levels
- to investigate recombination mechanisms

The PL measurements were performed by using a Fourier Transform Infrared (FTIR) spectroscopy. FT-IR is a fast analytical technique and provides very interesting qualitative and quantitative information [56] which acquire broadband near IR to far IR spectrum [57]. Instead of viewing each component frequency sequentially, as in a dispersive IR spectrometer, an FT-IR spectrometer collects and examines all wavelengths simultaneously, known as multiplex or Felgett advantage [57]. FT-IR is a method of obtaining infrared spectra by first collecting an interferogram of a sample signal by using an interferometer and involves a mathematical manipulation of Fourier Transform on the interferogram to obtain the spectrum which may also involves phase correction and apodization [57,58].

In an FT-IR system, there are three basic spectrometer components: radiation source, interferometer, and detector. A simplified optical layout of a typical FT-IR spectrometer is illustrated in Figure 4.12. The layout shown is suitable for absorption, transmission and reflectance measurements.

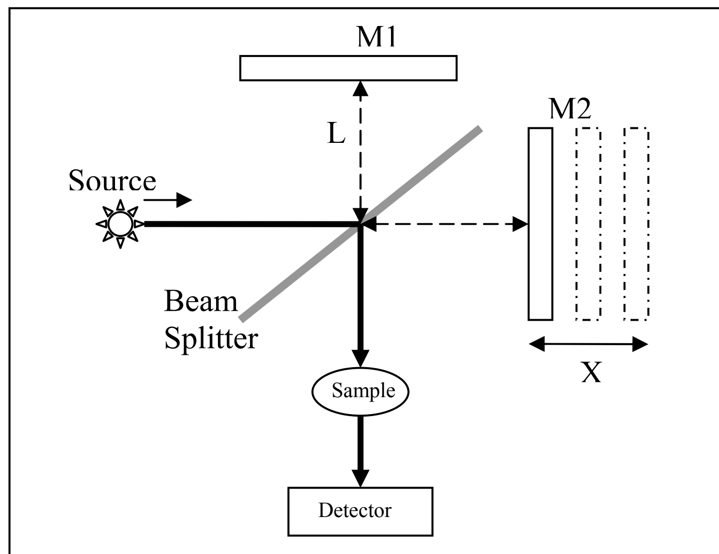

Figure 4.12 : A simplified optical layout of a typical FT-IR Spectrometer for absorption, transmission and reflectance measurements. After Ref. [57-60].

In order to use FT-IR spectrometer to perform the PL measurement, the setup has to be modified to the one shown in Figure 4.13 below. From the diagram one can see the movement of the beam from the sample through the beam splitter, then through the filter in A172 external compartment and finally being detected by the detector. A piece of semi-insulating GaAs substrate was used to filter out any emission below 1 μm.

The following pieces of equipment were used to obtain the measurements:

i. Bruker IFS 66/S with A172 external compartment
ii. PC with OPUS software
iii. KBr beam splitter
iv. Liquid nitrogen cooled InSb detector
v. EG & G Instruments 7265 DSP Lock-In Amplifier
vi. Oxford Instruments OptistatDN Cryostat
vii. Edwards Vacuum pumping system
viii. Oxford Intelligent ITC temperature controller

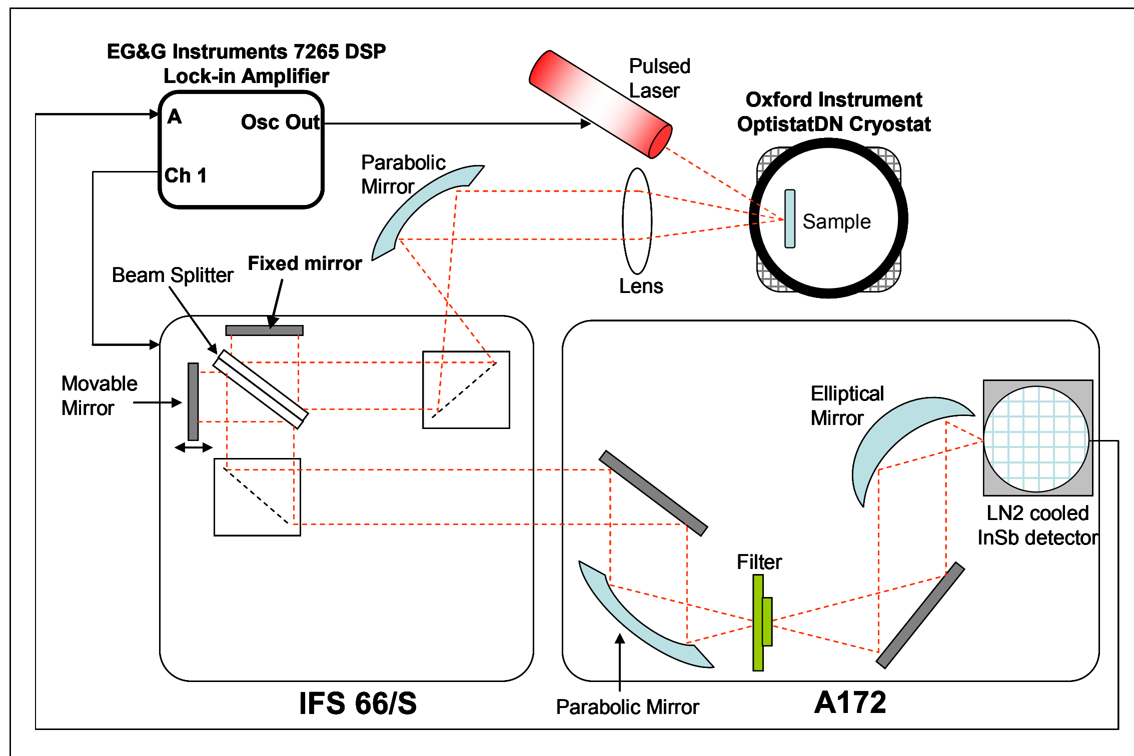

Figure 4.13 : FT-IR PL measurement set-up

4.3.2 PRINCIPLE of OPERATION of FT-IR PL MEASUREMENT

As radiation emitted from the sample as a result of the excitation by a source, it is collimated and directed to the beam splitter, and strikes the beam splitter. At the beam splitter, the beam separates into two. One beam is reflected off the beam splitter, travels to the fixed mirror, and the other beam travels to the moving mirror. Both beams are reflected back to the beam splitter. The reflected beam travels through a distance L and is reflected back to hit the beam splitter again after a total path length of 2L. Although same thing happen to the transmitted beam but the total path length of the transmitted beam is according to $2*(L = x)$ because moving mirror is not fixed at the same position L but moving back and forth around L by a distance x [57,58,61].

After reflection by both mirrors, the two halves of the beam recombine on the beam splitter and exhibit optical path different of $2*x$. This means the partial beams are spatially coherent and create an interference pattern when they recombine since some of the wavelengths recombine constructively and some destructively [58,59].

The interference signal acquired is called an interferogram. Interferogram is actually a time domain spectrum and records the detector response changes versus time

within the mirror scan. Figure 4.14 shows a typical interferogram collected by FT-IR spectrometer.

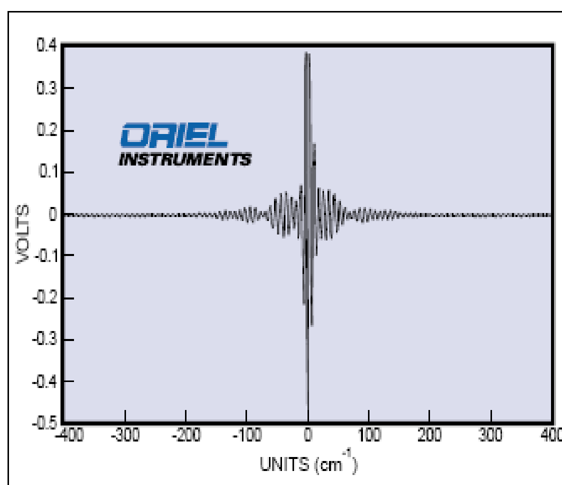

Figure 4.14: A typical interferogram collected by FT-IR spectrometer. Reproduced from Ref. [57].

Once an interferogram is collected, a mathematical operation known as Fourier Transform is performed to convert the interferogram into a final IR spectrum which is the familiar frequency domain spectrum showing intensity versus frequency, i.e. emission, absorption, transmission, etc. This also explains how the term *Fourier Transform Infrared* spectrometry is created.

The x-axis of the FT-IR spectrum is typically represented the wave numbers in cm^{-1}. This unit is a product of the Fourier transform algorithm operating on the interferogram and is the reciprocal of the actual wavelength of light measured in centimetres at a point in the infrared spectrum [59].

4.3.3 FT-IR PL MEASUREMENT PROCEDURES

There are a few procedures that have to be followed in order to obtain a spectrum. First of all, the samples were mounted on a holder which was screwed onto a sample rod. This was then lowered into the Oxford Instruments cryostat and all locked into place using the instrument clamps. The cryostat was capable of liquid nitrogen LN_2 cooling, a facility that was employed with most measurements. To do this, the cryostat was evacuated first using a conventional rotary pump, followed by a high performance turbo pump, until pressures in the cryostat reached high vacuum conditions (in the 10^{-6} Torr range).

The cryostat heat exchanger was filled with gaseous helium and then a funnel used to introduce about two litres of liquid nitrogen into the cryostat's LN_2 storage chamber. The desired sample temperature was digitally selected using the ITC temperature controller. The temperature control is either lowering temperature by introducing LN_2 into the heat exchanger surrounding the sample or raised using a heater built into the cryostat, all of which is electronically managed by the temperature controller. Liquid nitrogen was then poured down a funnel into the InSb detector jacket to cool it down to operating temperature (77K).

The FTIR was then initialised and desired hardware parameters set using the OPUS PC application. OPUS was then used to initiate the FTIR scan and format the output data as required.

Once the samples had cooled down to liquid nitrogen temperature, the power dependent PL can be performed. The excitation power was varied from 10mW up to 90mW at 10mW interval. Then the temperature dependent PL was performed from 77K up to 300K and the temperatures were controlled by Oxford Intelligent ITC temperature controller. The excitation power was kept at 20mW.

4.3.4 ADVANTAGES of FT-IR PL SPECTROSCOPY

FT-IR instruments have distinct advantages over conventional dispersive spectrometer [57,58,60,62]:

- FT-IR spectrometers have a built-in wave number calibration of high precision that practically about 0.01 cm^{-1} due to the use of a helium neon laser as the internal reference. This is known as the Connes advantage. This eliminates the need for external calibrations.
- FT-IR spectrometers have better speed and sensitivity known as Multiplex or Felgett advantage. A complete spectrum can be obtained during a single scan of the moving mirror, while the detector observes all frequencies simultaneously. In IR region, an FTIR instrument can achieve the same signal-to-noise (S/N) ratio of a dispersive spectrometer in a fraction of the time $\leqslant$1 sec versus 10 to 15 min. The S/N ratio is proportional to the square root of the total number of measurements.

- Increased optical throughput which known as Jaquinot advantage because FT-IR instruments do not require slits because dispersion or filtering is not needed. Instead, a circular optical aperture is commonly used in FTIR systems. The beam area of an FT instrument is usually 75 to 100 times larger than the slit width of a dispersive spectrometer. Thus, more radiation energy is made available. This constitutes a major advantage for many samples or sampling techniques that are energy-limited.
- Elimination of stray light and emission contributions. The interferometer in FTIR modulates all the frequencies. The unmodulated stray light and sample emissions (if any) are not detected.
- Modern FTIR spectrometers are usually equipped with a powerful, computerized data system. It can perform a wide variety of data processing tasks such as Fourier transformation, interactive spectral subtraction, baseline correction, smoothing, integration, and library searching.

FTIR spectrometers are the preferred choice for samples that are energy-limited or when increased sensitivity is desired although the spectrum of many samples can be satisfactorily run on either FTIR or dispersive instruments. A wide range of sampling accessories is available to take advantage of the capabilities of FTIR instruments.

References:

[1] I. Vurgaftman, L. R. Ram-Mohan, and J. R. Meyer, J. Appl. Phys. **89**, 5815 (2001).

[2] S. I. Rybchenko, G. Yeap, R. Gupta, I. E. Itskevich, and S. K. Haywood, J. Appl. Phys. **102**, 013706 (2007).

[3] J. D. Eshelby, in *Adv. Solid State Phys.*, edited by F. Seitz and D. Turnbull (Academic, New York, 1956), Vol. 3, p. 79; Proc. R. Soc. London Ser. A **241**, 376 (1957).

[4] H. Jiang and J. Singh, Phys. Rev. B. **56**, 4696 (1997); IEEE J. Quant. Electron. **34**, 1188 (1998).

[5] A. J. Williamson, L. W. Wang, and A. Zunger, Phys. Rev. B **62**, 12963 (2000); L. W. Wang and A. Zunger, *ibid.* **59**, 15806 (1999); L. W. Wang, J. Kim, and A. Zunger, *ibid.* **59**, 5678 (1999).

[6] S. Lee, F. Oyafuso, P. von Allmen, and G. Klimeck, Phys. Rev. B **69**, 045316 (2004); S. Lee, O. L. Lazarenkova, P. von Allmen, F. Oyafuso, and G. Klimeck, *ibid.* **70**, 125307 (2004).

[7] M. A. Cusack, P. R. Briddon, and M. Jaros, Phys. Rev. B **54**, R2300 (1996).

[8] C. Pryor, Phys. Rev. B **57**, 7190 (1998).

[9] M. Grundmann, O. Stier, and D. Bimberg, Phys. Rev. B **52**, 11969 (1995).

[10] G. R. Liu and Q. Jerry, Semicond. Sci. Technol. **17**, 630 (2002).

[11] W. Lee, J. -M. Myong, Y. -H. Yoo, and H. Shin, Solid State Commun. **132**, 135 (2004).

[12] G. Muralidharan, Japan. J. Appl. Phys. **39**, L658 (2000).

[13] M. Tadic, F. M. Peeters, K. L. Janssens, M. Korkusinski, and P. Hawrylak, J. Appl. Phys. **92**, 5819 (2002).

[14] M. K. Kuo, T. R. Lin, B. T. Liao, and C. H. Yu, Physica E **26**, 199 (2005).

[15] R. V. N. Melnik and K. N. Zotsento, Modelling Simul. Mater. Sci. Eng. **12**, 465 (2004).

[16] A. Carlsson, L. R. Wallenberg, C. Persson, and W. Seifert, Surf. Sci. **406**, 48 (1998).

[17] T. Benabbas, P. Francois, Y. Androussi, and A. Lefebvre, J. Appl. Phys. **80**, 2763 (1996).

[18] Q. X. Pei, C. Lu, and Y. Y. Wang, J. Appl. Phys. **93**, 1487 (2003).

[19] I. P. Ipatova, V. G. Malyshkin, and V. A. Shchukin, V.A., J. Appl. Phys. **74**, 7198 (1993).

[20] M. Tadić, F. M. Peeters, and K. L. Janssens, Phys. Rev. B **65**, 165333 (2002).

[21] L. D. Landau and I. M. Lifshitz, *Theory of Elasticity* (London, Pergamon, 1959), v. 17.

[22] J. O. Fossum, J. Phys. C: Solid State Phys. **18**, 5531-5548 (1985).

[23] C. Pryor, J. Kim, L. W. Wang, a. J. Williamson, and A. Zunger, J. Appl. Phys. **83**, 2548 (1998).

[24] G. R. Liu and S. S. Quek Jerry, Semicond. Sci Technol. **17**, 630 (2002).

[25] V. Siklitsky and A. Tolmatchev, 2001. New Semiconductor Materials. Characteristics and Properties: Physical Properties of Semiconductors [Online]. St. Peterburg: Ioffe Institute. Available: http://www.ioffe.ru/SVA/NSM/Semicond

[26] J. F. Nye, *Physical Properties of Crystals,* (Oxford, Oxford University Press, 1960).

[27] R. W. Keyes, J. Appl. Phys. **33**, 3371 (1962).

[28] C. G. Van de Walle, Phys. Rev. B **39**, 1871 (1989).

[29] S. -H. Wei and A. Zunger, Phys. Rev. B **49**, 14337(1994).

[30] G. E. Pikus and G.L. Bir, Sov. Phys. Solid State **1**, 136 (1959); *ibid* **1**, 1502 (1959); *ibid* **3**, 730 (1961).

[31] F. H. Pollak and M. Cardona, Phys. Rev. **172**, 816 (1968).

[32] W. C. Herring and E. Vogt, Phys. Rev. **101**, 944 (1956).

[33] T. B. Bahder, Phys. Rev. B **45**, 1629 (1992); Phys. Rev. B **41**, 11992 (1990).

[34] J. Los, A. Fasolino, and A. Catellani, Phys. Rev. B **53**, 4630(1996).

[35] B. A. Foreman, Phys. Rev. B **56**, R12748(1997).

[36] F. Boxberg and J. Tulkki, Rep. Prog. Phys. **70**, 1425(2007).

[37] C. Pryor, M. –E. Pistol, and L. Samuelson, Phys. Rev. B **56**, 10404 (1997).

[38] S. L. Chuang, Physics of Optoelectronic Devices (Wiley, New York, 1995).

[39] S-. H. Park, D. Ahn, and Y-. T. Lee, J. Appl. Phys. 96, 2055 (2004).

[40] Y. P. Varshni, Physica **34**, 149 (1967).

[41] E. Alphandéry, R. J. Nicholas, N. J. Mason, B. Zhang, P. Möck, and G. R. Booker, Appl. Phys. Lett. **74**, 2041 (1999); P. Möck, G. R. Booker, N. J. Mason, R. J. Nicholas, E. Alphandéry, T. Topuria, and N. D. Browning, Mat. Sci. Eng. **B80**, 112 (2001), Y. Qiu, D. Uhl, and S. Keo, Appl. Phys. Lett. **84**, 263 (2003); Y. Qiu and D. Uhl, Appl. Phys. Lett. **84**, 1510 (2004); P. A. Shields, C. W. Bumby, L. J. Li, and R. J. Nicholas, J. Appl. Phys. **96**, 2725 (2004)

[42] K. M. Gambaryan, V. M. Aroutiounian, T. Boeck, M. Schulze, and P. Soukiassian, J. Phys. D: Appl. Phys. **41**, 162004 (2008); K. D. Moiseev, Ya. A. Parkhomenko, A. V. Ankudinov, E. V. Gushchina, M. P. Mikhaĭlova, A. N. Titkov, and Yu. P. Yakovlev, Tech. Phys. Lett. **33**, 295 (2007); A. Krier and X. L. Huang, Physica E

15, 159 (2002), A. Krier, X. L. Huang, and A. Hammiche, J. Phys. D: Appl. Phys. **34**, 874 (2001); A. Krier, X. L. Huang, and A. Hammiche, Appl. Phys. Lett. **77**, 3791 (2000); A. Krier, Z. Labadi, and A. Hammiche, J. Phys. D: Appl. Phys. **32**, 2587 (1999)

[43] N. Deguffroy, V. Tasco, A. N. Baranov, E. Tournié, B. Satpati, A. Trampert, M. S. Dunaevskii, A. Titkov, and M. Ramonda, J. Appl. Phys. **101**, 124309 (2007); V. Tasco, N. Deguffroy, A. N. Baranov, E. Tournié, B. Satpati, A. Trampert, M. S. Dunaevskii, and A. Titkov, Appl. Phys. Lett. **89**, 263118 (2006); V. Tasco, N. Deguffroy, A. N. Baranov, E. Tournié, B. Satpati, A. Trampert, M. S. Dunaevskii, and A. Tiykov, J. Cryst. Growth **301-302**, 713 (2007); N. Deguffroy, V. Tasco, A. N. Baranov, B. Satpati, A. Trampert, M. S. Dunaevskii, A. Titkov, F. Genty, and E. Tournié, Phys. Stat. Sol. (c) **4**, 1743 (2007); V. Tasco, N. Deguffroy, A. N. Baranov, E. Tournié, B. Satpati, and A. Trampert, Phys. Stat. Sol. (b) **243**, 3959 (2006); J. C. Ferrer, F. Peiró, A. Cornet, J. R. Morante, T. Uztmeier, G. Armelles, and F. Briones, Appl. Phys. Lett. **69**, 3887 (1996); A. N. Semenov, V. A. Solov'ev, B. Ya. Meltser, O. G. Lyublinskaya, Ya. V. Terent'ev, A. A. Sitnikoya, and S. V. Ivanov, Acta Physica Polonica A **108**, 859 (2005); A. F. Tsatsul'nikov, S. V. Ivanov, P. S. Kopev, A. K. Kryganovskii, N. N. Ledentsov, M. V. Maximov, B. Ya. Mel'tser, P. V. Nekludov, A. A. Suvorova, A. N. Titkov, B. V. Volovik, M. Grundmann, D. Bimberg, and Zh. I. Alferov, J. Elec. Mat. **27**, 414 (1998); N. Bertru, O. Brandt, M. Wassermeier, and K. Ploog, Appl. Phys. Lett. **68**, 31 (1996); A. F. Tsatsul'nikov, N. N. Ledentsov, M.V. Maksimov, B. Ya. Mel'tser, S. V. Shaposhnikov, B. V. Volovik, I. L. Krestnikov, A. V. Sakharov, N. A. Bert, P. S. Kopev, Zh. I. Alferov, and D. Bimberg, Semiconductors **31**, 55 (1997); F. Hatami, S. M. Kim, H. B. Yuen, J. S. Harris, Appl. Phys. Lett. **89**, 133115 (2006)

[44] D. Wood, *Optoelectronic Semiconductor Devices*. (New York: Prentice-Hall, 1994).

[45] B. G. Streetman and S. Banerjee, *Solid State Electronic Devices*, 5th Edition. (New Jersey: Prentice Hall International, Inc., 2000).

[46] S. Franchi, G. Trevisi, L. Seravalli, and P. Frigeri, Progress Cryst. Growth Charact. Mater. **47**, 166 (2003).

[47] R. A. Strading and P. C. Klipstein, ed., *Growth and Characterisation of Semiconductors*. (Bristol: J W Arrowsmith Ltd., 1990).

[48] A. Feltrin and A. Freundlich, J. Cryst. Growth **301-302**, 38 (2007).

[49] V. Tasco, N. Deguffroy, A. N. Baranov, E. Tournié, B. Satpati, A. Trampert, M. S. Dunaevskii, and A. Titkov, Appl. Phys. Lett. **89**, 263118 (2006).

[50] V. Tasco, N. Deguffroy, A. N. Baranov, E. Tournié, B. Satpati, and A. Trampert, Phys. Stat. Sol. (b) **243**, 3959 (2006).

[51] N. Deguffroy, V. Tasco, A. N. Baranov, B. Satpati, A. Trampert, M. Dunaevskii, A. Titkov, F. Genty, and E. Tournié, Phys. Stat. Sol. (c) **4**, 1743 (2007).

[52] N. Deguffroy, V. Tasco, A. N. Baranov, E. Tournié, B. Satpati, A. Trampert, M. Dunaevskii, A. Titkov, and M. Ramonda, J. Appl. Phys. **101**, 124309 (2007).

[53] S. V. Ivanov, A. N. Semenov, V. A. Solov'ev, O. G. Lyublinskaya, Ya. V. Terent'ev, B. Ya. Meltser, L. G. Prokopova, A. A. Sitnikova, A. A. Usikova, A. A. Toropov, and P. S. Kop'ev, J. Cryst. Growth **278**, 72 (2005).

[54] P.J. Carrington, V. A. Solov'ev, Q. D. Zhuang, A. Krier, and V. Ivanov, Appl. Phys. Lett. **93**, 091101 (2008).

[55] O. G. Lyublinskaya, V. A. Solov'ev, A. N. Semenov, B. Ya. Meltser, Ya. V. Terent'ev, L. A. Prokopova, A. A. Toropov, A. A. Sitnikova, O. V. Rykhova, and S. V. Ivanov, J. Appl. Phys. **99**, 093517 (2006).

[56] M. Khanmohammadi and K. Kargosha, Talanta **65**, 824 (2005).

[57] Oriel Instruments, *Introduction to FT-IR Spectroscopy*. Product catalogue (No Date).

[58] W. Herres and J. Gronholz, *Understanding FT-IR Data Processing* (Karlsruhe: Bruker Analytische Meβtechnik GmbH, 1987).

[59] Thermo Nicolet, *Theory of Infrared Spectroscopy Instrumentation*. (Madison: Thermo Electon, 2002).

[60] C. P. Sherman Hsu, Infrared Spectroscopy. In: F. Settle, ed. *Handbook of Instrumental Techniques for Analytical Chemistry* (New Jersey: Prentice-Hall, 1997). pp. 247-283.

[61] P. Kosters, *FT-IR Spectroscopy of Thin Biological Layers*. PhD diss. (University of Twente, 2000).

[62] B. C. Smith, *Fundamentals of Fourier Transform Infrared Spectroscopy* (Boca Raton, Florida: CRC Press, Inc, 1996).

CHAPTER 5

PRELIMINARY STUDY OF STRAIN DISTRIBUTION AND STRAIN-MODIFIED BAND PROFILE IN SAQDs

5.0 INTRODUCTION

In this chapter, the model validation studies are performed. It is an important procedure to undertake prior to performing the actual modelling. It helps in determining the best model to be used and to prevent unnecessary mistakes when performing the modelling. As mentioned earlier, many previous studies simplify the problem geometry into axial symmetric geometry e.g. conical and lens shape due to the computational demands of a full 3-D model. Therefore, the FEM study for a 2-D axial symmetric model will first be considered to verify this approach and to simulate the loading and boundary conditions for various structures that will be outlined later. Following this, the same structures are modelled using a full 3-D model in order to compare the results obtained from these two models. Although the 3-D model is computationally extensive and expensive a complete picture of the strain distribution of the structure can be obtained. Studies can also be performed easily on various planes of the structure.

After verifying the results published in the literature for the InAs/GaAs system, the preliminary study of strain distribution and strain-modified band profile is performed for the InSb/GaSb SAQD system. This preliminary study has purposes; to justify the FEM modelling method and to justify the reliability of the results obtained using the Comsol Multiphysics package.

In the literature, the strain-modified band profile is normally plotted as a 1-D profile along the growth directed at the centre of the dot. It will be revealed that the 1-D profile is not adequate in providing an overall picture of the band profile. In this thesis, the band profiles will be plotted as a 2-D colour plot along the (100)- and (110)-plane. The purpose is to show the variation of the band profile across the whole SAQD structures as a result of the misfit strain.

5.1 STRAIN FIELD CALCULATIONS

Following Equation 4.18, the lattice mismatch for the InSb/GaSb system is -6.29%. By the definition in Equation 4.19, the lattice mismatch for the InSb/GaSb system is -5.92%. In the first attempt to calculate the strain distribution in the QD system, the former definition was used. This is the definition most often used in the literature. The latter definition is employed when comparison between isotropic and anisotropic models in terms of strain field and band edge calculations is performed using Comsol Multiphysics. This also applies to the other models described in this thesis.

The lattice mismatch can be regarded as a kind of eigenstrain that is commonly used in the mechanics of composite materials to simulate the thermal expansion, phase deformation or to describe the initial strain in the QD systems.

5.1.1 LITERATURE RESULS

In order to verify the approach to simulate the loading and boundary conditions, the published results by *Benabbas et al.* [1] have been reproduced and analysed. The system studied is the InAs/GaAs QD system. The FEM calculations were performed using both the FEM packages ANSYS and Comsol Multiphysics employing 2-D axial symmetry about the cone axis to represent the 3-D model. The calculations have been carried out for three types of island, one conical island and two truncated conical islands with e/e'=2 and e/e'=3, respectively with height, h=3 nm, island half width, e=12nm and substrate half width, *l*=30 nm, as shown in Figure 5.1 below.

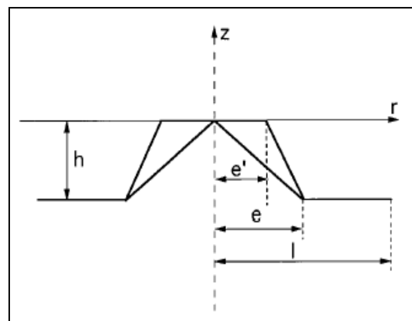

Figure 5.1 : Schematic View of Model Studied with h=3nm, l=30nm. Reproduced from Ref. [1].

The lattice mismatch between InAs island and GaAs substrate is -0.067. Isotropic behaviour of the materials was assumed. The bottom surface of the substrate is

fixed against displacement in all directions. The periodicity of the structure was chosen to be 60 nm and it was taken into account by applying appropriate boundary condition in which the right hand side of the substrate is fixed against displacement in the radial direction. The material parameters are taken from Ref. [2,3] as listed in Table 4.2.

Although the modelling results can not be compared directly to the results from Ref. [1]; nevertheless, the results obtained from both ANSYS and Comsol Multiphysics packages show very good qualitative agreement with the published results as shown in Figure 5.2 below.

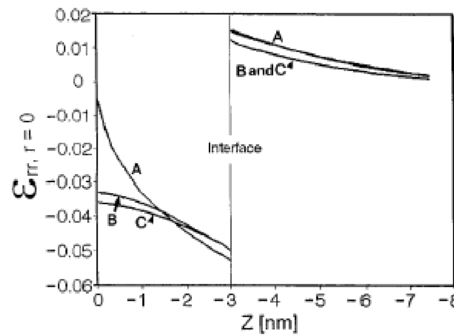

(a) The Result from Benabbas et al. Reproduced from Ref. [1].

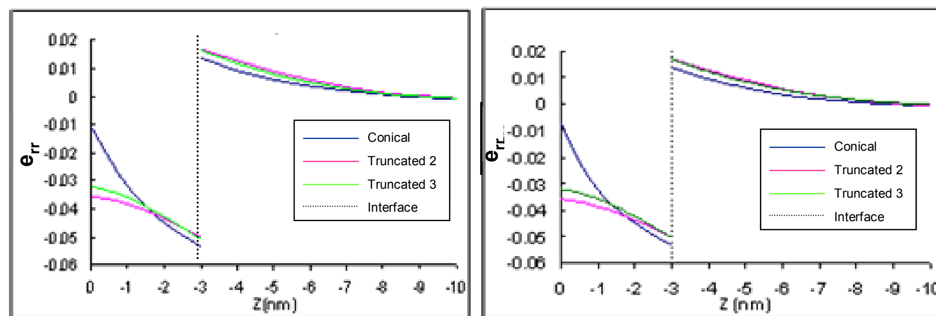

(A=Conical; B=Truncated e/e'=3; C=Truncated e/e'=2)

(b) ANSYS Results *(c) Comsol Multiphysics Results*

Figure 5.2 : Literature FEM calculation results (a) results from Ref. [1] (b) ANSYS modelling and (c) Comsol Multiphysics modelling

5.1.2 2-D AXIAL SYMMETRY MODEL for InSb/GaSb SAQD SYSTEM

As mentioned earlier, Comsol Multiphysics will be the FEM package that will be used to perform the modelling in this thesis. After being able to reproduce the results from Ref. [1], further investigation into the reliability of the results obtained from Comsol Multiphysics was carried out. This was done by performing strain field modelling for the InSb/GaSb SAQD system using both packages and employing the 2-D axial symmetry model. Again, isotropic behaviour of the materials was assumed and the material parameters are listed in Table 4.2.

5.1.2.1 ANSYS MODEL

The calculations were carried out by using ANSYS in the first place. The same loading and boundaries conditions as in Ref. [1] were used. The geometry is meshed with 8-node rectangular elements in the matrix and wetting layer while the dot is meshed by using 6-node triangular elements. The bottom line of the substrate is fixed against displacement in all directions while the side surface of the substrate is fixed against displacement in the radial direction.

The contour plots of the e_{xx} component of the strain distribution for a truncated conical QD are shown in the Figure 5.3 below and for a conical QD are shown in Figure 5.4.

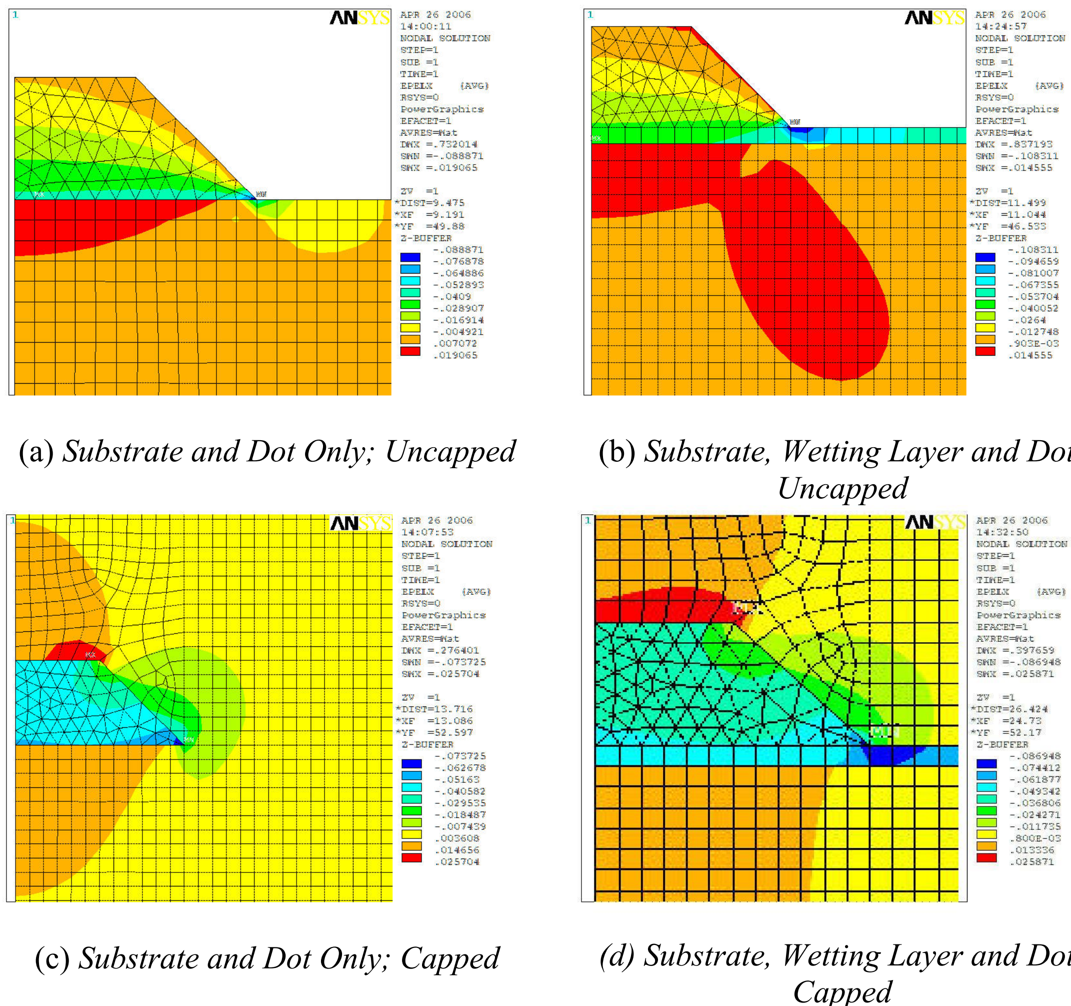

(a) *Substrate and Dot Only; Uncapped*

(b) *Substrate, Wetting Layer and Dot; Uncapped*

(c) *Substrate and Dot Only; Capped*

(d) Substrate, Wetting Layer and Dot; Capped

Figure 5.3 : Contour Plot of e_{xx} Component for InSb/GaSb Truncated Conical QDs Structure

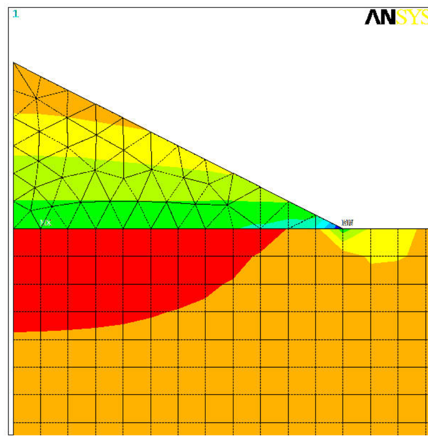

(a) *Substrate and Dot Only; Uncapped*

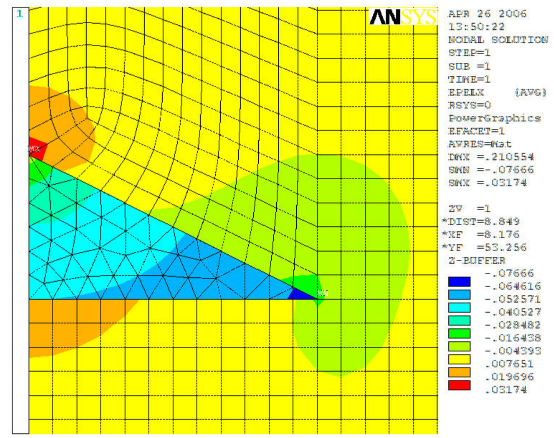

(c) *Substrate and Dot Only; Capped*

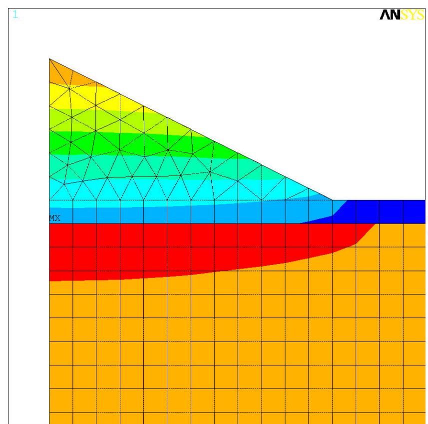

(b) *Substrate, Wetting Layer and Dot; Uncapped*

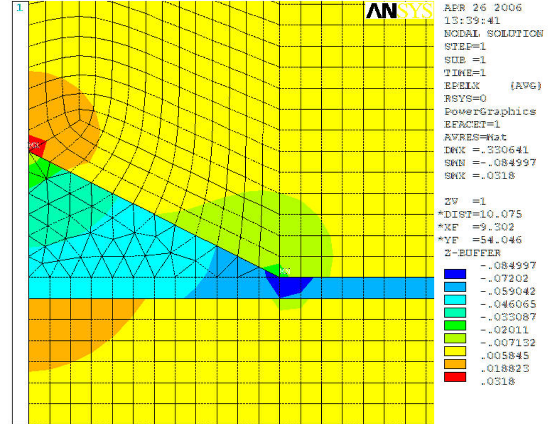

(d) *Substrate, Wetting Layer and Dot; Capped*

Figure 5.4 : Contour Plot e_{xx} Component for InSb/GaSb Conical QDs Structure

From the contour plots, strain relaxation is observed in the island whereas strain concentration occurs at its edge. By symmetry, the strain component $e_{xx} = e_{yy}$. The minimum in the e_{xx} component of strain is in the apex region of the conical QD whilst it is away from the centre of the truncated conical QD at the edge between the plateau and the slope. This results in a less rapid change in the strain gradient along the axial region of the truncated conical QD as compared to the conical QD. The magnitude of the strain at an arbitrary location in the dot is different for the two cases and a significant tensile strain is also observed in the underlying substrate.

The strain concentration is taken over by the wetting layer for the structures that contain a wetting layer; however, the overall strain distribution is not affected by the existence of wetting layer as we shall see later. For the capped QD structures, a decrease

in the peak occurring above the centre of the island is observed and this is due to the relaxation of the tensile stress as the stress is being absorbed by the capping layer.

Figure 5.5 below shows the strain field component for InSb/GaSb conical QD, while Figure 5.6 shows the strain field component for InSb/GaSb truncated conical QD and Figure 5.7 shows the comparison of strain field distribution between conical and truncated conical QDs. All these plots are plotted along the [001] direction through the centre of the QD structures.

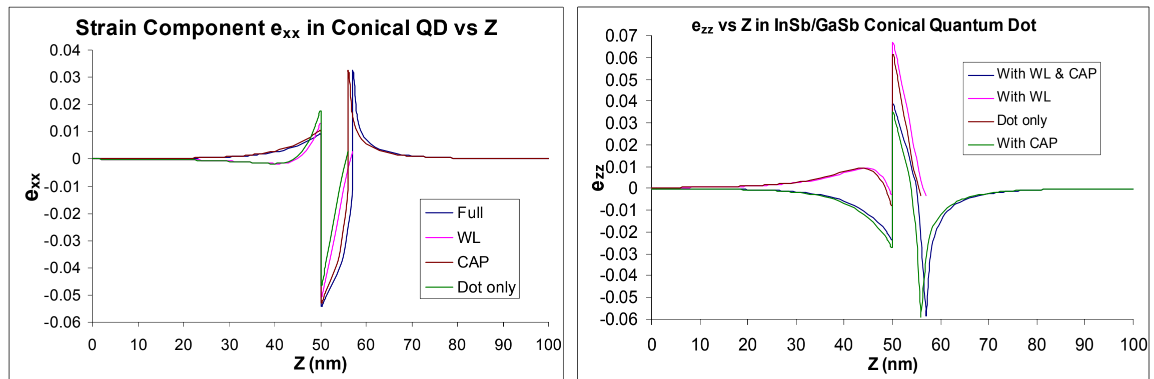

(a) e_{xx} (b) e_{zz}

Figure 5.5 : Strain Field Component for InSb/GaSb Conical QD

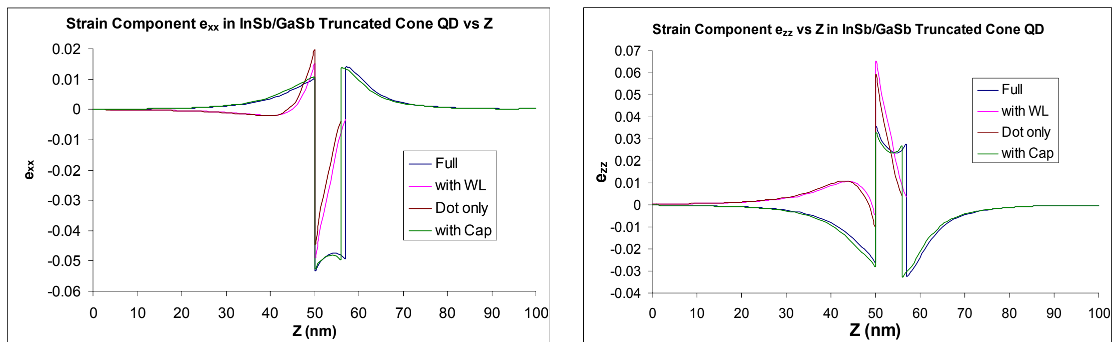

(a) e_{xx} (b) e_{zz}

Figure 5.6 : Strain Field Component for InSb/GaSb Truncated Conical QD

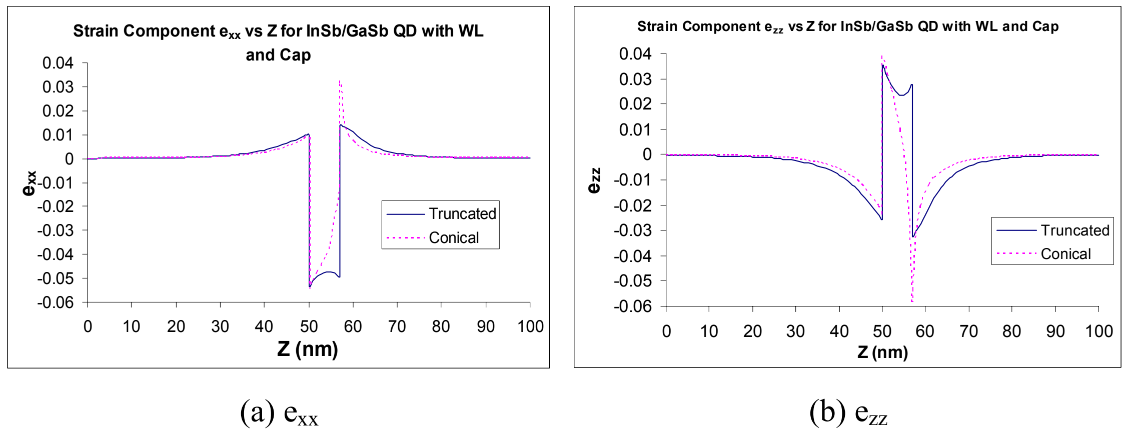

(a) e_{xx} (b) e_{zz}

Figure 5.7 : Comparison of Strain Field Distribution Between Conical and Truncated Conical QD

As already mentioned above, the effect of wetting layer on the strain distribution is very small but the effect of capping layer on the strain distribution is quite significant as we can see from the e_{zz} component of the strain. The main difference between conical and truncated conical QDs lies in the fact that the strain field in the conical dot varies exponentially while it is approximately constant in the truncated cone dot. Therefore, the strain relaxation is much higher in the conical dot.

In the case of capped conical QDs, the e_{zz} strain component changes its sign with increasing height within the dot, becoming negative at the top of the dot. This feature is also common for pyramidal dots [4]. This is due to the artificial divergence from the continuum mechanics calculation and is not real [4,5]. Therefore, for the remaining sections, the discussion will only concentrate on the truncated conical QD although similar calculations have also been carried out using Comsol Multiphysics for all the QD shapes and structures discussed.

5.1.2.2 ANSYS vs. COMSOL MULTIPHYSICS

This is to compare or determine which package gives better or more accurate results. The same geometries and parameters have been adapted in both packages but the modelling was done in the framework of thermoelasticity using ANSYS and the framework of initial strain in Comsol Multiphysics. Both models gave identical results as shown in Figure 5.9.

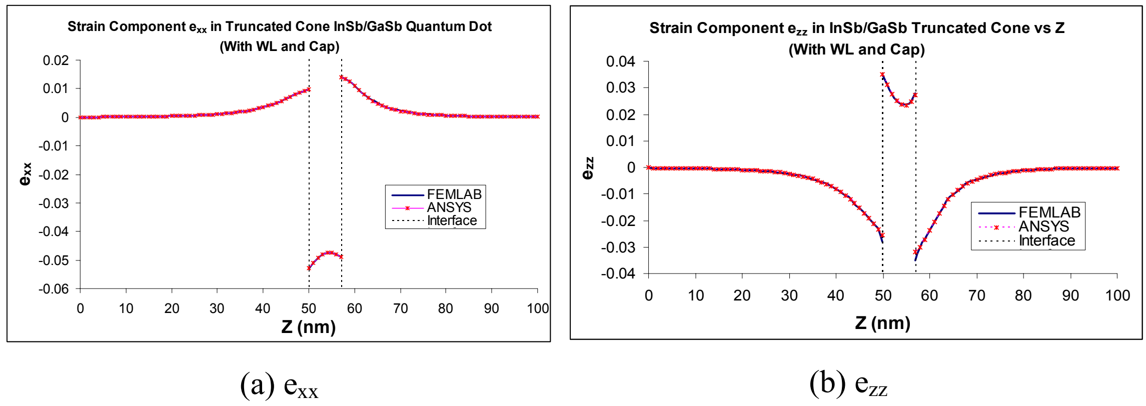

(a) e_{xx} (b) e_{zz}

Figure 5.9 : Strain Component in InSb/GaSb Truncated Cone Quantum Dot with Wetting and Cap Layer Modelled by ANSYS and Comsol Multiphysics

As we can see from the plots, the results from both ANSYS and Comsol Multiphysics are in excellent agreement. However, they have pros and cons in terms of data manipulation and defining geometry.

- ANSYS gives the data with separation by the material type, i.e. at the interface, ANSYS provides the data for the two materials but Comsol Multiphysics does not.
- Comsol Multiphysics describes the strain in term of total strain of the form

$$e_T = e_{el} + e_{th} + e_0 \quad (5.7)$$

  where, e_{el}, e_{th} and e_0 are elastic strain, thermal strain and initial strain respectively. In order to obtain the strain field component, the initial strain needs to be subtracted out from the total strain but ANSYS provides just the elastic strain.
- In geometry creation, the graphical user interface in Comsol Multiphysics enables the user to create the model as well as the composite material faster and more straightforwardly compared with ANSYS.

Comsol Multiphysics is also more favourable because it can be used in parallel with Matlab to perform further strain-modified band profile calculations; which will be discussed later. The single-particle states of the SAQDs system can also be determined conveniently through the multiphysics coupling function using Comsol Multiphysics. The partial differential equation module can be coupled with the structural mechanic module to solve for the energy levels after the strain tensors were obtained.

5.1.3 3-DIMENSIONAL MODEL vs. 2-DIMENSIONAL MODEL

The main advantage of the 3-D model is that it gives a complete picture of the stress and strain distribution of the QD since the stresses and strains distribution of arbitrary plane can be obtained easily. The draw back of the 3-D model is that it requires intensive computation and very high memory consumption. However, with the progressive improvement of the computer power in terms of processor speed and multi-core processor; incorporated with the capability in accepting more physical memory and high resolution graphic card, the 3-D modelling is now feasible at acceptable cost.

Comsol Multiphysics has been used to perform the 3-D modelling of a truncated conical capped QD with wetting layer and the results are shown in Figure 5.10 below.

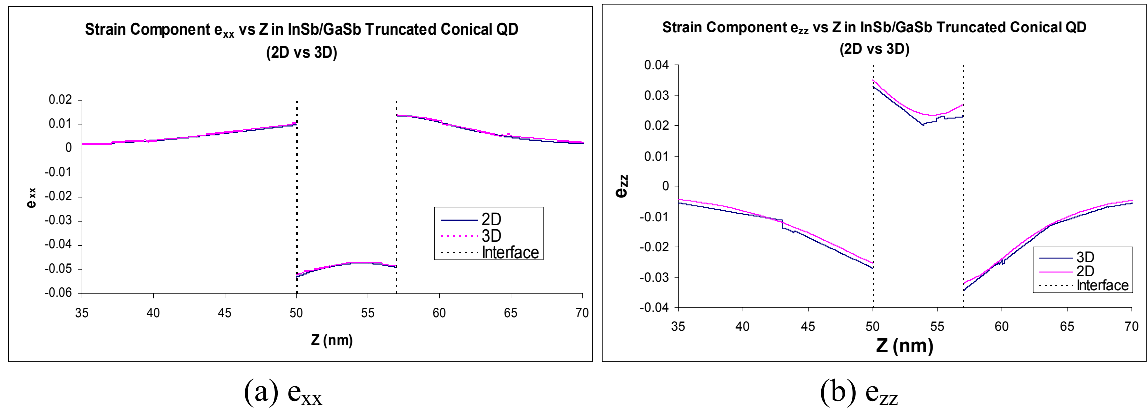

(a) e_{xx} (b) e_{zz}

Figure 5.10 : Strain Field Component in InSb/GaSb Truncated Cone QD with Wetting and Capping Layer for 2D and 3D Model

From the figure, there is tensile strain in a thin region of the matrix just below and above the dot due to lattice mismatch in the e_{xx} and e_{yy} components whereas in the e_{zz} component, the matrix experiences compressive strain. This is because the dot is forcing the matrix lattice constant to be that of InSb. However, in the dot region, the situation is reversed. e_{zz} is positive and e_{xx} and e_{yy} are negative because the matrix now attempts to force the dot lattice constant to be that of GaSb.

As one can see from Figure 5.10(a), both 2-D and 3-D models gave identical results for the e_{xx} strain component (also e_{yy} by analogy). This is due to the in-plane symmetry of the truncated conical shape. This situation changes when the modelling is performed for a highly asymmetric shape such as the pyramidal dot (Chapter 6) taking into account the anisotropic nature of the zinc-blende III-V semiconductors.

From Figure 5.10(b), there is some discrepancy between the 2-D and 3-D models when we look at the e_{zz} component of the strain. This is because there is no symmetry between the bottom and top surface of the truncated conical dot. The result from the 2-D model is rather smooth and slightly different to the 3-D model.

Nevertheless, 2-D axial symmetry model is applicable for certain dot shapes that possess symmetry. However, the shapes of SAQDs structures often do not possess the symmetry property. Hence, it is advisable to perform the modelling by using the full 3-D model in order to study the strain distribution across the whole structure of the SAQDs systems.

5.1.4 EFFECTS OF ANISOTROPY

In nature, typical semiconductor materials having zinc-blende cubic crystalline structures show anisotropic stress-strain behaviour. Therefore, it is necessary to model them using anisotropic material properties in order to investigate the effects of strain distribution on the electronics structure of QDs system more accurately. The anisotropic properties for InSb and GaSb are listed in Table 4.1 (Chapter 4).

Figure 5.11 shows the comparison of hydrostatic and biaxial strain between an isotropic and an anisotropic model for a InSb/GaSb truncated conical QD along the [001] direction through the centre of the dot. From the figure it can be seen that there is a difference in the magnitude of the hydrostatic strain. In the isotropic model, the hydrostatic strain is constant across the dot at about -0.07 whereas for the anisotropic model, a maximum hydrostatic strain of about -0.08 occurred at the centre of the dot, a difference of about 14%. The hydrostatic strain is also higher at the dot-matrix interface for the anisotropic model.

For biaxial strain, the maximum strain occurred at the base of the dot for both models but the isotropic model showed a drop in magnitude from the base to the top surface of the dot whereas the strain is nearly constant for the anisotropic model. These results generally show that elastic anisotropy should not be neglected in the analysis of QD structures, but in order to examine the extent of it effects on the analysis further calculations of the band edge profiles need to be carried out and this will be discussed in the next section.

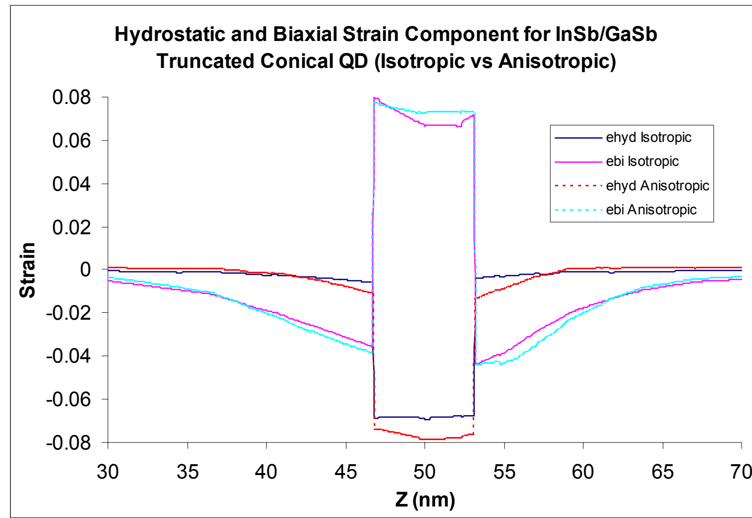

Figure 5.11 : Comparison of Hydrostatic and Biaxial Strain for Isotropic and Anisotropic Model of InSb/GaSb Truncated Conical QD

5.2 STRAIN EFFECTS ON BAND EDGES

As mentioned earlier, the introduction of homogeneous strain in bulk semiconductors changes the lattice parameter and, in some cases, the symmetry of the material. These in turn produce significant changes in the electronic band structure. Homogeneous strained configurations can quite generally be divided into two: the hydrostatic component that gives rise to a volume change without disturbing the symmetry and the shear component that in general reduces the symmetry present in the strain-free lattice. A homogeneous strain induces change in energy gaps and when the symmetry of the crystal is reduced, lifts degeneracies.

Using the strain profiles of Figure 5.11, the shifts in the conduction, heavy-hole and light-hole band edges due to the strain at the Brillouin zone centre (*k=0*) were calculated and the results are shown in Figure 5.12 as a function of the distance along the [001] direction. The split off band was not considered here because the band edge energy for the split off band is very low and makes no contribution to confining carriers.

The InSb dot provides the confinement potential for both electrons and holes. The conduction band has a potential well of about 120 meV as shown in Figure 5.12 compared to about 550 meV for the unstrained heterostructure. This implies that the dominant effect of the strain is that the dot experiences a large increase in its bandgap due to the considerable hydrostatic pressure. The valence band has a more complicated

structure. If we could somehow turn off the strain, the holes would be confined to the InSb by a well 30 meV deep. However, with the presence of strain, the potential well becomes 80 meV at the base of the dot, tapering off to a depth of about 50 meV at the apex and this makes the dominant contribution to the hole confinement potential. A remarkable feature of the valence band is that it is peaked near the base and at the apex of the dot, which is clearly shown in the inset of Figure 5.12.

When elastic anisotropy is considered, it is noticed that the conduction band edge within the dot inclines upward whilst it is almost flat with the isotropic assumption. As a result, differences in the potential at the dot apex reach 60 meV. However, confinement potentials in the valence band do not seem to be appreciably sensitive to the choice of elasticity type. Consequently, the underestimation of the upward shift of the conduction band edge due to the assumption of isotropy would result in the prediction of both a narrower bandgap and deeper potential well in the QD region than is predicted from the anisotropic model. Such changes in direct bandgap and potential well depth would lead to the prediction of different optoelectronic properties. Therefore, consideration of elastic anisotropy in the calculations would be necessary for improved design and analysis of optoelectronic devices based on QD structures.

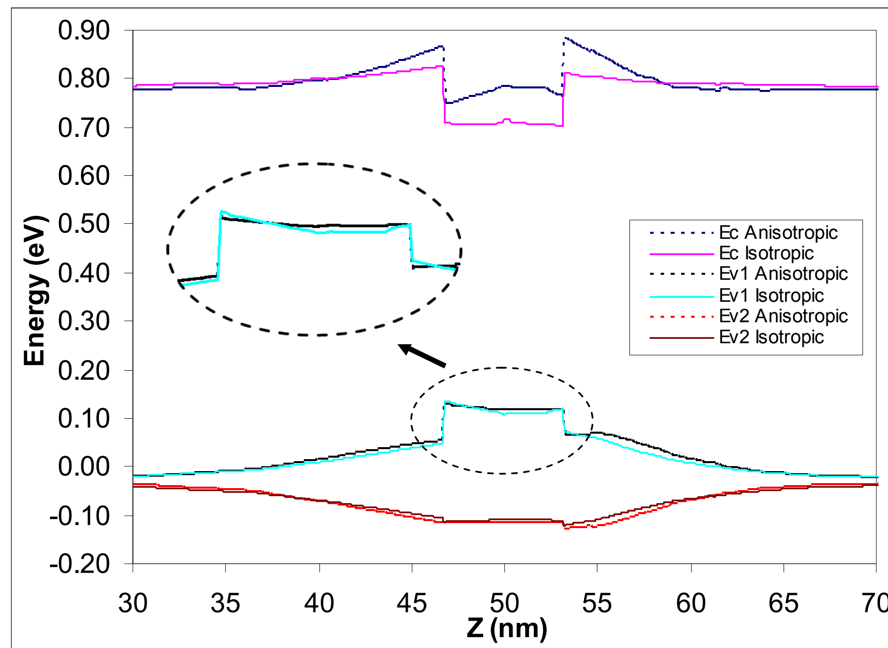

Figure 5.12 : Band Edges Diagram for InSb/GaSb Truncated Conical QD Along [001] Direction Through the Centre of the Dot

The band edge diagram along the [001] direction is a good representation of governing localization potential for electrons and holes through the centre of the dot.

However, it is only valid in the highest symmetry position, where the shear component of strain is zero (i.e. along [001] direction through the centre of the dot). It is often considered in previous publications [5-9]. When the band edge diagram along the [001] direction is plotted shifted from the dot centre, a different band edge diagram is obtained as shown in Figure 5.13. Therefore, the band edge diagram along the [001] direction is not capable of illustrating the whole picture of strain-induced modification of the band profile for the whole QD structure.

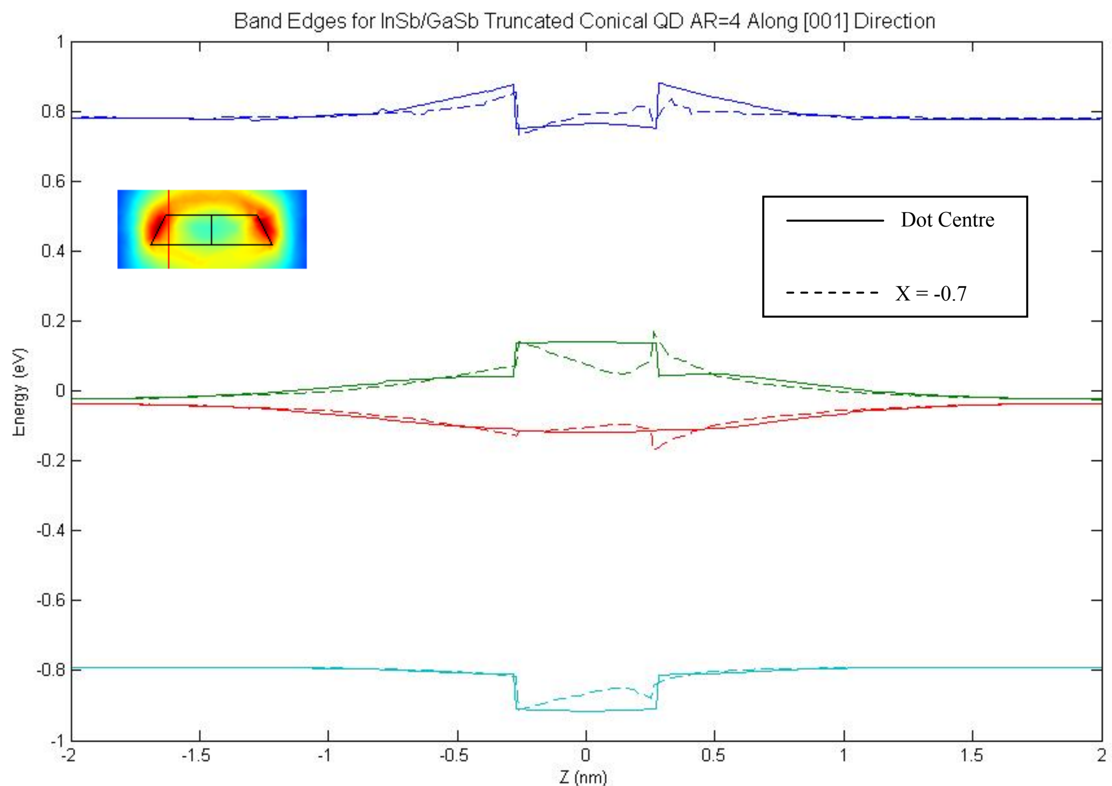

Figure 5.13 : Band Edges Diagram Plotted Off Centre at x=-0.7

A more accurate picture of the strain-modified band edges can be obtained by calculating the energies of the conduction band and upper valence band and plotting them in a two-dimensional cross section plot. Figure 5.14 and Figure 5.15 show the conduction band and upper valence band edge respectively in the (100) and (110) planes cross section based on the elastic anisotropy model.

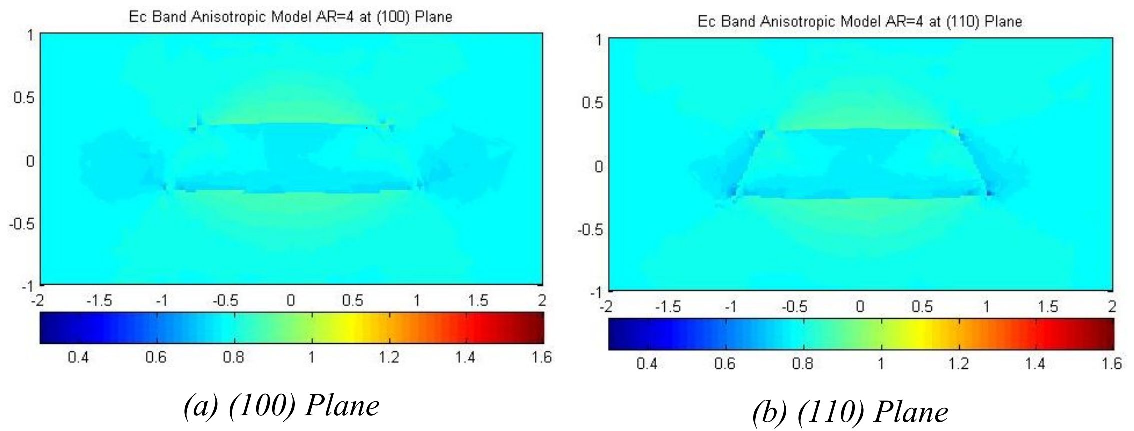

(a) (100) Plane *(b) (110) Plane*

Figure 5.14 : Conduction Band Edge Presented in (a) (100) Plane and (b) (110) Plane

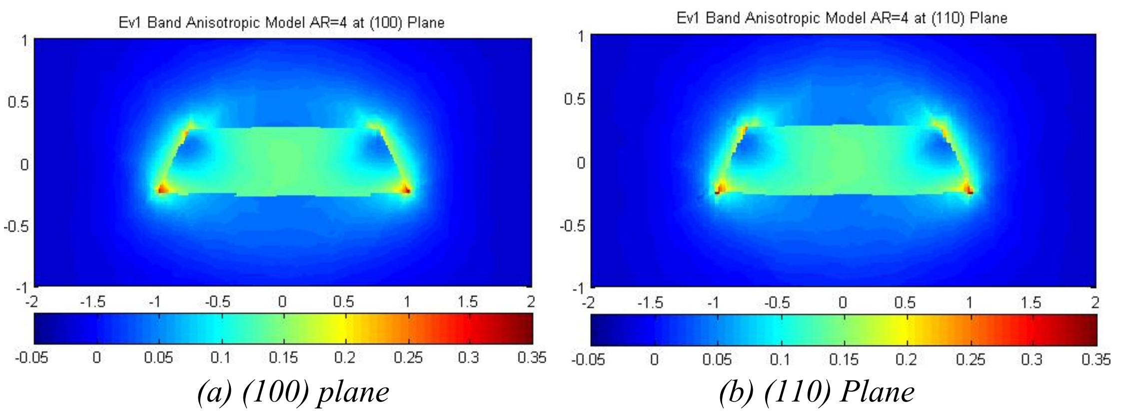

(a) (100) plane *(b) (110) Plane*

Figure 5.15 : Upper Valence Band Edge Presented in (a) (100) Plane and (b) (110) Plane

The two dimensional cross section plots of band edges enable us to examine the strain-modified band profile more clearly as the band edge distribution can be obtained for arbitrary plane and they provide a complete picture of band edge distribution throughout the whole QD structure. As we can see from Figure 5.14, the minimum in the conduction band occurs at the edge of the QD-matrix interface whereas Figure 5.15 shows that the upper valence band maximum also occurs at the edge of the QD-matrix interface.

The effect of the aspect ratio of the dot on the band edges has also been investigated and the two dimensional cross section plots of band edges for the truncated conical QD with aspect ratio 2, 4, 6 and 8 in (110) cross-section plane are shown in Figure 5.16. As we can see from the figure, the conduction band moves down while the valence band moves up in the energy colour scale. Therefore, the bandgap of InSb reduces with increasing aspect ratio.

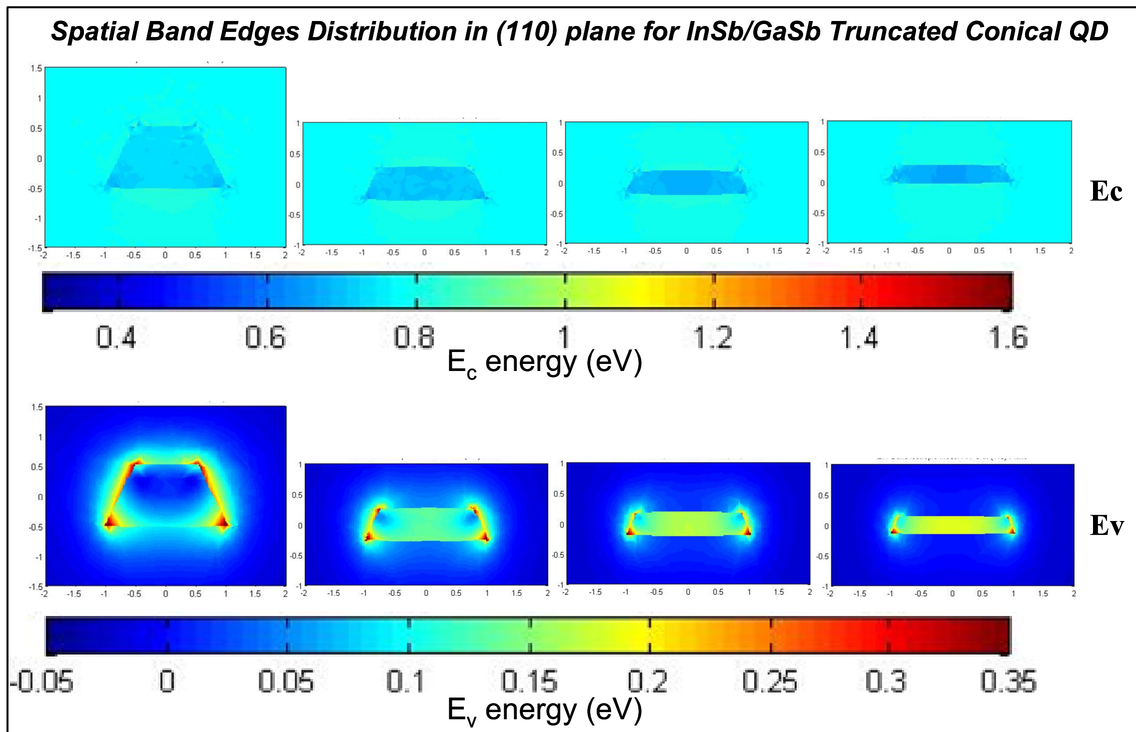

Figure 5.16 : Spatial Band Edges Distribution in (110) cross-section plane for InSb/GaSb Truncated Conical QD with Aspect Ratio 2, 4, 6 and 8

5.3 SUMMARY

The InSb/GaSb conical and truncated conical QD heterostructures are analysed using 2-D axial symmetry using ANSYS and both 2-D and 3-D models using Comsol Multiphysics. Both packages provided results in very good agreement but Comsol Multiphysics is more powerful and preferable because it can be used in parallel with Matlab to perform band structure calculations. Though the 2-D model provides a good approximation and satisfactory results, it may overlook the symmetry property of the zinc-blende crystal structure. On the other hand, the 3-D model allows strain in any arbitrary plane through the model to be obtained easily. However, the 3-D model is sensitive to finite element meshing especially near the edges of the dot-matrix interface.

Due to the lattice mismatch, there is a tensile strain in the matrix just below and above the dot and compressive strain in the dot in xx- and yy-direction and the other way round in the zz-direction. There are various factors that may affect the strain distribution such as, height of the cap layer, the shape of the dot and the aspect ratio of the dot but only the shape and aspect ratio of the dot have been investigated.

Strain-induced band edge diagrams have also been calculated for a truncated conical QD based upon model solid theory and standard-deformation-potential theory. Hydrostatic strain shifted the conduction band of InSb 430 meV up while the biaxial strain removed the degeneracy of the valence bands. The conduction band moves down while the valence band moves up in energy (see colour scale in Figure [5.16]) with increasing aspect ratio; in other words, the bandgap of the InSb dot reduces with increasing aspect ratio.

Though the band edge diagram along the [001] direction is a good representation of the dominant localization potential for electrons and holes, which is often considered in the literature it is only valid in the highest symmetry position, which is through the centre of the dot, where the shear component of strain is zero. The two dimensional cross section plots of band edge enable us to examine the strain-modified band profile more clearly as the band edge distribution can be obtained for an arbitrary plane and they provide a complete picture of the band edge distribution throughout the whole QD structure.

References:

[1] T. Benabbas, P. Francois, Y. Androussi, and A. Lefebvre, J. Appl. Phys. **80**, 2763 (1996).

[2] G. R. Liu and S. S. Quek Jerry, Semicond. Sci Technol. **17**, 630 (2002).

[3] V. Siklitsky and A. Tolmatchev, 2001. *New Semiconductor Materials. Characteristics and Properties: Physical Properties of Semiconductors* [Online]. St. Peterburg: Ioffe Institute. Available: http://www.ioffe.ru/SVA/NSM/Semicond

[4] V. –G. Stoleru, D. Pal, and E. Towe, Physica E **15**, 131 (2002).

[5] H. Shin, W. Lee, and Y. –H Yoo, J. Phys.: Condens. Metter **15**, 3689 (2003).

CHAPTER 6

IMPORTANCE OF ASPECT RATIO OVER SHAPE IN DETERMINING THE QUANTIZATION POTENTIAL OF SELF-ASSEMBLED ZINC-BLENDE III-V QUANTUM DOTS

6.0 INTRODUCTION

It has been shown that the misfit strain will dramatically affect the band structure of the SAQDs [1,2]. The shift or splitting in the conduction and valence bands can be expected to be as large as 80 meV per 1% of strain for typical values of the deformation potentials in III-V semiconductors [3]. As a typical example, the lattice mismatch in the InAs/GaAs SAQDs is ~7%, hence the strain-modified band-edge positions is expected to be comparable to or even larger than the band gap in the unstrained materials [4].

The band structure modelling taking into account the effects of mismatch strain have been reported for various QD shapes, such as flat cylinders [5,6], pyramids [7,8], lenses [4,9], and cones [10,11]. The studies include the comparative study of sphere and lens shapes of particular size [12], and the examination of the effect of height-to-base ratio for pyramid [13,14] and truncated pyramid [15] shapes. The common conclusion was that the effect of the dot shape (volume) on the electronic structure is significant. However, the more detailed trends appeared to be shape-specific only as the trends have commonly studied within single shape "families" (i.e., by varying the volume or aspect ratio of a pyramidal dot). Therefore, the question as to what extent the QD band structure is sensitive to particular shape details remains unanswered. This question is particularly important because the exact dot geometry is very difficult either to assess in the already grown structures, especially in the capped ones or to predict when designing new structures.

The shape of the dot affects the electronic structures in two ways, namely the "strain" effect and the "size" effect. For the "strain" effect, the dot shape alters the strain distribution in and around the dot and hence the strain-modified potential for both electrons and holes. On the other hand, the variation of shape affects the effective size quantisation in particular directions when some linear dimensions remain the same. Note that this size effect is different from the well-studied effect of simple size scaling

of dot of a fixed shape [7,8]. Since the contribution from the "strain" and "size" effects may be of opposite directions [15], it is more informative to consider them separately. Such an analysis is particularly effective when studying the "strain" effect by the continuum-elasticity approach, since the solution of the elastic problem is size independent and scalable. In this chapter, only the strain-induced modification of the confinement potential is treated in continuum-elasticity approximation. The size-quantisation energies are not considered.

The aim is to reveal the most important geometrical parameter(s) of QD of an arbitrary shape. We start by considering the ellipsoidal QD shape since it has the simplest strain distribution. The most important trends in strain and strain-modified confinement potential are analysed as a function of aspect ratio, which is the only variable shape parameter for an oblate ellipsoid. Next, the same trends are analysed for a number of the more complicated QD shapes as well as taking into account of the wetting layer. The calculations were done for the InAs/GaAs material combination which serves here as a well-known test system.

The results show that the basic features of the strain and the strain-modified band profile for a number of realistic QD shapes are determined by the aspect ratio only and much less sensitive to the other shape details. This allows us to justify approximating the QD shape to an ellipsoid and to propose a simplified model for analysis of strain-induced modifications of band profile in SAQDs. Based on the analytical solution of the elastic problem, this model provides a straightforward and relatively accurate description of the confinement potential in SAQDs.

6.1 ELLIPSOIDAL QUANTUM DOTS

In this section, the strain distribution and the resulting confinement potential for oblate ellipsoidal-shaped QD of various ARs are analysed. Starting with examining the simplest example of a spherical dot (i.e. ellipsoid of AR=1). Then the effect of increasing AR is examined. For comparison, the same trends are analysed for more complicated shapes (i.e. lens-, truncated cone-, and pyramid-shapes). Note that for all shapes, the strain distribution and the confinement potential are size-independent in the continuum-elasticity approximation.

6.1.1 GENERAL TRENDS In STRAIN DISTRIBUTION And STRAIN-MODIFIED BAND PROFILE For ELLIPSOIDAL QD

In this section, the strain and strain-modified quantisation potential are calculated for the oblate ellipsoidal QD as function of aspect ratio. The most important strain-induced features of the quantisation potential and their variation with aspect ratio are revealed. The isotropic approximation of the elastic problem is analysed in parallel with a numerical solution in order to reveal the effect of elastic anisotropy.

We start with an analysis of strain inside the dot in terms of the elastic energy density. Figure 6.1(a) shows the spatial distribution of the total elastic energy density for several aspect ratios obtained from numerical modelling in two-dimensional cross sections. It presents the (100) plane on the left and the (-110) plane on the right. Note that the homogeneous colour distribution inside the dot indicates homogeneous strain within the dot. This illustrates that the condition of homogeneous strain distribution within an ellipsoidal dot is still valid for the cubic anisotropy structure. With increasing aspect ratio, subtle changes are observed for the intensity of the colour inside the dot. This indicates a slight increase in the total elastic energy density.

As we have mentioned earlier, strain inside an ellipsoidal (001) dot can be represented as the sum of hydrostatic and tetragonal components. Figure 6.1(b) shows spatial distribution of the hydrostatic component of the strain energy density. As expected, hydrostatic strain inside the dot is also homogeneous. However, variation in the coloration intensity with aspect ratio is much stronger. Together with the subtle variation in total strain, this is indicative of re-distribution of strain between the two components.

Homogeneous strain inside the dot allows characterization using accurate single values. Figure 6.2(a) shows both the total strain energy density and its components as a function of the aspect ratio. Circles represent results obtained from numerical modelling. One can see that the hydrostatic component strongly decreases and the tetragonal component increases with AR. Such behaviour is in sharp contrast to the weak variation in the total strain. The latter indicates that there is no essential re-distribution of misfit strain between the dot and the matrix. Thus, re-distribution of strain between the hydrostatic and tetragonal components is a prevailing manifestation of variation in strain inside the dot with aspect ratio for the (001) growth plane.

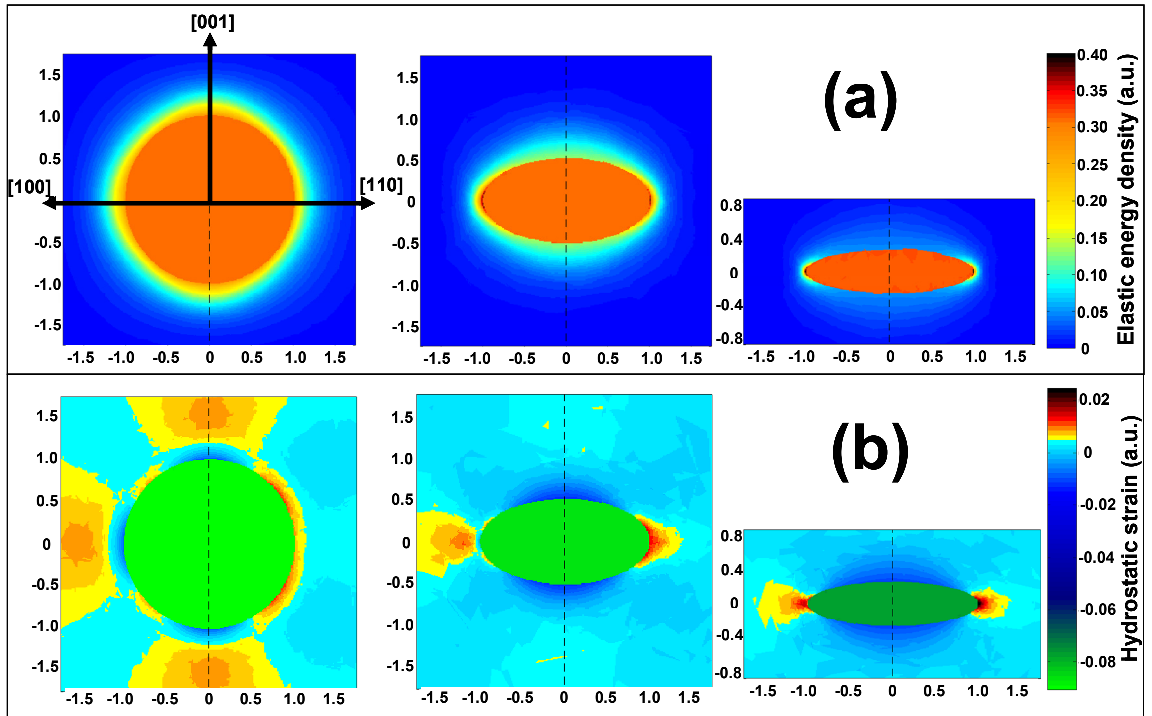

Figure 6.1: (a) Spatial distribution of total strain energy density, (b) Spatial distribution of hydrostatic strain component; inside and around InAs/GaAs (001) ellipsoidal QD for different aspect ratios.. Each graph shows (100) and (−110) cross-section planes through the dot centre on the left- and right-hand-side parts, respectively.

Homogeneous strain inside the dot also results in well-defined positions of the edges of the conduction and valence bands. Their values, obtained from numerical calculations, are shown by circles in Figure 6.2(b). In agreement with Eq. (4.24), the conduction band edge shifts downwards with the aspect ratio, following the hydrostatic strain. As to the valence band, the major effect comes from increased splitting induced by the shear strain component. Indeed, shear deformation potentials b and d, Eq. (4.26), are typically 2-5 times large than the hydrostatic potential, a_v. Hence, the top valence band shifts upwards. As a result, the band gap inside the dot drops from ≈ 1.05 eV for AR = 1 to ≈ 0.6 eV for AR = 20, with almost 60% of the effect originating from the shift of the valence band.

In the limit of infinite aspect ratio, both the strain and the band-edge positions approach the quantum-well values, which are shown by short solid bars in the right-hand side of Figures 6.2(a) and 6.2(b), respectively. Note however that even for AR = 20, the difference between the quantum dot and quantum-well values is still large.

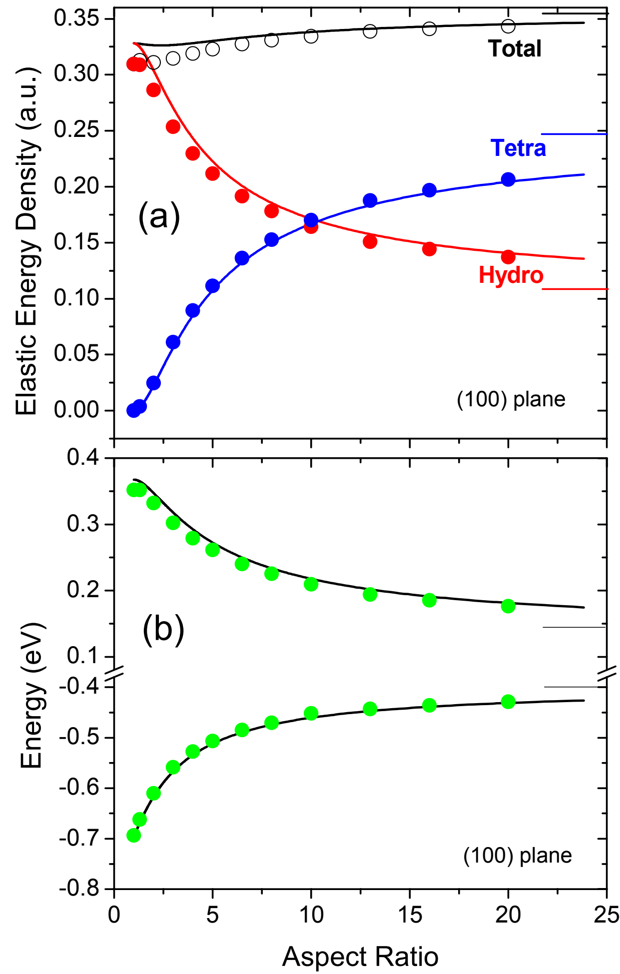

Figure 6.2 : (a) Total elastic energy density and its hydrostatic and tetragonal components inside InAs/GaAs (001) ellipsoidal quantum dot as a function of aspect ratio AR. (b) Positions of conduction and top valence band edges inside InAs/GaAs (001) ellipsoidal QD as a function of AR. Symbols are numerical results obtained within cubic elastic anisotropy model; solid lines are analytical results obtained within isotropic elasticity model; short solid bars in the right-hand side of the plots are values for InAs/GaAs (001) quantum well.

In order to analyse the effect of real cubic elastic anisotropy, the same calculations for ellipsoidal QDs were performed analytically in the isotropic elastic approximation (IE model). The results are shown in Figures 6.2(a) and 6.2(b) by solid lines. In general, a good agreement is observed between isotropic and anisotropic elasticity approaches. In particular, the difference is negligible for the valence band edge; there is a minor systematic overestimation for the conduction band-edge position in the isotropic model. The underlying variations in the strain components are also well reproduced in the isotropic approximation, both qualitatively and quantitatively.

The aspect ratio of the dot also affects the strain distribution in the matrix near the heterointerface. One can see from Figure 6.1(a) that the strain energy density in the matrix is distributed nearly homogeneously around the spherical dot, being weakly modulated by elastic anisotropy. When the aspect ratio of an ellipsoid increases, the strain is concentrated near the sharp edge of dot, while the average strain density energy along the flattened part of the interface decreases. Such behaviour is in agreement with the unstrained matrix condition for infinite AR (quantum-well limit).

At the same time, variation of the relatively weak hydrostatic strain component with AR is more complicated. One can see from Figure 6.1(b) that even for a spherical dot, areas of hydrostatic contraction and hydrostatic dilation alternate along the heterointerface. Such modulation is a clear manifestation of elastic anisotropy. With increasing AR, areas of hydrostatic contraction extend over the flattened parts of the heterointerface, whereas hydrostatic dilation is concentrated near the sharp edge of the ellipsoid. Such a distribution of shear and hydrostatic strain components results in a complex modification of the band profiles.

Figure 6.3 shows the profiles of the valence and conduction bands *in the matrix at the interface with the dot* for three aspect ratios. It presents the positions of the conduction and three valence band edges along a representative contour [100] – [110] – [001] – [100] (which is marked by a bold line in the insert to Figure 6.3). Dotted lines represent numerical results obtained in the anisotropic approximation, while solid lines show analytical results in the isotropic elasticity model. Dashed lines show positions of the conduction and top valence bands edges inside the dot.

Results in Figure 6.3 clearly reveal effects from cubic anisotropy, in comparison to the IE model. For the spherical dot (AR = 1), the conduction band edge position oscillates around its value for the unstrained material. Such behaviour reflects modulation in hydrostatic strain around the interface. As mentioned above, it is a pure manifestation of elastic anisotropy. In contrast, the IE model suggests flat distribution of the conduction band edge along the interface, which reflects the zero hydrostatic strain produced by a spherical inclusion in the isotropic elastic matrix. For the valence band, a weakly varied strong splitting of the valence band is well reproduced in both elastic approximations for the same spherical shape. This splitting reflects a combination of a

large, nearly homogeneous, shear strain at the heterointerface and a weak anisotropy of shear deformation potential (see also discussion in Section 6.4.2 below).

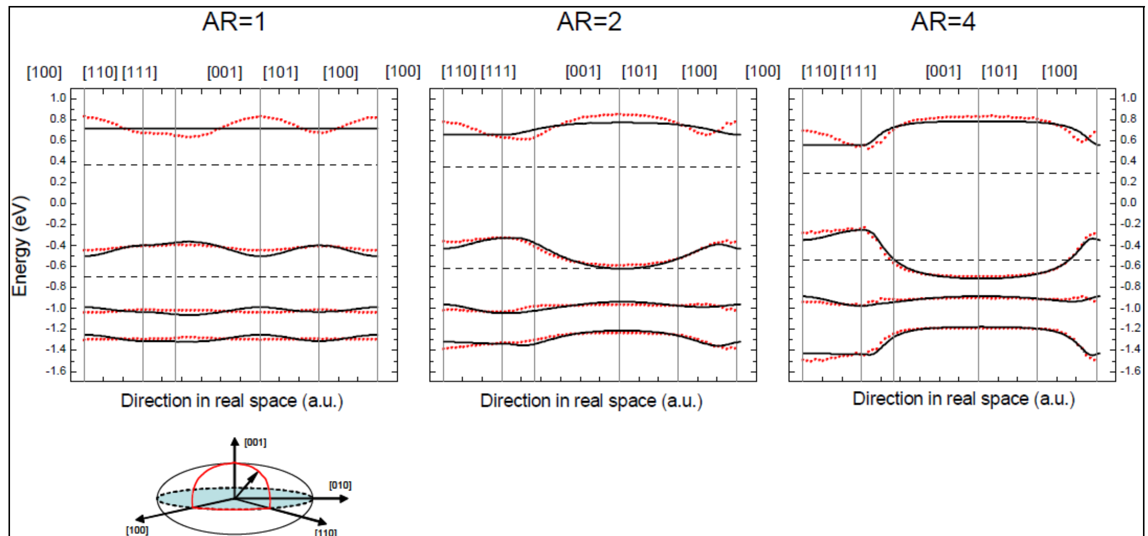

Figure 6.3 : The band-edge profiles in the matrix at the heterointerface for different aspect ratios: symbols—numerical results obtained for cubic elastic anisotropy; solid lines—calculated within the isotropic elasticity approximation (IE model). Dashed lines show the band-edge positions in QD. Insert picture shows the contour at the heterointerface, along which the band profiles are presented.

As the dot flattens (AR = 2 and AR = 4), the strain-induced valence band splitting concentrates near the sharp planar edge ([100] – [110] segment in Figure 6.3). This is in agreement with the strain redistribution shown in Figure 6.1(a). The splitting is also well reproduced in the IE approximation. The same part of the heterointerface is also characterized by a downshift of the conduction band edge. This is due to dilation (see also Figure 6.1(b)), which is reproduced in both approximations, but to a different extent. At the flattened parts of the heterointerface, small splitting in the valence band indicates low residual shear strain, while moderate uplift of the conduction band reflects the build-up of compressive hydrostatic strain. One can see that there is a very good agreement between the two models for the flattened parts of heterointerface around the [001] direction.

The above results show that major discrepancies between the isotropic and anisotropic elasticity approximations are observed only for the conduction band in the matrix. Moreover, these discrepancies are not important in determining the electronic properties of the QD. Essentially, at low ARs, cubic anisotropy results in directional modulation of the depth of the electron confinement potential. From this we can conclude that the flat conduction band profile in the isotropic model provides a good

approximation for the mean confinement potential. This is not going to have a strong effect on the dot energy spectra, because in a spherical dot, all directions contribute equally to size quantisation. For flatter dots with larger AR, the discrepancy is limited to the depth of the confinement potential in the in-plane directions. These directions provide the least contribution to the size-quantisation energy. Therefore, the energy spectra of the dot cannot be strongly affected. Further analysis (Section 6.3) shows that the effect becomes even weaker if the wetting layer is taken into account.

Finally, we note that the overall agreement between isotropic and anisotropic approximations is good. This suggests that, although the above analysis was performed for the (001) growth plane, a qualitatively similar modification of band profile is expected for an arbitrary growth direction.

6.2 REALISTIC QD SHAPES

The above analysis revealed some features of the strain-modified band profile in ellipsoidal QDs, as well as trends in its modification with the AR. To find whether they are specific for an ellipsoid, we performed a series of numerical calculations for a number of realistic QD shapes. These include a rather "smooth" hemispherical lens (dome) shape, as well as a highly "anisotropic" square-based pyramid. The results of band profile calculations are presented in Figures 6.4. Cross-sections for the same representative planes, (010) and (–110) are shown. Geometry details for the lens, pyramid and truncated-cone shapes are given in the insert to Figure 6.4(a). Results for the ellipsoidal shape are also shown for comparison.

6.2.1 GENERAL TRENDS In STRAIN DISTRIBUTION And STRAIN-MODIFIED BAND PROFILE For REALISTIC QD SHAPES

For non-ellipsoidal shapes, the potential profile for both electrons and holes is inhomogeneous across the dot. One can also notice that the profile becomes more homogeneous at larger ARs. For dots of ***all*** shapes, the energy of the conduction band edge decreases and that of the valence band edge increases with the AR. These trends are indicated by variation of the overall brightness of the dot image, as shown in Figure 6.4.

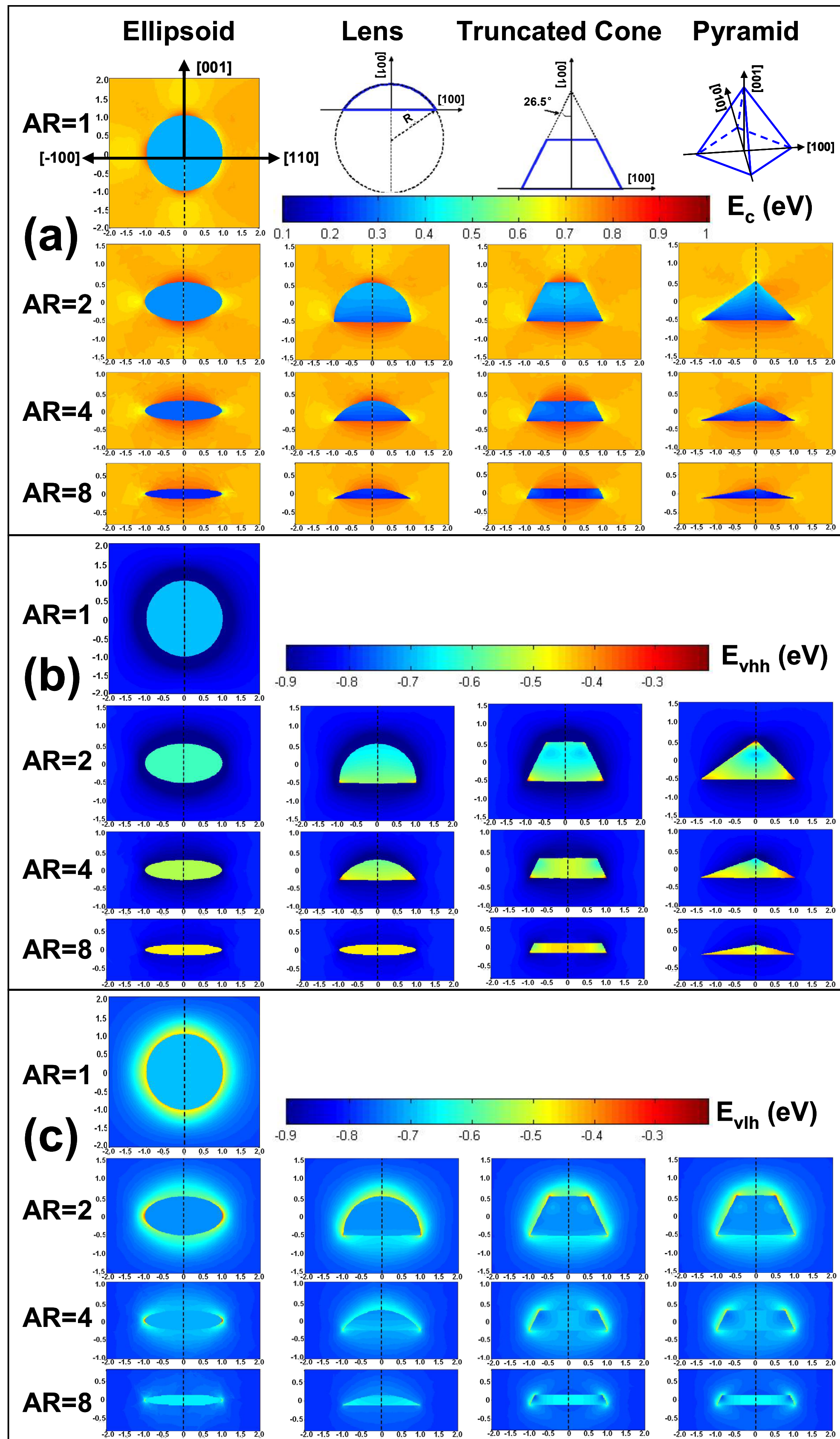

Figure 6.4 : Band profile for several aspect ratios for isolated InAs/GaAs (001) QDs of different shapes. Each graph shows (100) and (−110) cross-section planes through the dot centre on the left- and right-hand-side parts, respectively: (a) conduction band, (b) heavy-hole valence band, and (c) light-hole valence band. Inserts illustrate the parental geometry details for the QDs.

At low AR, the strain effect on the conduction band edge can be described qualitatively as uplift (darker areas in Figure 6.4(a)) at some regions of the heterointerface, which coexists with downshift (lighter areas) of comparable magnitude in other regions. (This behaviour has been reproduced in earlier calculations for different QD shapes. [1,3-14])

Modification of the conduction band edge with AR in Figure 6.4(a) displays a similar trend for all shapes. It can be described as the development of uplift (darker areas) near the flattened sides of the QD accompanied by downshift (lighter areas) along the sharp in-plane corners. It is notable that the uplift is observed even for the pyramidal shape, despite its sharp tip! Such a band profile matches the hydrostatic strain profile depicted in Figure 6.1(b) for the ellipsoidal shape.

For the valence band, strain produces significant band bending in the matrix at low ARs and the valence band splits into heavy- and light-hole bands. This matches the nearly homogeneous valence-band splitting for AR = 1, shown in Figure 6.3. The effect of shape and AR on the heavy-hole band profile is much stronger as can be seen in Figure 6.4(b). For ellipsoidal dots, the energy within the dot is constant. As the AR is increased, the heavy-hole band within the dot moves up in energy, forming a deeper confinement for the holes. The increase in the confinement energy is as large as ≈ 200 meV when the AR changes from 1 to 8. One can also note that there are darker blue areas in the matrix near the interface, which are lower in energy than in the matrix away from the dot. This is due to the downward band bending, which increases the heavy hole confinement even further.

The light-hole band profile is shown in Figure 6.4(c). Again, homogeneous colour distribution within the ellipsoidal dot indicates constant energy. By comparing Figure 6.4(b) and 6.4(c), one can see that the light-hole band is much lower in energy within the dot. In addition, the band edge energy in the matrix near the interface is *higher* than it is away from the dot. This is due to the upward light-hole band bending near the interface.

For quantitative comparison, energy values of the band edges are averaged over the QD volume and the results are presented in Figure 6.5. These *averaged* values are shown in Figure 6.5(a) as a function of the AR. Symbols represent results for various

shapes, obtained in the cubic-anisotropy approximation. Analytical results for the isotropic ellipsoidal model are also included. A striking observation from this figure is that all values are close to each other for a given AR. This means that the band-edge energies are not so sensitive to shape details. The most prominent difference of ≈ 0.1 eV is found for the lowest AR. This value should be considered against the strain-induced increase in the band gap change up to ≈ 1 eV from 0.42 eV in the unstrained material. At higher AR, the differences become much smaller; this correlates with more homogeneous band profiles inside the dots. Also, there is a very good agreement between the isotropic and anisotropic models.

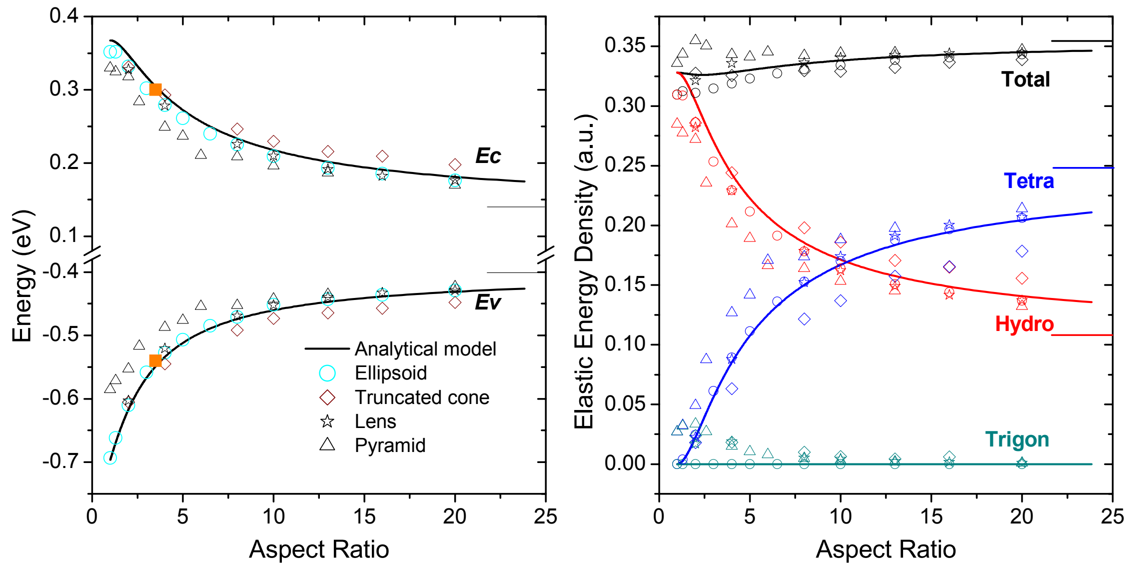

Figure 6.5 : (a) Conduction and upper valence band edges within InAs/GaAs (001) QDs as a function of aspect ratio: open symbols—averaged numerical results for cubic elastic anisotropy approximation for different QD shapes: circles—ellipsoid, triangles—pyramidal, diamonds—cone, stars—lens, and filled square symbols show the results from Ref. 4. Solid lines present analytical results obtained within the IE model for the ellipsoidal shape. (b) Elastic energy density within the InAs/GaAs (001) QD as a function of the aspect ratio. Symbols display averaged values of different components of the elastic energy obtained from numerical calculations. Solid lines represent the elastic energy density components for the ellipsoidal QD as obtained within the IE model. Short solid lines indicate values of the energy density components for an InAs/GaAs (001) quantum well.

To reveal underlying variation of strain inside the QDs, *averaged* values of strain energy density components are presented in Figure 6.5(b) for all the shapes as a function of the aspect ratio. One can see that the major features are mostly the same as for the ellipsoidal QD in Figure 6.2(a). In particular, hydrostatic and tetragonal strains are the dominant components except for very low AR. Enhancement in the tetragonal component at the expense of the hydrostatic one is also a major effect of the increased

AR. At lowest ARs, however, the trigonal and orthorhombic components are the most prominent shear components of the strain energy.

Taking into account ambiguity in the definition of the AR, agreement between the results for different shapes is remarkable, both in terms of strain and band profile. This justifies the role of the AR as a governing parameter related to the QD shape. Note that the importance of the AR correlates with an earlier suggestion [10] regarding the significance of such QD parameters as a volume.

We note that our results are in good qualitative agreement with those reported in the literature, taking into account deviations in materials parameters, elastic constants, dot shapes and/or the approximations used. A quantitative comparison with Ref. [4] is possible, where similar material parameters and averaging procedures were used for lens-shaped QDs of AR ≈ 3.5. Relevant averaged band-edge values are represented by filled symbols in Figure 6.5(a). They are in excellent agreement with our results.

Analysis of band alignment in the matrix also reveals features which are common for different QD shapes. This can be seen from Figure 6.4. In addition, representative one-dimensional (1D) band profiles along the [001] direction are provided in Figure 6.6. In each graph, band profiles for dots of the same size and AR are shown, which allows for easy comparison.

Accurate potential profile is sensitive to particular shape details, as one can see from Figure 6.6(a). It is worth noting, however, that because of alternating areas of uplift and downshift, a 1D band profile is also direction-specific. As a result, a 1D band profile along the [001] direction alone is not sufficient for representing the effective localization potential.

Moreover, the magnitude of the uplift is also similar for different dot shapes, which is demonstrated by the 1D band profiles along the [001] direction in Figure 6.6(b). The only substantial difference is observed at the pyramid tip. As mentioned earlier in Section 5.1.2.1, this effect is not real and very local, as is illustrated in Figure 6.6(c) by the band profile along the [001] line which is slightly shifted from the dot centre.

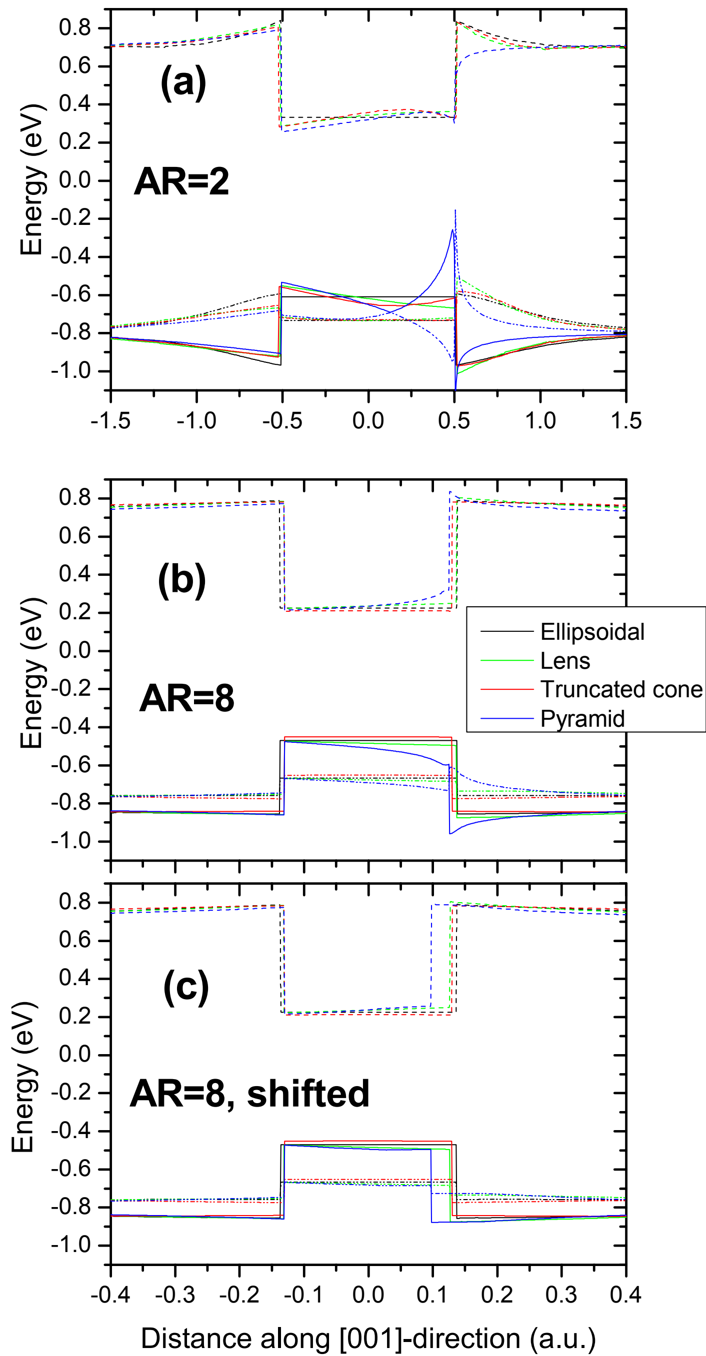

Figure 6.6 : Band-edge profiles along the (001) direction through the dot centre for different QD shapes: (a) aspect ratio=2; (b) aspect ratio=8; (c) aspect ratio=8 [same as (b)] along the (001) line shifted by 10% of the dot base size in the (110) direction. Dashed line – conduction band; solid line – heavy-hole band; and dashed-dot-dot line – light-hole band.

For a flat QD, the [001] direction produces the dominant contribution to the size quantisation of electrons. Hence, the one-dimensional conduction band profile in Figures 6.6(b) and 6.6(c) provides a good representation of the localization potential for electrons, even despite the effects near the sharp edges of the dot.

As mentioned earlier, strain produces significant band bending in the matrix at low ARs. Such a bending, together with "rounding-up" of sharp corners inside the QD, provides a significant uplift of the top valence band within some "shell" around the QD as shown in Figure 6.7 (brighter areas, or lighter colour). This plot is obtained by aligning the valence band maxima within the dot to the valence band maxima of the matrix.

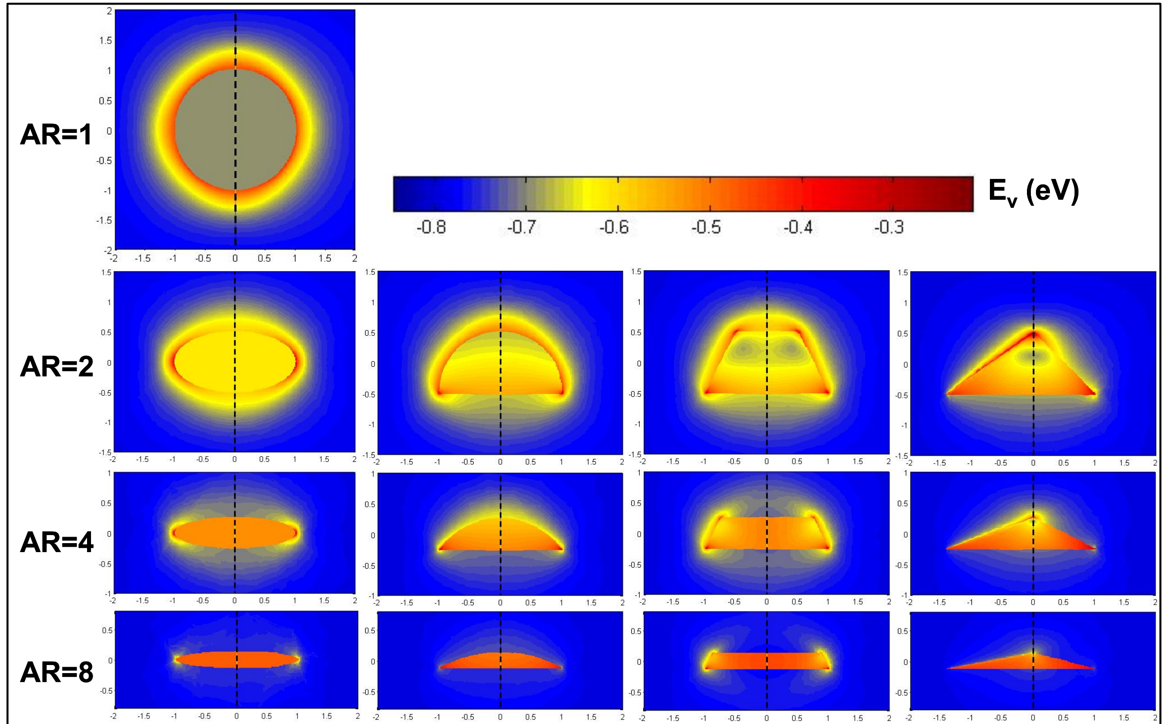

Figure 6.7 : Top valence band for several aspect ratios for isolated InAs/GaAs (001) QDs of different shapes. Each graph shows (100) and (−110) cross-section planes through the dot centre on the left- and right-hand-side parts, respectively.

The "shell" generally includes both sides of the heterointerface. Note that the top valence band has different origin on different sides of heterointerface: it is more heavy-hole-like inside the QD and light-hole-like on the matrix side. An exception is the ellipsoidal shape in which the "shell" includes the matrix side only. The valence band bending within this "shell" is of comparable magnitude for all shapes, as illustrated by 1D band profiles in Figure 6.6. Larger values are displayed at strain "concentrators" which are created at sharp corners of the QD. Note that the "shell" observed for a spherical QD, AR = 1 in Figure 6.7, has nearly spherical symmetry, to be compared to the strain distribution in Figure 6.1(a). At larger ARs, the valence band "shell" survives only in the form of "patches" along the sharp edges of the QD. This is observed for all shapes.

As a result, a representative valence band profile for flat dots along the [001] direction demonstrates a relatively weakly perturbed valence band edge at the matrix side of heterointerface, see Figures 6.6(b) and 6.6(c). This common trend indicates that for large ARs, the underlying strain variation is similar for all shapes and matches that for an ellipsoidal QD, (Figure 6.1(a)). Such an observation suggests that observation of the "shell" and its modification with the AR reflect some general (not shape-specific) features of strain distribution. These features may be sensitive only to the most basic material parameters, such as the ratio of elastic modulus in the dot and the matrix (assuming the same sign of misfit strain). Note that for III-V SAQDs, the elastic modulus ratio and the sign of the misfit strain are correlated, because the materials with larger lattice constant are typically softer. Therefore, the "shell" feature may be expected to be common for a wide range of III-V material combinations (see Ref. [12] for a particular example).

There are important consequences of the "shell" feature for the hole localization potential in the QDs, which we would like to point out. Bending of the top valence band within the "shell" enlarges the effective QD size seen by localized holes and smothers the sharpness of the confinement potential. Moreover, if the hole confinement potential in a QD is comparatively shallow, the "shell" provides a local energy minimum, in which the holes would tend to be localized. Actual localization is, of course, dependent on the QD size, which should not be too small. [12,16] However, even if "full" localization is not possible, the "shell" can essentially redistribute the hole density within the QD, affecting the electron-hole overlap, the oscillator strength of the interband transition, or the sign of the quantum-confined Stark effect [17,18]. Effects from the "shell" may be particularly important in case of type-II band alignment with the electrons localized in the matrix.

6.3 EFFECT of WETTING LAYER

The calculations above have not taken into account the wetting layer (WL), which is normally present in the SAQD heterostructures. We performed an additional series of calculations for the lens-shaped dots to include effects from the WL. The QDs were superimposed onto the WL to give varying relative thickness. (The relative thickness is defined as the ratio of the WL thickness to the overall thickness (height) of the whole structure, dot plus WL.) Figures 6.8(a) and 6.8(b) present 2D cross sections of the

potential profile for the conduction and upper valence bands, respectively. The 1D band profiles along the [001] line through the dot centre are shown in Figure 6.8(c). Results for a QD without the WL are also presented for comparison.

Variation in the band-edge positions with the WL thickness is represented by variation in brightness in Figures 6.8(a) and 6.8(b). The results indicate that effects from the WL on the strain-modified band profile are negligible, provided the relative WL thickness is small. This observation is in agreement with earlier results. [19] Quantitative estimates, available from Figure 6.8(c), show that a WL of relative thickness ≈ 0.2 results in a shift of less than 20 meV. At larger relative thicknesses, the effect of the WL appears to be equivalent to that of increased AR. This can be qualitatively understood if one considers a WL as an extreme case of the QD.

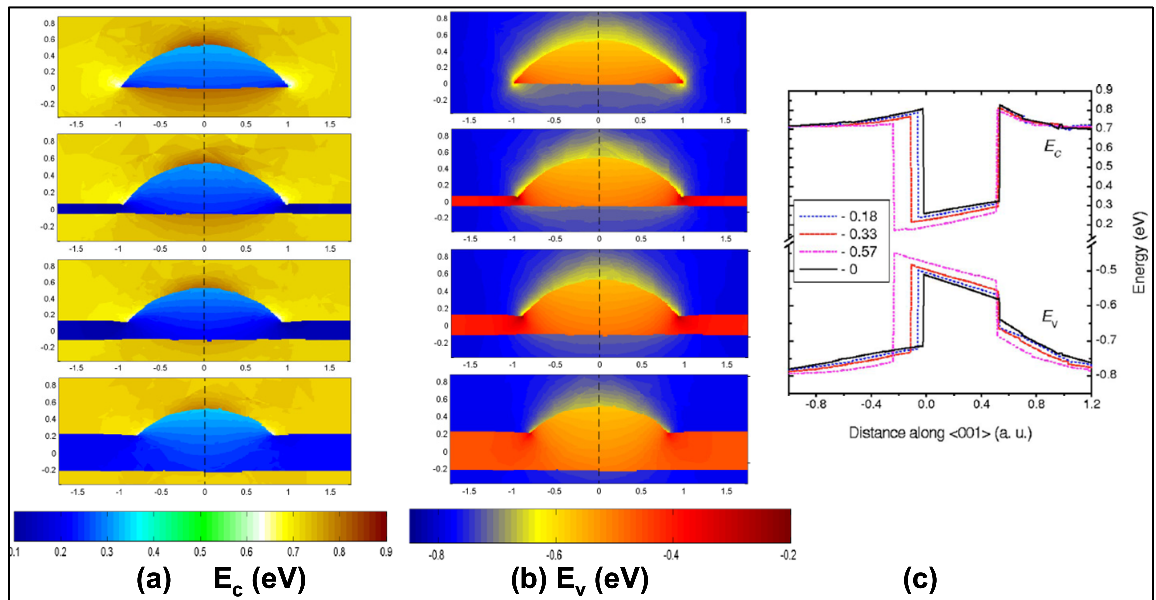

Figure 6.8 : Confinement potential for lens-shaped InAs/GaAs QD for different thickness of the wetting layer. (a) Conduction band and (b) top valence band. Each graph shows (100) and (−110) cross-section planes through the dot centre on the left- and right-hand-side parts, respectively. (c) band profile along the [001] direction through the dot centre.

If there is a region in which effects from the WL are noticeable, it is at the sharp in-plane edges of flat QDs. The WL affects the strain distribution in close proximity to them, as might be expected. The effect of the WL extends only over a distance comparable to its thickness. Effectively, the WL smoothes the sharp edges and therefore removes strain concentrators and the band profile perturbation, related to them. The effect from such a perturbation was not significant anyway, because the in-plane

direction provides the least contribution to the quantisation energies. The wetting layer makes this effect even smaller.

6.4 ELLIPSOIDAL MODEL

Analysis performed in Section 6.2 highlights the two most important results:

(a) Major features of the strain-modified confinement potential, revealed for the ellipsoidal shape, can be applied to characterize the effective confinement potential for all other shapes which we considered.

(b) Both the averaged confinement potential and its variation with the AR are similar for all shapes, reflecting similar trends in the strain redistribution.

From this we conclude that that

(1) The AR is a governing parameter related to the QD shape;

(2) Major features of the effective confinement potential can obtained in an ellipsoidal approximation for the QD shape, at least for the (001) growth plane and except for very low ARs.

The ellipsoidal approximation is very practical because a simple analytical solution of the elastic problem is available. The solution is based on the isotropic-elasticity approximation. We showed in Section 6.1 that it is sufficient to accurately reproduce the most important features of the quantisation potential.

One can question the validity of using averaged values of the band profile seen by electrons (or holes). We note that any variations in the potential profile within the dot happen on a very small spatial scale, because a quantum dot itself is small enough to enable quantum-mechanical confinement. Therefore, disregarding these variations is going to have little effect on the positions of size-quantised energy levels. Because of that, we suggest that the ellipsoidal model, which uses averaged localization potential, provides a good initial approximation for analysis of electronic spectra of QDs, with high predictive efficiency. Such an approximation is useful when the exact QD shape is not known and/or the most general features of the quantisation potential are of the interest.

Obviously, the ellipsoidal model does have limitations. For example, it is unable to reveal any spatial potential deviations from the average value. These may affect the density distribution of the electron and/or hole wave functions and hence parameters sensitive to their overlap, such as the oscillator strength.

We have arrived at similar conclusions after the same analysis and calculations were performed for the InSb/GaSb (001) system (see Section 6.5.1). In particular, the same general trends in strain variation with the AR were identified. Because of this, we would expect such trends to be common for a wide range of III-V materials, in view of the same symmetry of elastic moduli and deformation potentials. Thus, we suggest that the ellipsoidal approximation can be applied to the whole range of III-V zinc-blende SAQD systems. Moreover, in addition to compressively strained QDs, the ellipsoidal model appears to be applicable also to tensile-strained SAQD systems. Indeed, in the linear elasticity approximation, strain is symmetric with respect to the sign of stress, as is the strain-induced band shift and/or splitting, at least to the first order of magnitude.

6.4.1 GROWTH PLANE ORIENTATION

Here, we address the question, to what extent the ellipsoidal model is applicable to orientations of the growth plane other than (001). Good accuracy of the isotropic elasticity approximation suggests that effect of the AR on the quantisation potential should be similar, at least qualitatively, for any crystallographic orientation. This assumption is supported by additional results, which are presented below.

We performed calculations for ellipsoidal InAs QDs grown on the (111) GaAs plane within the IE model (see Chapter 5), with subsequent coordinate axes rotation to make the *z*-axis parallel to the [111] direction taken into account. In this case, strain inside the QD is composed of hydrostatic and trigonal components. The total elastic energy density and its components are shown in Figure 6.9(a) as a function of the AR.

Here, results for isotropic and anisotropic elasticity approximations are presented by solid lines and filled circles, respectively. We find that the shear-strain components increase with AR, in a similar way to the case of the (001) plane, [Figure 6.2(a)]. However, we find that it happens essentially not at the expense of the hydrostatic strain. A change in the hydrostatic energy density is not very big; instead,

the total energy density inside the dot significantly increases with AR. This reflects further strain concentration inside the dot with the AR, i.e. redistribution of misfit strain from the matrix to the dot.

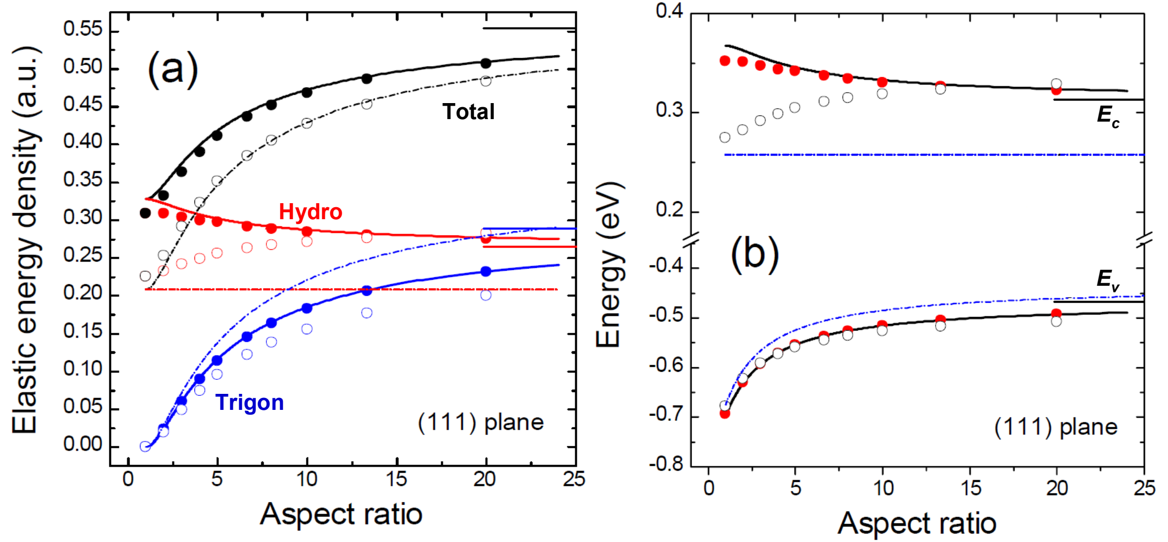

Figure 6.9 : (a) Different elastic energy density components and (b) conduction and valence band-edge positions within the InAs/GaAs (111) ellipsoidal QD as a function of the aspect ratio. Solid lines—as obtained within the IE model; filled symbols—numerical results within cubic elastic anisotropy; dash-dotted lines and open symbols show results within the similar-elasticity approximation for isotropic and anisotropic elastic approximations, respectively. Short solid lines indicate band edges for InAs/GaAs (111) QW.

Strain-induced modification of the band-edge positions is presented in Figure 6.9(b). Note that effects of piezoelectric field are not taken into account here. Hence this result is an approximate because the realistic band profile for (111) plane can be essentially altered by piezoelectric field. Qualitatively, it is similar to the (001) case shown in Figure 6.2(b). However, absolute values of band shift and/or splitting are different. What is the reason for this? The hydrostatic deformation potentials and bulk modulus are isotropic by definition. For the shear deformation potentials, a condition for isotropy is $b\sqrt{3}/d = 1$, [20-22] which roughly holds for most of III-V zinc-blende materials. Therefore, variation of band shift and/or splitting with growth direction originates mainly from the elastic anisotropy which alters the magnitude of strain. This happens because shear elastic modulus, μ_2, comes into play instead of μ_1 for the (111) orientation, as was discussed in Section 4.1.1.2. Typically, μ_2 is twice as large as μ_1. Note that still a good agreement is observed for the (111) plane between the isotropic and anisotropic elasticity approximations.

For arbitrary growth direction, the situation is expected to be intermediate between (001) and (111) cases, with the major effect in strain caused by an effective μ value. We suggest that the ellipsoidal model in the isotropic elasticity approximation still possesses good predictive ability, as long as an appropriate expression for the Lamé coefficients in terms of cubic elastic constants is used, in the spirit of Eq. (4.17). It has also been noted in earlier papers [7,8,23-25] that the isotropic elasticity approximation provides a relatively accurate picture of strain effects in SAQDs.

Such an observation may appear surprising in view of the fundamental elastic anisotropy of cubic III-V materials. The degree of anisotropy can be formally defined by deviation of $(c_{11} - c_{12})/2c_{44}$ from 1. For example, for GaAs $1-(c_{11} - c_{12})/2c_{44} \approx 0.55$. We suggest that a small effect of elastic anisotropy on the strain profile in III-V SAQDs is essentially due to the coincidence of hard (soft) elastic directions in the dot and in the matrix. In that case, the normal force field produced by the lattice misfit at the heterointerface is sustained by a hard (soft) elastic direction in the dot against the hard (soft) direction in the matrix. Thus, anisotropy of individual moduli appears not to be as important as a *difference in anisotropy* between the dot and matrix materials. This difference is often very small. Indeed, the ratio of lattice stiffness along hard [111] and soft [001] directions, which is equal to μ_2/μ_1 , varies weakly between III-V zinc-blende materials.

6.4.2 COMPARISON To The SIMILAR-ELASTICITY APPROXIMATION

Finally, we would like to compare our approach to the Similar-Elasticity (SE) approximation, in which the same elastic constants are assumed for dot and matrix materials. This approximation is typically employed in analytical calculations of the elastic problem for SAQDs.[23-25] First, we note that for isotropic elasticity, the hydrostatic strain is constant and is equal to $e_m\ [(1+\nu)/(1-\nu) - 3]$ in the dot and is zero in the matrix for *any* shape of the dot.[11] Hence, neither of the conduction band energies in the dot nor in the matrix are at all affected by the dot shape. This reveals the most important limitation of the SE approximation. At the same time, variation in the shear strain and therefore in the position of the top valence-band edge is similar to the case of different elastic constants. This is shown in Fig. 6.10; data for the SE approximation were obtained using the elastic constants of the GaAs matrix. However, there is a strong variation in the total strain energy density with the AR. This indicates

that the origin of the increase in the valence-band splitting is different. In this case it is due to further strain concentration in the dot, rather than strain redistribution between different components in the case of different elastic constants.

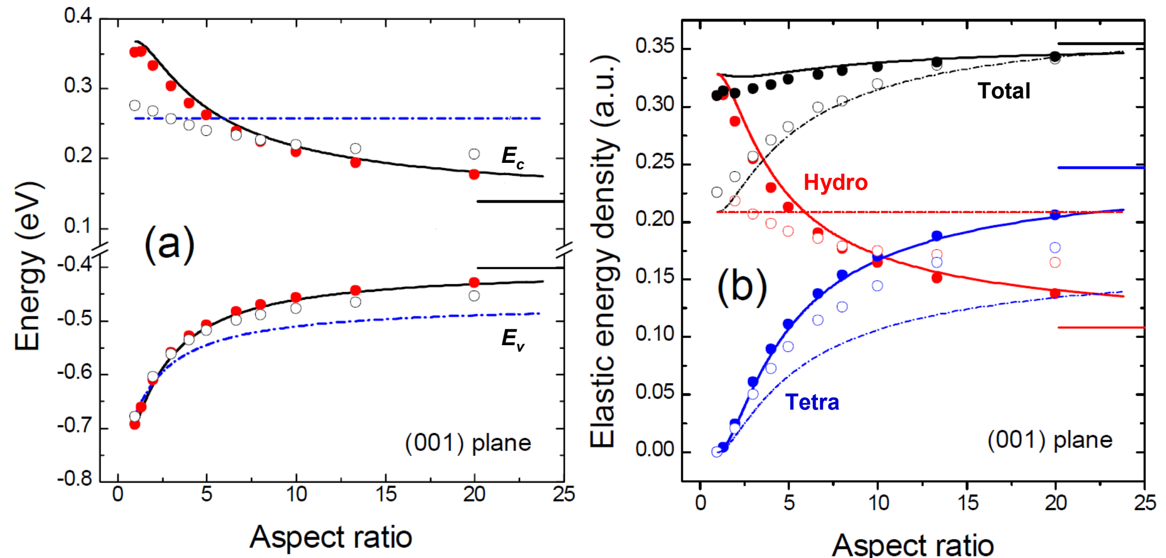

Figure 6.10 : (a) Conduction and valence band-edge positions and (b) different elastic energy density components within the InAs/GaAs (001) ellipsoidal QD as a function of the aspect ratio. Filled symbols-numerical results within cubic elastic anisotropy; solid lines-as obtained within the IE model; dash-dotted lines and open symbols show results within the similar elasticity approximation for isotropic and anisotropic elastic approximations, respectively. Short solid lines indicate band edges for InAs/GaAs (001) QW.

Combination of the Similar-Elasticity approximation with elastic anisotropy introduces some variation of the conduction band edge with the AR. [25] The results of numerical calculations in such an approximation are presented by dash-dot lines and open circles in Figure 6.9 and Figure 6.10 for the (111) and (001) planes, respectively. One can see that for the conduction-band variation as a function of AR, there is qualitative agreement between the two approximations in the case of the (001) plane. However, in case of the (111) plane, an *opposite* trend is observed. Such behaviour reflects variation in the hydrostatic strain component, as depicted in Figures 6.9(b) and 6.10(b).

The comparison demonstrates that the SE approach provides a less accurate approximation as compared to isotropic elasticity, especially for the conduction band. In particular, it predicts a *qualitatively* different strain variation with AR in and around the dot.

6.5 APPLICATION OF ELLIPSOIDAL MODEL

The ellipsoidal model discussed above was applied to several SAQD material combinations in order to determine the systems that would be available for MIR applications. The model allows studies of the combination of both binary and ternary material combinations. The band profiles were calculated for three AR (i.e., 2, 4, and 8) for each of the material combinations. The averaged band edge positions from Ref. [4] were included to facilitate the comparison of the calculated results to the literature results.

As mentioned before, the fundamental objective of the DOMINO project is to create a new class of nano-photonic devices, namely Sb-based quantum dot laser diodes, emitting continuous wave at room temperature in the MIR 3-5 μm wavelength range utilising type-I band alignment. The chosen SAQD system in this project is InSb/GaSb. Another goal of DOMINO project is to retrieve a clear picture of the structural, electronic and optical properties of this SAQD. The investigation starts by studying the InSb/GaSb SAQD system.

It will be shown later that it is not possible to achieve emission in the MIR 3-5 μm (0.25-0.40 eV) emission range from InSb/GaSb SAQD system in theoretical modelling point of view. This is quite a surprising result for this narrow gap InSb-based SAQD.

Further investigation on other type-I SAQD systems has shown that in fact, there are ***no*** appropriate material combinations that would applicable for the MIR 3-5 μm (0.25-0.40 eV) emission range. All of them produce QDs with band gap much larger than the MIR 0.25-0.40 eV range, when type-I band alignment is possible. This has leads to the study of the type-II $InAs_xSb_{(1-x)}$/InAs system and the results are presented in Chapter 7.

6.5.1 InGaSb QD in GaSb MATRIX

This section not only discusses the application of the ellipsoidal model to this particular SAQD with some general description of the band profile calculated, but a detailed discussion on this SAQD will also be presented. The result of the band profile

calculation is presented in Figure 6.11. The result shows that this SAQD system shows type-I band alignment for the whole composition range.

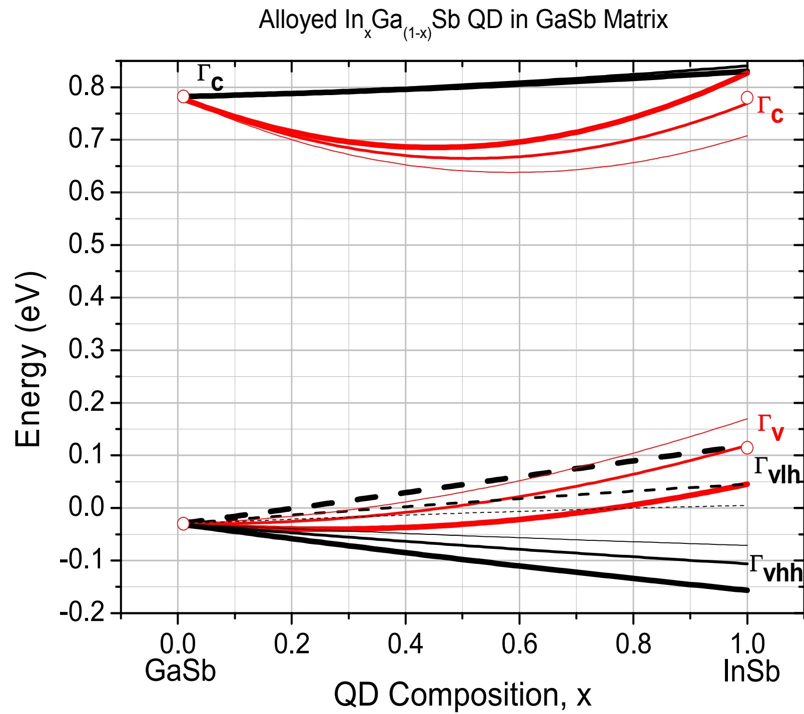

Figure 6.11 : Band alignment for $In_xGa_{(1-x)}Sb$/GaSb SAQD as a function of composition, x. Red line – band edges within the dot. Black line – band edges of the matrix at heterointerface. Thick line – AR=2, Intermediate line – AR=4, and Thin line – AR=8. The circles denote the averaged band edges for lens-shaped similar dot from Ref. [4]

As one can see, the smallest band gap within the dot is ~550 meV for the InSb/GaSb dot of AR = 8. The band gap is even larger for the lower ARs. These values are far from the targeted MIR 3-5 μm optical range. Note that only the top of valence band within the dot is shown, while both light- and heavy-hole valence bands at the heterointerface are shown for the matrix. This is to facilitate the 'shell' feature observed for low AR dots discussed in Section 6.2.2 for InAs/GaAs SAQD. This 'shell' feature is more pronounced for the $In_xGa_{(1-x)}Sb$/GaSb SAQD system because the valence band offset for this system is only ~30 meV.

In this section, the results from the electronic structure modelling will be presented. The same trend as for InAs/GaAs system in the previous chapter has been studied. The purpose is two-fold; first, to present the detailed study of the electronic structure of the heterostructures and second to facilitate the applicability of the method used in performing the modelling. After that, the optical properties of high density, uniform and fully strained InSb/GaSb grown under alternative conditions, which were

established in University of Montpellier II, will be presented. Under this alternative growth procedure, a dot density of 7.4x10^{10} cm^{-2} and a narrow monomodal distribution are obtained with the ground state PL emission peak at 0.36 eV (3.45 μm).

6.5.1.1 STRAIN AND STRAIN-MODIFIED BAND PROFILE

In this section, we analyse the strain distribution and the strain-modified band profile of InSb/GaSb SAQDs similar to that for InAs/GaAs system. We also start by examining the elastic strain energy density and the strain distribution of the ellipsoidal dot. Figure 6.12(a) shows the spatial distribution of the total elastic energy density for several aspect ratios obtained from numerical modelling in two-dimensional cross sections. Figure 6.12(b) shows spatial distribution of the hydrostatic component of the strain energy density. The (100) plane is on the left and the (-110) plane is on the right.

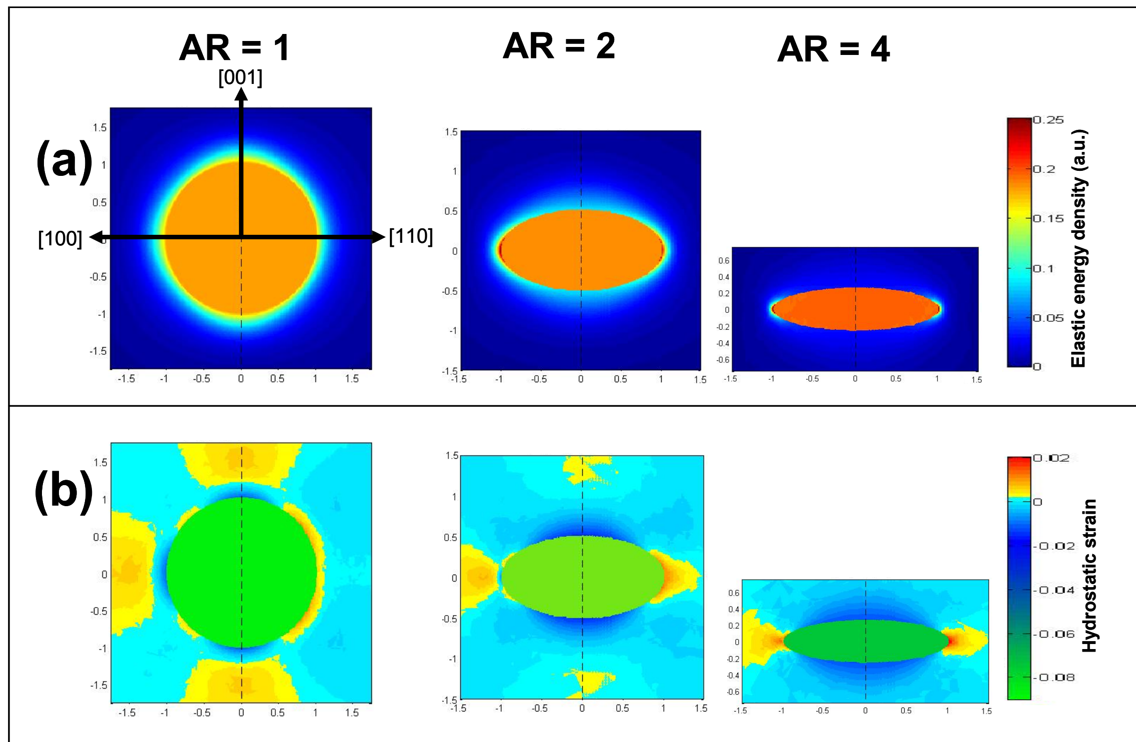

Figure 6.12: (a) Spatial distribution of total strain energy density, (b) Spatial distribution of hydrostatic strain component; inside and around InSb/GaSb (001) ellipsoidal QD for different aspect ratios. Each graph shows (-100) and (110) cross-section planes through the dot centre on the left- and right-hand-side parts, respectively.

As one can see, the same general trends in strain variation with the AR were identified similar to that of InAs/GaAs system. Because of this, we would expect such trends to be common for a wide range of III-V materials, in view of the same symmetry of elastic moduli and deformation potentials.

Figure 6.13 shows the strain-modified band profile for a spherical InSb/GaSb SAQD. The conduction band within the dot shifts to higher energy. This illustrates the dominant effect of the hydrostatic strain, which is an increase in the direct band gap. As a result, the band gap of the dot is increased beyond the 3-5 μm (0.25-0.40 eV) emission range.

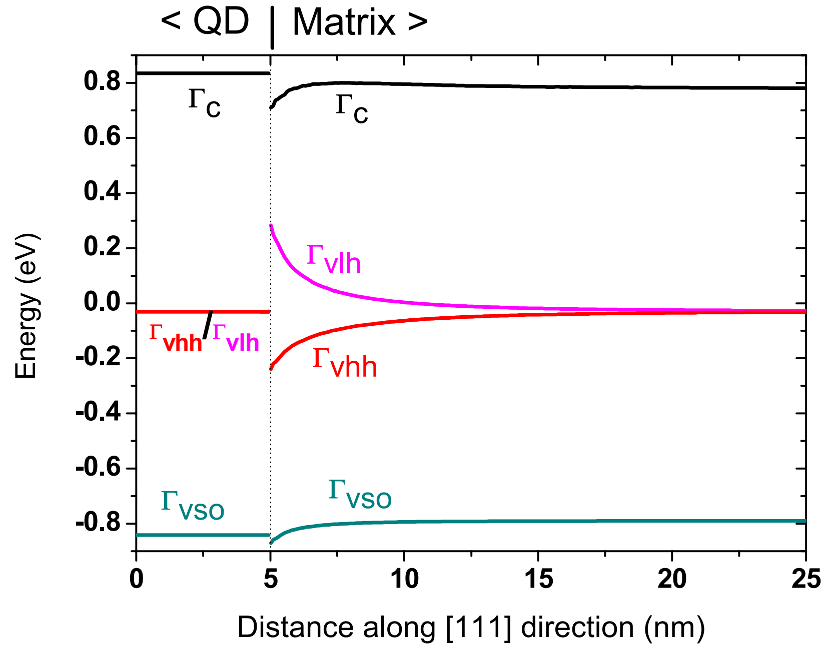

Figure 6.13 : Strain-modified band profile for spherical InSb/GaSb SAQD along [111] direction. Black line – conduction band; red line – heavy-hole band; magenta line – light-hole band; green line – split-off band.

Inside the dot, the valence bands are still degenerate, as shown in Figure 6.13. However, the valence bands are split into light- and heavy-hole bands in the GaSb matrix near the heterointerface due to the presence of the shear strain. The splitting of the valence bands resulting in deeper confinement for heavy holes to ~200 meV. On the other hand, the light-hole band in the matrix near the heterointerface is higher in energy as compared to both the heavy- and light-hole bands in the dot due to the upward band bending of the light-hole band at the interface.

The two-dimensional cross-section plots have been plotted in Figure 6.14 in order to show the detailed picture of the strain-modified band profiles for InSb/GaSb SAQDs. The cross-section plots present the (100)-plane on the left and (-110)-plane on the right for ellipsoid-, truncated cone-, lens-, and square base pyramid-shaped SAQDs. Figure 6.14 (a) shows the Γ-valley conduction band profile. As shown in Figure 6.14 (a),

the average Γ-valley conduction band energies in the dot and in the matrix are close to each other for the dots of lower ARs (see also Figure 6.13). As the AR is increased, the Γ-valley conduction band within the dot decreases in energy. This is because the hydrostatic strain drops with increasing AR.

The effect of increasing AR on the valence bands profile is much stronger; it is not only causing the energy shift but also the splitting of the valence band into heavy- and light-hole bands within the dot as well as in the matrix. The heavy-hole band is shown in Figure 6.14(b). For ellipsoidal dots, the energy within the dot is constant. As the AR is increased, the heavy-hole band within the dot moves up in energy, forming a deeper confinement for the holes. The increase in the confinement energy is as large as ≈ 250 meV when the AR changes from 1 to 8. One can also note that there are darker blue areas in the matrix near the interface, which are lower in energy than that in matrix away from the dot. This is due to the downward band bending, which increases the heavy-hole confinement even further.

The light-hole band profile is shown in Figure 6.14(c). Again, homogeneous colour distribution within the ellipsoidal dot indicates constant energy. By comparing Fig. 6.14(b) and 6.14(c), one can see that the light-hole band is much lower in energy within the dot. In addition, the band edge energy near the interface is *higher* than in the matrix away from the dot. This is due to the upward light-hole band bending near the interface. Such a bending generates some "shell" around the dot as discussed in the previous chapter.

The effect of this "shell" feature is more prominent for the dots of lower ARs as shown in Figure 6.15. This is because, the confinement potential for both light and heavy holes within the dot are much shallower than that of the light holes in the matrix. As a result, the holes tend to localisation in this "shell" feature. The unstrained valence band offset for InSb/GaSb SAQDs heterostructure is very small (i.e., ~30 meV), hence the tendency of the hole localisation in this "shell" feature is higher as the hole confinement potential in the dot is much lower in InSb/GaSb SAQDs as compared to InAs/GaAs system.

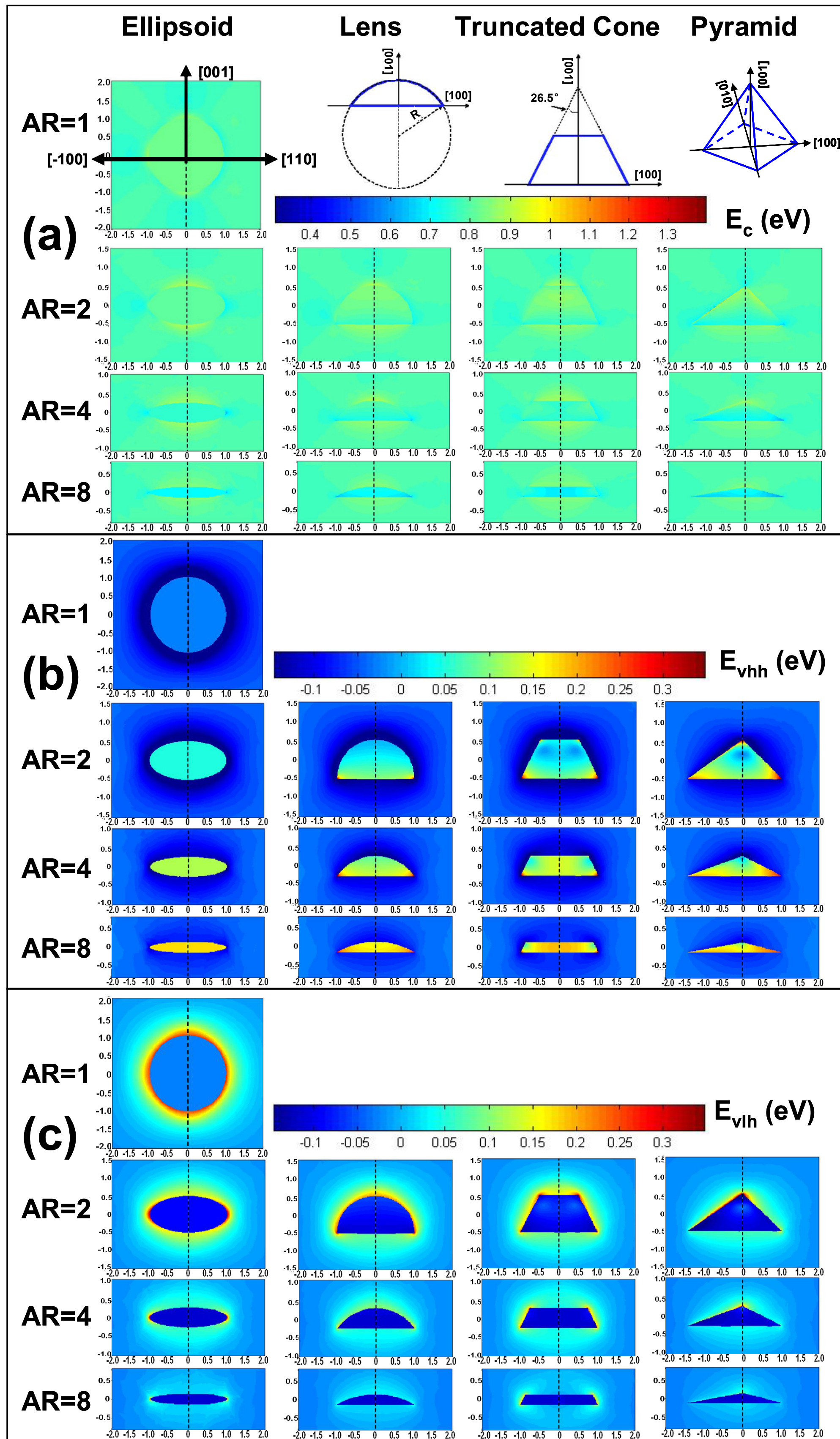

Figure 6.14 : Band profile for several aspect ratios for isolated InSb/GaSb (001) SAQDs of different shapes. Each graph shows (100) and (−110) cross-section planes through the dot centre on the left- and right-hand-side parts, respectively: (a) conduction band, (b) heavy-hole valence band, and (c) light-hole valence band. Inserts illustrate the parental geometry details for the QDs.

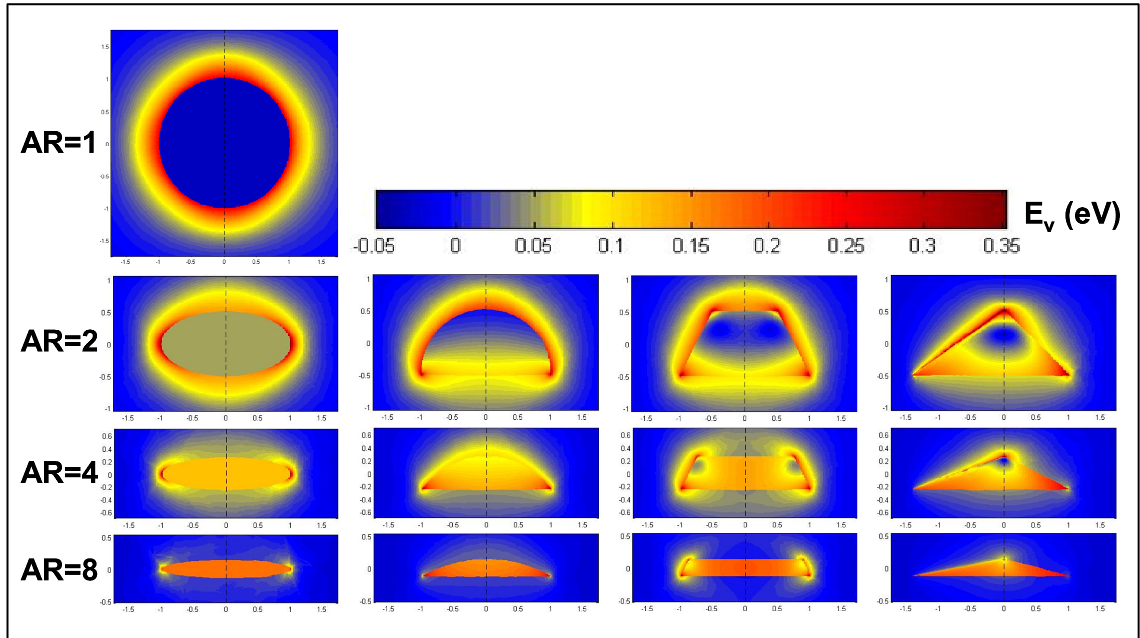

Figure 6.15 : Top valence band for several aspect ratios for isolated InSb/GaSb (001) QDs of different shapes. Each graph shows (100) and (−110) cross-section planes through the dot centre on the left- and right-hand-side parts, respectively.

The energy values of the band edges strain energy density components averaged over the QD volume are presented in Figure 6.16(a) and 6.16(b), respectively. These *averaged* values as a function of the AR similar to that of Figure 6.5 in the previous section. One can see not only that all values are close to each other for a given AR and follow that of the ellipsoidal dot; also the conduction (valence) band edge within the dot of all shapes shows a clear tendency to decrease (increase) with AR. This means that the band-edge energies are not so sensitive to shape details and the band gap within the dot is reduces with increasing AR. This phenomenon is due to the redistribution of the strain energy density components as presented in Fig. 6.16(b).

The hydrostatic and tetragonal strains are the dominant components except for very low AR. Enhancement in the tetragonal component at the expense of the hydrostatic one is also a major effect of the increased AR. At lowest ARs, however, the trigonal and orthorhombic components are the most prominent shear components of the strain energy. As one can see from Figure 6.16(b), the hydrostatic (shear tetragonal) component of the strain energy density drops (increases) with increasing AR. The drop in hydrostatic component reduces the conduction band shift while the increase in tetragonal component results in stronger valence band splitting and hence shifting the

valence band maxima to higher energy. As a result, the band gap within the dot decreases with increasing AR.

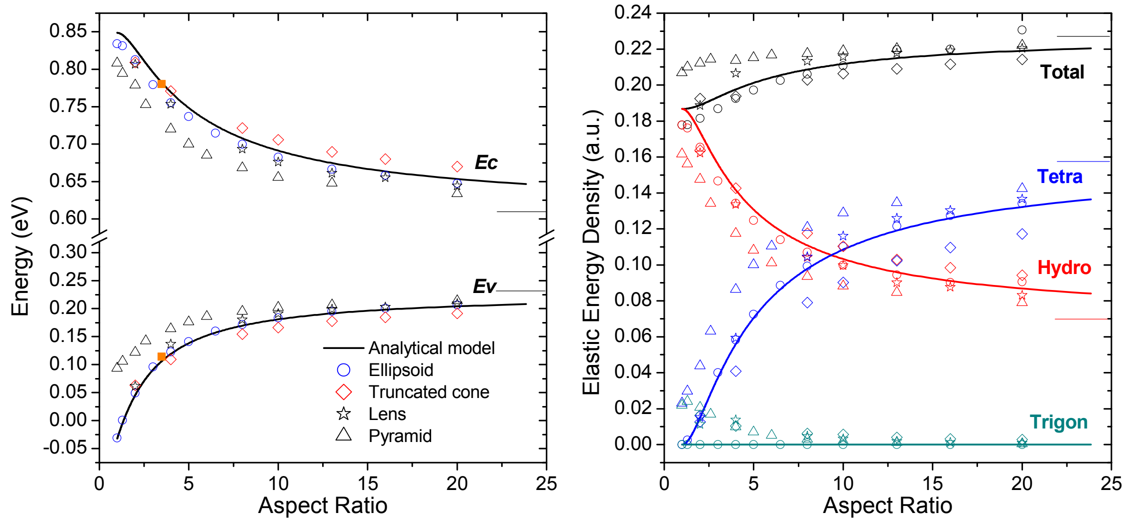

Figure 6.16 : (a) Conduction and upper valence band edges within InSb/GaSb (001) QDs as a function of aspect ratio: open symbols—averaged numerical results for cubic elastic anisotropy approximation for different QD shapes: circles—ellipsoid, triangles—pyramidal, diamonds—cone, stars—lens, and filled square symbols show the results from Ref. 4. Solid lines present analytical results obtained within the IE model for the ellipsoidal shape. (b) Elastic energy density within the InSb/GaSb (001) QD as a function of the aspect ratio. Symbols display averaged values of different components of the elastic energy obtained from numerical calculations. Solid lines represent the elastic energy density components for the ellipsoidal QD as obtained within the IE model. Short solid lines indicate values of the energy density components for an InAs/GaAs (001) quantum well.

6.5.1.2 ELECTRON/HOLE LEVELS

After examining the strain distribution and the resulting confinement potential, we proceed to examining the single-particle electron and hole states which take into account the size-quantisation. In this calculation, we assumed the dot base size of 25 nm and the height of 4 nm close to the averaged strained dot reported in the literature [26-31]. We have modelled the electronic states only for the ellipsoidal dot because from the calculated band profile, we expect the effect of shape to be insignificant. The calculated transition energy is in good agreement to the reported experimental results [26-31].

6.5.1.3 OPTICAL PROPERTIES

The investigation of the QD optical properties was carried out by means of PL measurements. The PL measurements were performed by employing lock-in amplification technique in a variable-temperature closed-cycle LN2 cryostat under the excitation of a 785 nm diode laser. The luminescence spectra were detected by a FTIR spectrometer with a potassium bromide (KBr) beam splitter and a liquid nitrogen cooled InSb photodetector. The measurements are performed at 77K and 300K by using 90 mW excitation power and the spectra are shown in Figure 6.17. Due to the low intensity of the PL signal, the spectra appear to be quite noisy.

In the high energy region, two peaks are found at 0.805 eV and at 0.735 eV. The 0.805 eV line is due to the emission from GaSb matrix while the emission line at 0.735 eV is related to the Γ-band transition from the dot similar to that reported in literature. There are two more transitions at low energy being observed at 0.370 eV and 0.490 eV. Hence, the objective to obtain emission in the 3-5 µm range is achieved. However, according to the band structure calculation, the occurrences of these two transitions are not possible. Although the existence of mid-gap defects is not unusual from the growth of SAQDs; however, it would be unusual to have such defects optically active and the TEM investigations have shown that the QD sample is free from defects and dislocations. Therefore, the observation of the 0.370 eV and 0.490 eV emission lines could be linked to the emission from the dot.

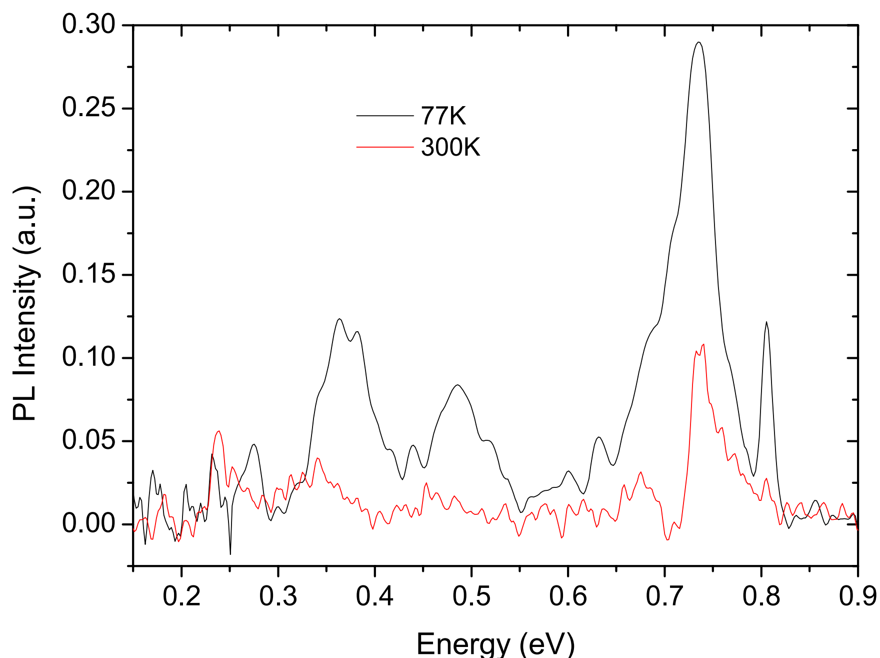

Figure 6.17 : PL spectra of the InSb/GaSb SAQDs at 77K.

The PL signal can be detected on this sample up to room temperature. Both the lower energy peaks shift down to lower energy due to the energy gap reduction with temperature and the intensity decreases by only a factor of 4. This is a very interesting result, because it suggests a good thermal stability. Moreover, the energy separation between the two QD-related peaks does not change with the temperature while their intensity ratio changes, thus suggesting again a thermal activation process of the carriers from the ground state to the excited state. A careful and detailed study as a function of power density and temperature in a wider range is clearly needed. However, these studies are not feasible due to the low intensity of the signal. A long scanning time is needed to obtain good spectra and overheating of the sample is unavoidable when using high excitation power. Hence the reliability of the results will be affected by this heating effect.

6.5.1.4 L-BAND RELATED TRANSITIONS in InSb/GaSb SAQD HETEROSTRUCTURE

From the discussion in the previous section, we note that there is a huge discrepancy between the experimental and theoretical modelling results. So far, the electronic structure modelling considered only the effect of misfit strain on the lowest conduction band and highest valence band edges, which are ground states in the unstrained materials. However, the strain-induced shifting of the band edges may be larger than the energy gap between conduction bands of different symmetry (i.e., *Γ*-, *L*- or *X*-valleys), and resulting in the crossover between them. The crossover could cause the symmetry of the ground electron level in SAQDs being different to the unstrained materials. And this would dramatically affect the optical properties of the SAQDs.

GaSb has a gap between its *Γ*- and *L*-valley conduction bands of only ~60 meV [9]. It has been experimentally established that the *Γ*- to *L*- crossover in bulk GaSb can be obtained with the rhombohedral strain of as small as 0.25% [32]. Compared to the misfit strain in InSb/GaSb SAQD system of ~6%, one would expect the strong *Γ*- to *L*- crossover in GaSb matrix. The conduction band crossover induced by the misfit strain in InSb/GaSb SAQDs has been reported by *Rybchenko et. al.* [33]. The authors have deduced that both the emission at 0.37 eV and 0.49 eV are attributed to the ground state and excited state from indirect transitions between the electrons localised in the *L*-band pockets and the holes that localised in the matrix near the heterointerface.

Therefore, both the emissions at 0.37 eV and 0.49 eV are not only indirect in the real-space but also in the *k*-space.

6.5.2 InAsSb QD in InP Matrix

The band alignment for $InAs_{(1-x)}Sb_x$/InP system is presented in Figure 6.20. The result shows that $InAs_{(1-x)}Sb_x$/InP QDs exhibit type-I band alignment for a broad composition range, as long as the dot is not very round.

The band gap values could be as small as ~400 meV for x=0.5 at AR=8. The deep electron/hole localisation in this QD system may result in higher quantisation energy.

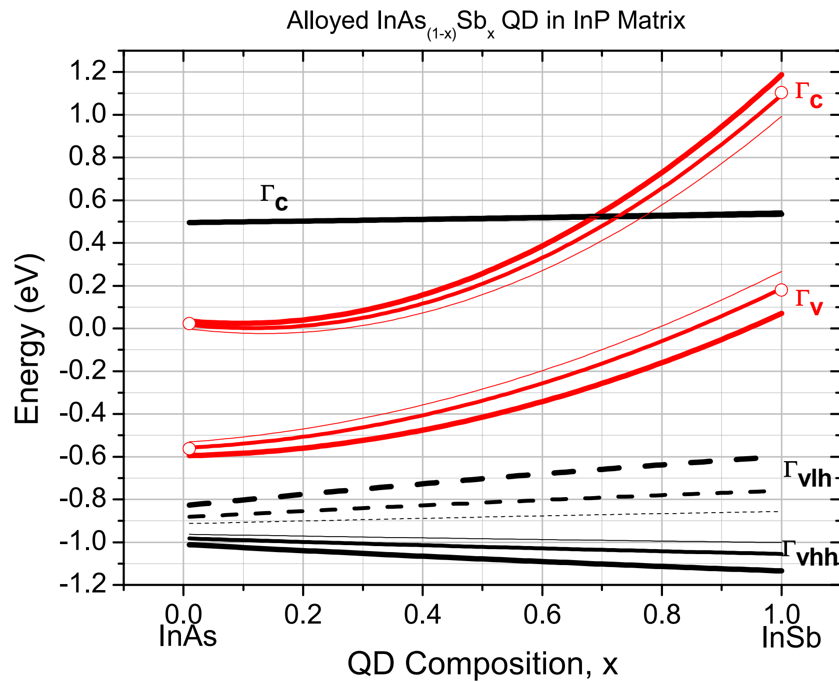

Figure 6.20 : Band alignment for $InAs_{(1-x)}Sb$/InP SAQD as a function of composition, x. Red line – band edges within the dot. Black line – band edges of the matrix at heterointerface. Thick line – AR=2, Intermediate line – AR=4, and Thin line – AR=8. The circles denote the averaged band edges for lens-shaped similar dot from Ref. [4]

6.5.3 InAsSb QD in InAs Matrix

The consideration above shows that the possibility of type-I band alignment with optical transitions tuneable across the MIR optical range is strongly limited for the traditional SAQDs obtained from compressively strained overlayer via SK growth mode. The type-II alignment could be utilised similar to that of W-type quantum well structures

[34]. But the quantum efficiency for this case will be reduced. The band alignment for type-II $InAs_{(1-x)}Sb_x/InAs$ system is presented in Figure 6.21. Detailed discussion about this SAQD system will be presented in Chapter 7.

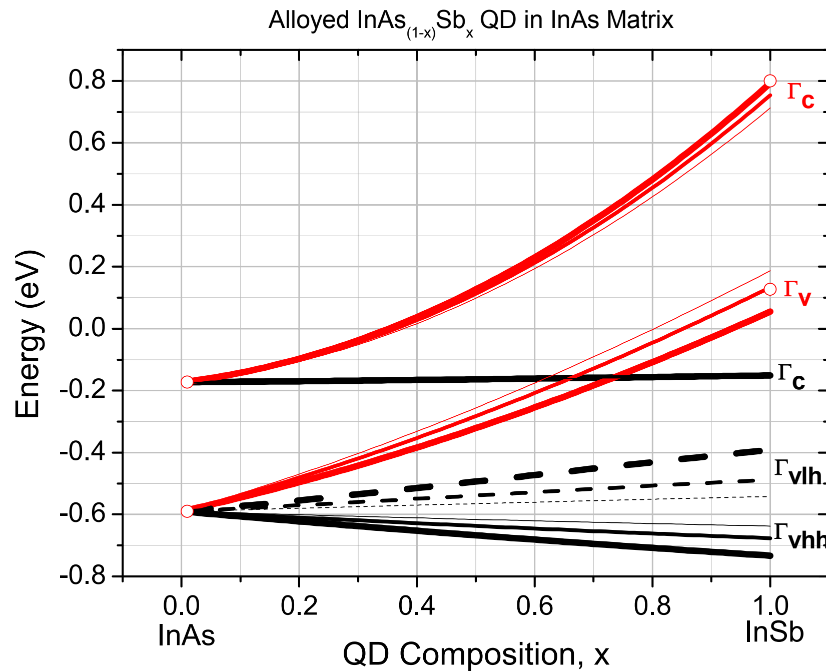

Figure 6.21 : Band alignment for $InAs_{(1-x)}Sb_x/InAs$ SAQD as a function of composition, x. Red line – band edges within the dot. Black line – band edges of the matrix at heterointerface. Thick line – AR=2, Intermediate line – AR=4, and Thin line – AR=8. The circles denote the averaged band edges for lens-shaped similar dot from Ref. [4]

6.6 SUMMARY

We have examined the effect of the quantum-dot shape on the strain-modified quantisation potential. For this purpose, the band profile was calculated for the InAs/GaAs and InSb/GaSb (100) system for a number of realistic dot shapes. The most important features of the quantisation potential were analysed, and their variation with the dot geometry was examined. The underlying variations in the characteristic strain components within the QD were revealed. As a result, the aspect ratio was suggested as a governing geometric parameter of the QD shape. This was used to justify approximation of the QD shape by an ellipsoid, which is expected to be valid for a wide range of III-V zinc-blende SAQD systems. Effects from incorporation of the wetting layer and from the growth plane orientation have been also analysed.

For the ellipsoidal shape, reproducibility of the quantisation potential was analysed using different approximations for the elastic problem. It was shown that most

essential features of the quantisation potential are well reproduced in the isotropic elasticity approximation, provided the effective elastic moduli are selected according to orientation of the growth plane. This result is particularly important because the isotropic approximation allows a simple analytical solution of the elastic problem for an ellipsoidal QD. On the other hand, it was shown that further simplification of the elastic problem (such as the Similar-Elasticity approximation) results in a strain profile which is different both qualitatively and quantitatively. As a result, it reproduces the quantisation potential with significant distortion.

Incorporation of the WL does not produce any essential modifications provided the thickness of the WL is much lower than the dot height.

From the analysis of the strain-modified band profile for a range of III-V compound semiconductors with zinc-blende structure shows that there are ***no*** appropriate material combinations that would applicable for the MIR emission range. All of them produce QDs with band gap much larger than the MIR 0.25-0.40 eV range, when type-I band alignment is possible.

References:

[1] D. Bimberg, M. Grundmann, and N. N. Ledentsov, *Quantum Dot Heterostructures* (Wiley, Chichester, 1999)

[2] B. A. Joyce, P. C. Kelires, A. G. Naumovets, and D. D. Vvedensky, eds., *Quantum Dots: Fundamentals, Applications and Frontiers*, (Amsterdam: Springer, 2005).

[3] I. Vurgaftman, J. R. Meyer, and L. R. Ram-Mohan, J. Appl. Phys. **89**, 5815 (2001).

[4] C. Pryor and M. E. Pistol, Phys. Rev. B **72**, 205311 (2005)

[5] M. Korkusinski, P. Hawrylak, Phys. Rev. B **63**, 195311 (2001)

[6] M. Tadic, F. M. Peeters, and K. L. Janssens, Phys. Rev. B **65**, 165333 (2002).

[7] M. Grundmann, O. Stier, D. Bimberg, Phys. Rev. B **52**,11969 (1995).

[8] C. Pryor, Phys. Rev. B **57**, 7190 (1998).

[9] A. Wojs, P. Hawrylak, S. Fafard, L. Jasak, Phys. Rev B **54**, 5604 (1996).

[10] H. Shin, Y.-H. Yoo, and W. Lee, J. Phys. D: Appl. Phys. **36**, 2612 (2003).

[11] W. Lee, J. -M. Myong, Y. -H. Yoo, and H. Shin, Solid State Commun. **132**, 135 (2004).

[12] L. He, G. Bester, and A. Zunger, Phys. Rev. B **70**, 235316 (2004).

[13] M. A. Cusack, P. R. Briddon, and M. Jaros, Phys. Rev.B **56**, 4047 (1997).

[14] J. Kim, L.-W. Wang, and A. Zunger, Phys. Rev. B **57**, R9408 (1998).

[15] C. Pryor, Phys. Rev. B **60**, 2869 (1999).

[16] A. J. Williamson, A. Zunger, Phys. Rev. B **59**, 15819 (1999).

[17] P. W. Fry, I. E. Itskevich, D. J. Mowbray, M. S. Skolnick, J. J. Finley, J. A. Barker, E. P. O'Reilly, L. R. Wilson, I. A. Larkin, P. A. Maksym, M. Hopkinson, M. Al-Khafaji, J. P. R. David, A. G. Cullis, G. Hill, and J. C. Clark, Phys. Rev. Lett. **84,** 733 (2000).

[18] P. W. Fry, I. E. Itskevich, S. R. Parnell, J. J. Finley, L. R. Wilson, K. L. Schumacher, D. J. Mowbray, M. S. Skolnick, M. Al-Khafaji, A. G. Cullis, M. Hopkinson, J. C. Clark, and G. Hill, Phys. Rev. B **62**, 16784 (2000).

[19] S. Lee, O. L. Lazarenkova, P. von Allmen, F. Oyafuso, and G. Klimeck, Phys. Rev. B **70**,125307 (2004).

[20] F. H. Pollak, M. Cardona, Phys. Rev. **172**, 816 (1968).

[21] Su-Huai Wei and A. Zunger. Phys. Rev.B **49**, 14337 (1994).

[22] G. E. Pikus and G. L. Bir, Soviet Phys. Solid State **1**, 136 (1959); *ibid* **1**, 1502 (1959); *ibid* **3**,730 (1961).

[23] J. R. Downes, D. A. Faux, and E. P. O'Reilly, J. Appl. Phys. **81**, 6700 (1997); D. A. Faux, J. R. Downes, and E. P. O'Reilly, J. Appl. Phys. **80**, 2515 (1996); *ibid* **82**, 3754 (1997).

[24] J. H. Davies, J. Appl. Phys. **84**, 1358 (1998).

[25] A. D. Andreev, J. R. Downes, D. A. Faux, and E. P. O'Reilly, J. Appl. Phys. **86**, 297 (1999).

[26] A. F. Tsarsul'nikov, N. N. Ledentsov, M. V. Maksimov, B. Ya. Mel'tser, P. V. Neklyudov, S. V. Shaposhnikov, B. V. Volovik, I. L. Krestnikov, A. V. Sakharov, N. A. Bert, P. S. Kop'ev, Zh. I. Alferov, and D. Bimberg, Semiconductors **31**, 55 (1996).

[27] A. F. Tsarsul'nikov, S. V. Ivanov, P. S. Kop'ev, A. K. Kryganovskii, N. N. Ledentsov, M. V. Maksimov, B. Ya. Mel'tser, P. V. Nekludov, A. A. Suvorova, A. N. Titkov, B. V. Volovik, M. Grundmann, D. Bimberg, and Zh. I. Alferov, J. Elect. Materials **27**, 414 (1998).

[28] E. Alphandéry, R. J. Nicholas, N. J. Mason, B. Zhang, P. Möck, and G. R. Booker, Appl. Phys. Lett. **74**, 2041 (2001).

[29] P. Möck, G. R. Booker, N. J. Mason, R. J. Nicholas, E. Alphandéry, T. Topuria, and N. D. Browning, Mat. Sci. Eng. **B80**, 112 (2001).

[30] E. Alphandéry, R. J. Nicholas, N. J. Mason, S. G. Lyapin, and P. C. Klipstein, Phys. Rev. B **65**, 115322 (2002).

[31] P. A. Shields, C. W. Bumby, L. J. Li, and R. J. Nicholas, J. Appl. Phys. **96**, 2725 (2004).

[32] R. A. Noack, Phys. Stat. Sol. (b) **90**, 615 (1978).

[33] S. I. Rybchenko, R. Gupta, K. T. Lai, I. E. Itskevich, S. K. Haywood, V. Tasco, N. Deguffroy, A. N. Baranov, and E. Tournié, Phys. Rev. B **76**, 193309 (2007).

[34] J. R. Meyer, C. A. Hoffman, F. J. Bartoli, and L. R. Ram-Mohan, Appl. Phys. Lett. **67**, 757 (1995).

CHAPTER 7

STRAINED TYPE-II $InAs_xSb_{1-x}$/InAs SAQDs FOR THE MIR

7.0 INTRODUCTION

It has been shown in the previous chapter and by band-structure modelling in the literature [1-3] that the direct band gap in type-I InSb-based SAQDs increases beyond the 3-5 μm range due to the misfit compressive strain. Hence, for use in the MIR-range devices, alternative SAQD designs need to be considered.

SAQDs with type-II band alignment offer the possibility of optical transitions within the MIR range (albeit with lower quantum efficiency than type-I systems), similar to W-type quantum-well structures. [4] In particular this can be realized for the InSb/InAs SAQD system with an expected type-II broken gap band alignment. Recently, successful growth of InSb/InAs QDs has been reported, [5-7] with intense photoluminescence (PL) in the 3.9-4.3 μm wavelength range. However, measurement of structural parameters for these dots such as composition, size and shape is very difficult because of their small size (2.5-3 nm). Therefore, it is important to be able to evaluate these parameters from the investigation of the electronic structure by optical and transport methods. Because of that, theoretical analysis of the effect of the structural parameters on the electronic and optical properties is crucial.

In this chapter, the results of the modelling of electronic and optical properties of $InAs_xSb_{(1-x)}$/InAs SAQDs are presented, focusing on the effects of SAQD morphology and composition. In particular, the electronic structure of $InAs_xSb_{(1-x)}$/InAs SAQD of various shapes, aspect ratios and compositions are analysed. A method of assessing the geometry and composition of $InAs_xSb_{(1-x)}$/InAs quantum dots using their optical spectra and limited microscopy information is suggested.

The actual shape of $InAs_xSb_{(1-x)}$/InAs SAQDs is unknown. However, it has been shown earlier in Chapter 6 that the governing geometric parameter of a SAQD is the aspect ratio (AR), as defined in Figure 7.1. In particular, we have shown that the

approximation using a simple ellipsoidal shape is sufficient to reveal the major features of the electronic structure of the dots. In this chapter, two shapes: an oblate ellipsoidal and a lens are examined. The only variable parameter for both shapes is the AR. The most important effects of the dot structure on the electronic properties for the ellipsoidal shape are examined and then the analysis for the lens shape is performed for comparison.

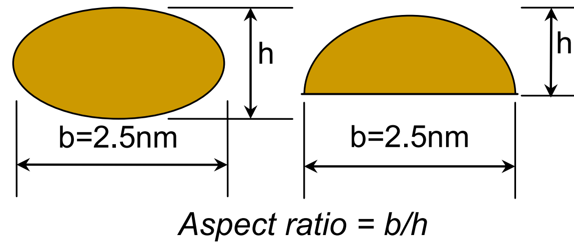

Figure 7.1: Definition of the aspect ratio AR.

The existence of developed wetting layer in the $InAs_xSb_{1-x}$/InAs SAQD system is still doubtful [7]; because of this, the wetting layer is excluded in this modelling. The piezoelectric potential is not included either, because it is expected to be negligible for the dot sizes considered. The material parameters were taken from Ref. [8], which are listed in Table 4.1 (Chapter 4). Also following Ref. [8], all energy values are given with respect to the valence band edge in unstrained InSb.

The modelling is started by obtaining the strain distribution in the dot and the surrounding matrix in the continuum-elasticity approximation. Both the cubic anisotropy and different elastic constants for the dot and matrix materials are taken into account. The finite element method (FEM) employing commercial Comsol Multiphysics software is used.

7.1 STRAIN AND STRAIN MODIFIED BAND PROFILE

In this section, the strain distribution and the resulting confinement potential are analysed for ellipsoid- and lens-shaped $InAs_xSb_{(1-x)}$/InAs SAQDs of various ARs and compositions. We start by examining the simplest example of a spherical dot (i.e. ellipsoid of AR=1). Next, the effect of increasing AR is examined and compared with similar calculations for the more complicated lens shape. Note that for both shapes, the strain distribution and the confinement potential are size-independent within the approximation used.

The strain within the spherical dot is purely hydrostatic and homogeneous. Hence, the positions of the edges of conduction and valence bands in the dot are well defined. Meanwhile, there is a shear component of strain present in the matrix, which is largest at the dot-matrix interface.

Figure 7.2(a) shows the unstrained band profile (i.e. if we could somehow turn off the strain) for a spherical InSb/InAs QD. It demonstrates a type-II broken-gap band alignment with a confinement energy of ≈ 600 meV for degenerate valence bands. Figure 7.2(b) shows how the band profile is modified by strain. As one can see, the type-II broken-gap band alignment still holds but the band profile changes considerably. The conduction band edge in the dot shifts to higher energy. This illustrates the dominant effect of the hydrostatic strain, which is an increase in the direct band gap. In addition, shallow potential wells for electrons in the InAs matrix arise close to the interface (marked by dashed ellipses in Figure 7.2(b)). This occurs due to the band bending, which does not exist in the unstrained band profile.

Inside a spherical SAQD, the valence bands are still degenerate. However, shear strain splits the valence bands in the matrix into heavy- and light-hole bands. One can see that strong confinement exists for both heavy- and light-holes. However, due to band bending that has opposite sign for heavy holes and light holes, the confinement potential for heavy holes increases to ≈ 800 meV. Meanwhile, the confinement for light holes varies into the matrix to a maximum value of 600 meV (i.e., the value for the unstrained profile).

A more detailed picture of the strain-modified band profiles can be obtained using two-dimensional cross-section plots. Figure 7.3 shows these colour plots of the band profiles for InSb/InAs SAQDs of ellipsoidal and lens shapes for several ARs. Profiles for the conduction band and the heavy- and light-hole valence bands are shown. Each colour plot presents the (100) plane on the left and the (-110) plane on the right. The colour scale indicates the energy levels in eV. Note that the colour scale is the same for heavy- and light-hole bands but it is different for the conduction band.

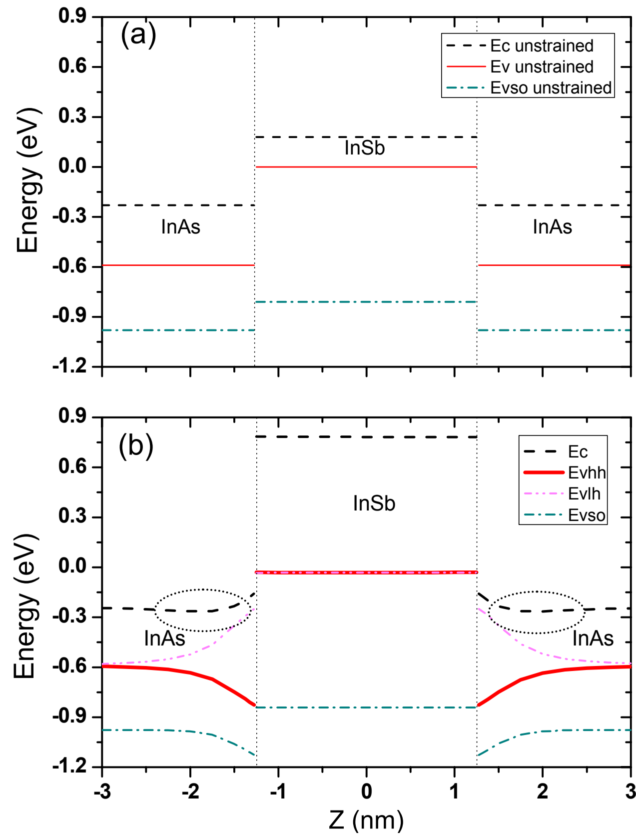

Figure 7.2 : Band profile for spherical InSb/InAs QD along [001] (growth) direction at 80K: unstrained (a), strain-modified (b). Black dashed line – conduction band; thin red solid line – degenerate valence band; thick red solid line – heavy-hole band; magenta dash-dot-dot line – light-hole band; green dash dot line – split-off band. Two dotted ellipses indicate areas of shallow confinement for electrons.

Figure 7.3(a) shows the profile for the conduction band. Homogeneous colour within the ellipsoidal dots indicates constant energy. (The energy varies slightly within the lens-shape dots). In the matrix, one can see darker blue areas which are most prominent in the (100) plane and for lower ARs. These areas of very shallow confinement potential, which are highlighted by the dotted ellipses in Figure 7.2, provide only weak confinement for the electrons. Otherwise, the effects of the shape and AR on the conduction band are minor. The same is true for other possible dot shapes such as the truncated cone or pyramid as it has been shown in Chapter 6.

The effect of shape and AR on the heavy-hole band profile is much stronger as can be seen in Figure 7.3(b). For ellipsoidal dots, the energy within the dot is constant. As the AR is increased, the heavy-hole band within the dot moves up in energy, forming a deeper confinement for the holes. The increase in the confinement energy is as large as ≈ 200 meV when the AR changes from 1 to 8. One can also note that there are darker

blue areas in the matrix near the interface, which are lower in energy than in the matrix away from the dot. This is due to the downward band bending, which increases the heavy-hole confinement even further. This feature is discussed in more detail later.

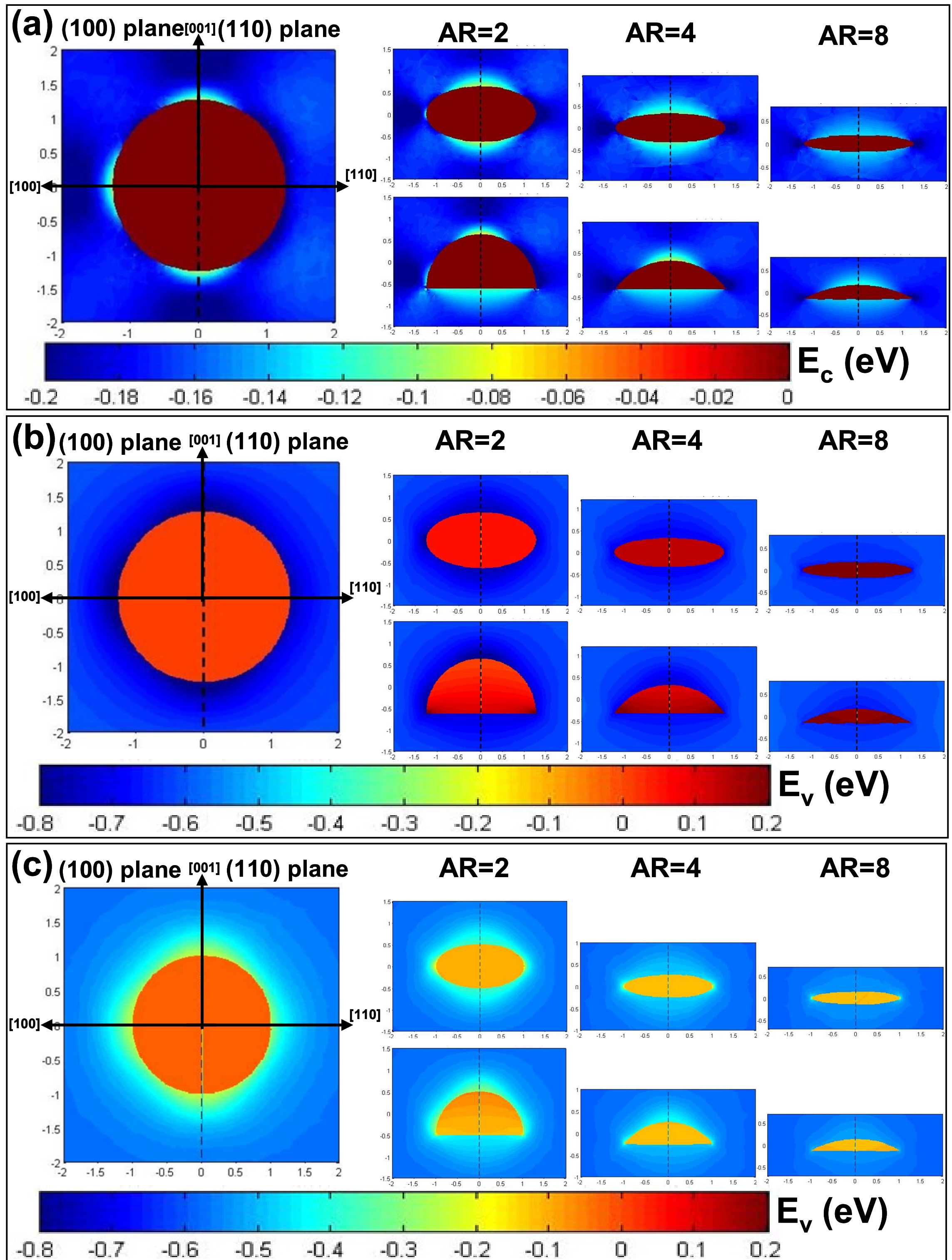

Figure 7.3 : Strain-modified band profile for InSb/InAs QDs of ellipsoidal and lens shapes for several aspect ratio. Each graph shows (100) and (-110) cross-section planes through the dot centre on the left- and right-hand-side parts, respectively. (a) conduction band; (b) heavy-hole band; (c) light-hole band.

The light-hole band profile is shown in Figure 7.3(c). Again, homogeneous colour distribution within the ellipsoidal dot indicates constant energy. By comparing Figure 7.3(b) and 7.3(c), one can see that the light-hole band is much lower in energy within the dot. In addition, the band edge energy near the interface is *higher* than in the matrix away from the dot. This is due to the upward light-hole band bending near the interface. Because of that, the confinement potential for light holes is much shallower than that for the heavy holes. Also, note that the light-hole band profile does not change significantly with increasing AR.

The main difference in the strain distribution between the ellipsoidal and lens shapes is that in the latter case, the strain is inhomogeneous across the dot. This results in a varying band profile across the dot. It is worth noting that the band edge is at the highest energy at the base of the dot for heavy holes and at the top of the dot for light holes. However, the overall variation in strain and hence in the band profile is relatively small as compared to the confinement energies. In general, all band profiles are very similar for both dot shapes, in agreement with the results in Chapter 6.

To show the variation in the band profile for the lens-shaped dots in more detail, it is plotted in Figure 7.4 along the [001] growth direction for several ARs. The overall variation in the band profile does not exceed 100 meV. The band profile for the lens shape becomes more homogeneous (and hence more similar to the ellipsoidal shape) with increasing AR. One can also notice that the heavy-hole band within the dot moves up in energy with increasing AR, while the light-hole energy within the dot is almost unchanged. The split-off valence band is also shown as an illustration. Within the dot, it moves down in energy with increasing AR, resulting in almost vanishing confinement potential at AR=8.

Note that Figure 7.4(b) shows the band profile for AR=3.5. The calculations for this specific AR value are performed in order to facilitate comparison with Ref. [1], in which the band structure was modelled for a variety of lens-shaped QD systems with AR≈3.5. The results obtained and those from Ref. [1] (indicated by arrows in Figure 7.4(b)) are in excellent agreement.

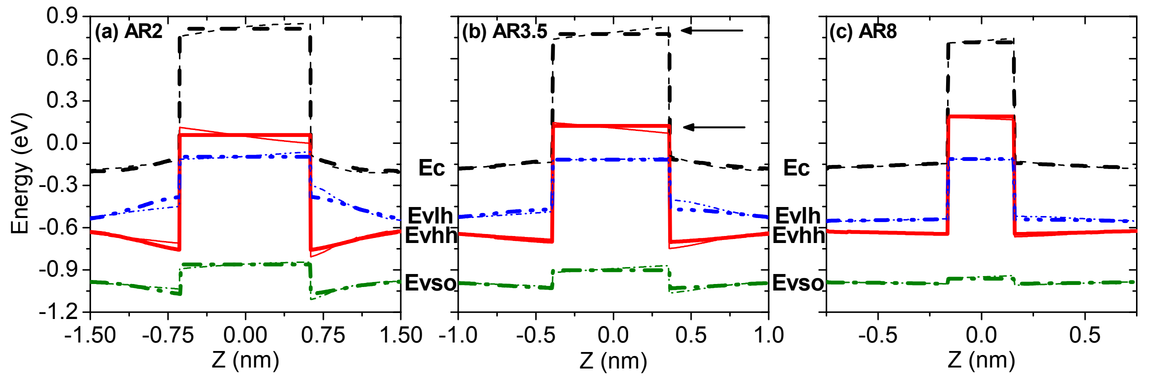

Figure 7.4 : Strain-modified band profiles along the [001] growth direction through the dot centre for ellipsoidal (thick lines) and lens(thin lines) SAQD shapes: Dashed line – conduction band, solid line – heavy-hole band, dash-dot-dot line – light-hole band, dash-dot line – split-off valence band. (a) AR=2; (b) AR=3.5; (c) AR=8. Short arrowhead lines in Fig. 4(b) indicate the averaged band-edge energies from Ref. 1 for lens-shaped dots of AR≈3.5.

Another important structural parameter of SAQDs is the dot composition. Now, we examine how the dot composition affects the strain-modified band profile, as even nominally pure InSb SAQDs may contain a significant percentage of As. Figure 7.5 shows the band profiles in $InAs_xSb_{(1-x)}$/InAs dot of ellipsoidal shape and AR=2 for several compositions.

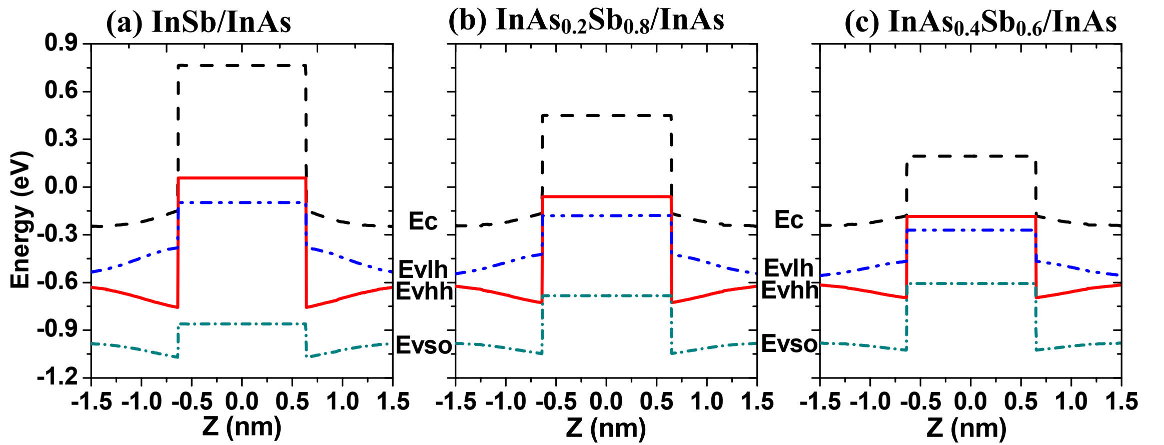

Figure 7.5 : Strain-modified band profile for alloyed ellipsoidal $InAs_xSb_{1-x}$/InAs SAQDs of AR = 2 for several As compositions. Dashed line – conduction band, solid line – heavy-hole band, dash-dot-dot line – light-hole band, dash-dot line – split-off valence band. (a) InSb/InAs; (b) $InAs_{0.2}Sb_{0.8}$/InAs; (c) $InAs_{0.4}Sb_{0.6}$/InAs.

For simplicity, a homogeneous composition profile within the dot is assumed and we neglect segregation into the matrix. The conduction band edge in the dot shifts in energy with As composition, but this does not affect the ground electron state as it is

not confined in the dot. However, the effect on the valence band is enormous. Both heavy- and light-hole bands move down in energy as the As percentage increases, significantly reducing the confinement potential. Note that the split-off valence band demonstrates an opposite trend. It moves up in energy as the percentage of As increases, inducing a deeper confinement.

7.2 ENERGY LEVELS

So far, the effects of the structural parameters on the band profiles are discussed, which are size independent in the continuum-elasticity approximation. Now, we proceed to examining the single-particle electron and hole states, which are (of course) size-dependent. In these calculations, a fixed value of the dot base size of 2.5 nm is used; i.e. varying the AR implies varying the dot height. Note that the base size is the only structural parameter of (very small) InSb/InAs SAQDs that can be experimentally measured with a meaningful accuracy, and the value of 2.5 nm is close to experimental data reported in the literature [5-7]. The electronic states are modelled only for the ellipsoidal dot because from the calculated band profile, the effect of shape is expected to be insignificant.

Figure 7.6(a) shows the single particle electron and hole energy levels at 80K as a function of the AR. Positions of the valence-band edges are also shown for reference. The position of the electron level almost remains constant. The heavy-hole band edge in the dot moves up in energy with AR. However, the size-quantised hole level demonstrates the opposite trend; the level is pushed down, toward the heavy-hole band edge in the matrix, with increasing AR. This demonstrates a dominating contribution from the size-quantisation effect due to decreasing dot height.

The hole level is below the ground electron state for dots of 2.5 nm base, despite the broken-gap alignment for the band edges. The ground state optical transition is due to recombination of weakly bound electrons in the matrix around the dot and holes strongly localized in the dot. Figure 7.6(b) shows the transition energies as a function of AR; results for both 80K and 300K were obtained for comparison with experimental data [5,6]. The transition energy increases with increasing AR.

Note that the hole level in the dot is lower in energy than the electron level in the matrix because of large size-quantisation energy for holes (up to the dot size of 3.5 nm in diameter). This is intrinsically related to the small size of the dot (indeed for AR=1, the transition energy is expected to be as small as 100 meV); this may explain why no PL was observed from InSb/InAs dot of larger sizes as reported in Ref. [7].

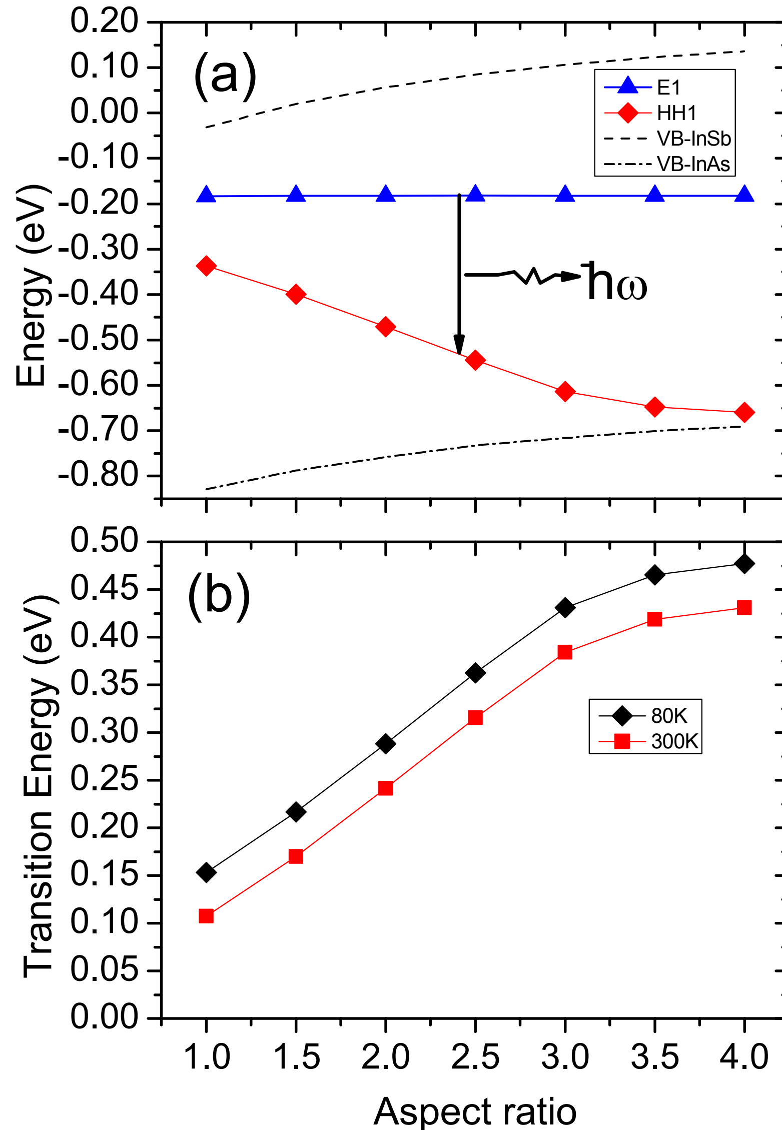

Figure 7.6 : (a) Single-particle electron and hole energy levels (triangles and diamonds, respectively) as a function of the aspect ratio for pure InSb/InAs ellipsoidal SAQDs at 80K. Dashed and dash-dot lines are InSb and InAs valence-band edges, respectively, shown for reference. (b) Ground-state transition energies at 80K and 300K (diamonds and squares, respectively). Symbols represent calculated results; solid lines are guides for the eye.

For alloyed $InAs_xSb_{(1-x)}$/InAs QDs, we have performed calculations for a fixed AR=2, i.e. the base is 2.5nm and the height is 1.25nm. The single-particle energy levels as well as the transition energies are shown in Figure 7.7 as a function of As

composition. As shown in Figure 7.7(a), the electron level remains constant and the heavy-hole level moves down in energy following the band edge position. Figure 7.7(b) shows how the transition energy increases with increasing As composition.

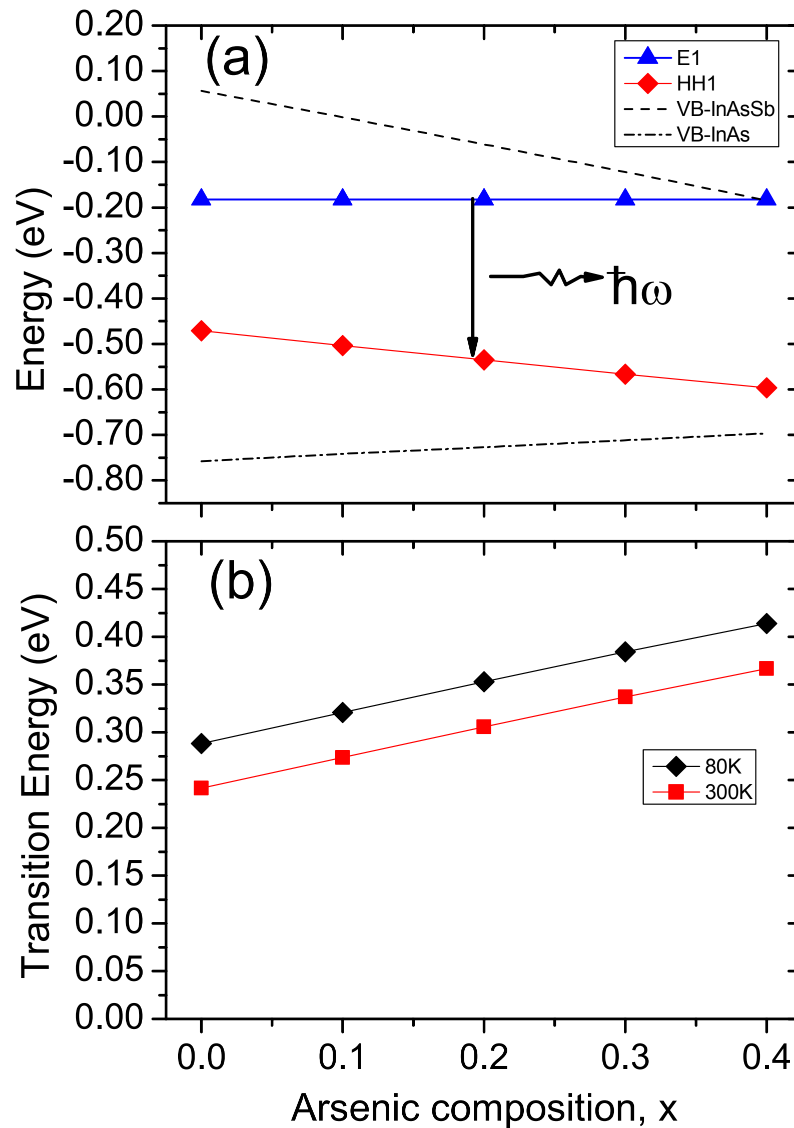

Figure 7.7 : (a) Single-particle electron and hole energy levels (triangles and diamonds, respectively) as a function of composition x for $InAs_xSb_{1-x}$/InAs ellipsoidal SAQDs of AR = 2 at 80K. Dashed and dash-dot lines are InSb and InAs valence-band edges, respectively, shown for reference. (b) Ground-state transition energies at 80K and 300K (diamonds and squares, respectively). Symbols represent calculated results; solid lines are guides for the eye.

Now, we are in the position to illustrate how the structural parameters of the dots can be assessed from the optical data. For this, we compare our results with the reported experimental data. References [5,6] report PL from several InSb/InAs SAQD samples. At 80K, the PL peaks are in the range of 0.33-0.36 eV. All samples exhibit

bright PL at temperatures up to 300K, red shifted to the range of 0.29-0.32 eV. The red shift is ≈ 40 meV, which agrees well with the value of ≈ 45 meV obtained from our calculations.

If we assume that the dots are pure InSb and the average lateral size is 2.5 nm [5,6], the dot has to have an AR of 2.3-2.6 for the transitions to be within the reported range. As an example, the AR of ≈ 2.5 is needed for the transition energy of 0.34 eV at 80K (and of 0.30 eV at 300K), as indicated by a downward arrow in Figure 7.6. On the other hand, if we find somehow that for the same dots, the AR = 2 (rather than 2.5), we should expect a significant As alloying. In this case, the dot would be expected to contain as much as 20% of As, indicated by a downward arrow in Figure 7.7.

Although only ground-state transitions from InSb/InAs SAQDs have been reported, [5,6] it is worth mentioning that excited states for holes are also expected in this system from our calculations. For the considered AR range, at least one excited hole state is expected. The separation between the levels should be about 140 meV. Separation between first and second excited states is found to be smaller, about 40 meV. For alloy $InAs_xSb_{(1-x)}$/InAs SAQDs with AR=2, at least three excited states are expected.

Finally, we would like to comment on relationship between PL intensity and dot size for this SAQD system, which originates from the type-II band alignment. Penetration of the electron wavefunction into the dot and hence the overlap integral are strongly limited by the dot size, similarly to W-type quantum well structures. [4] Thus the oscillator strength for the PL transition is expected to decrease dramatically with increasing dot size. Indeed, our estimates show that the oscillator strength drops by more then an order of magnitude if the dot size increases from 2.5 to 10 nm. This provides another reason for the observed quenching of PL from larger InSb/InAs dots. [7]

The integrated intensity of the InSb-related PL peak at 300K is reported to be about 15-20 times lower than that at 80K. This is in agreement with deep localization of holes in the dot; in addition, it indicates a relatively low level of non-radiative recombination.

7.3 EXPERIMENTAL RESULTS

As mentioned earlier in Section 4.3 in Chapter 4, one of the aims of the project was to study the optical properties of this SAQD samples using experimental techniques by means of PL spectroscopy. This allowed us to study the $InAs_xSb_{(1-x)}$/InAs SAQD not only on the theoretical side but also experimental side. In this experimental study, both power and temperature dependent PL were performed.

The PL obtained from the three InSb/InAs SAQD samples under similar excitation power conditions (20 mW) at 77K and 300K are shown in Figure 7.8. The PL spectra show that the dots luminescence are in the 0.34-0.39 eV range at 77K and red-shifted to 0.30-0.34 eV at 300K. The emission band of InSb dot from both A0160 and A0224 are about 2 orders of magnitude stronger than the InAs barrier emission at 77K; while the emission band from both the dot and barrier are comparable for A0150 sample. As a result, the InSb peak is clearly identified for both A0160 and A0150 at 300K. On the other hand, the PL from InSb dot appears as a shoulder to InAs barrier for A0150.

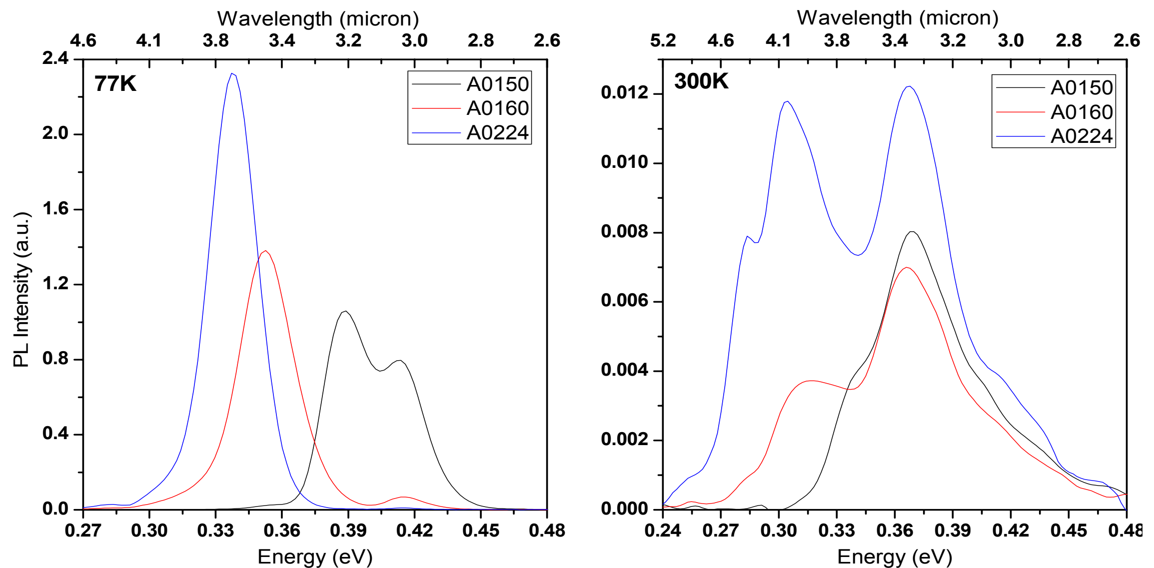

Figure 7.8 : PL spectra of the InSb/InAs SAQDs samples at 77K and 300K.

We have studied the luminescence of the samples as a function of varying excitation power and temperature in more detail. The PL spectra are dominated by a low-energy peak which is attributed to the emission of InSb dot.

7.3.1 Power Dependent PL

For power dependent PL, the temperature is kept at liquid nitrogen temperature and the excitation power is varied from 10 mW up to 90 mW. The peak energy of the dot emission band is found to shift to higher energy as the excitation power is increased from 10mW to 90mW. The PL peak energies of the dot emission band from all samples as a function of excitation power are shown in Figure 7.9.

The peak energy of the A0224 dot emission band is found to shift to higher energy by ~5 meV as the excitation power increased from 10mW to 90mW. A0160 shows similar behaviour to A0224 but the InSb dot peak energies is found to shift to higher energy by ~3 meV. A0150 shows a slightly different behaviour to that of A0160 and A0224 at high excitation power. The peak energy of the dot emission band for A0150 is found shift to higher energy up to 80mW excitation power and the peak energy started to shift to lower energy from 80 mW to 90 mW. The overall InSb dot peak energies shift is only around 1 meV for A0150.

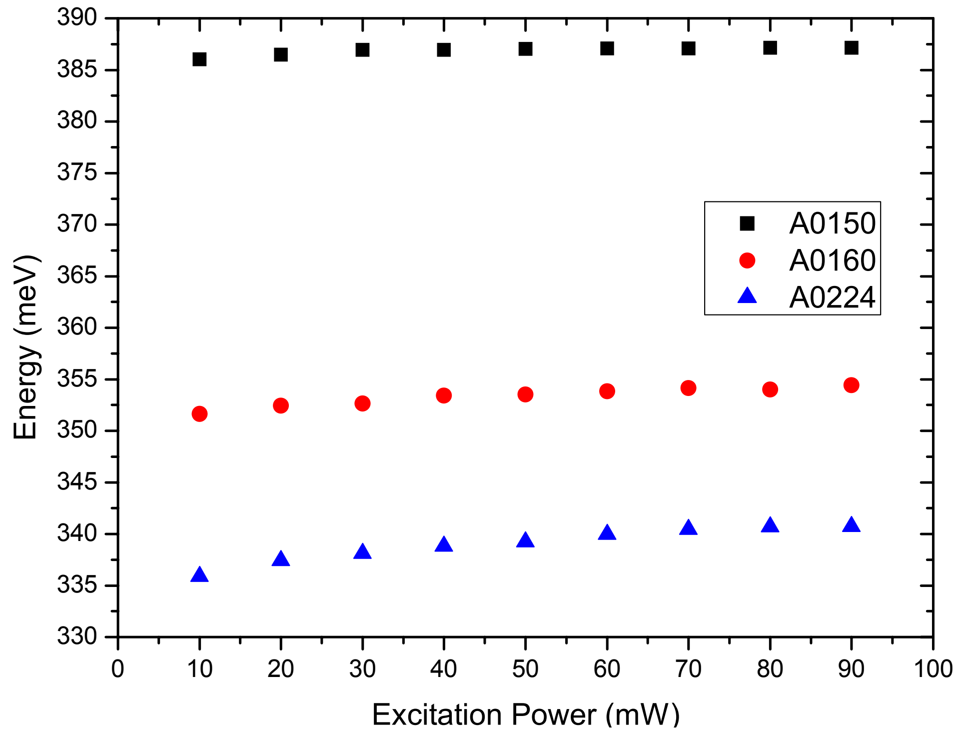

Figure 7.9 : The peak energies of the dot emission bands from A0150, A0160, and A0224 QD samples as a function of excitation power at 77K.

The shift of PL peak to higher energy as a function of increasing excitation power is consistent with a type-II band alignment with electrons and holes separated in real space [9]. Similar behaviour is also being observed for Ge/Si [10] QDs system. In

both QD systems, the holes are confined in the dots while electrons are confined outside. Since more electrons and holes are supplied at higher excitation powers, the electrons and holes will be at higher energy [11].

A strong increase in PL intensity with increasing excitation power can also be observed for both A0160 and A0224; and saturation of the PL peaks is not observed up to the maximum excitation power of the diode laser used. In contrast, the dot PL intensity for A0150 shows weak dependent on the excitation power and the intensity is seem to be saturated around 80-90 mW as shown in Figure 7.10.

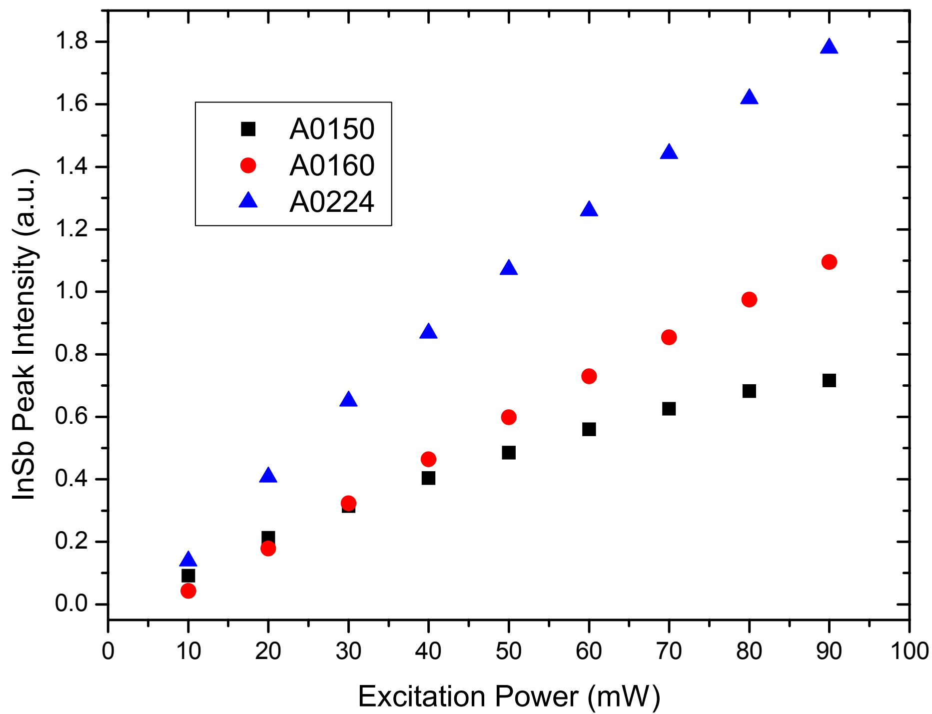

Figure 7.10 : The InSb peak intensity as a function of excitation power at 77K.

7.3.2 Temperature Dependent PL

Next, the result of the temperature dependent PL of the InSb/InAs samples is presented. PL spectra were measured under the diode laser excitation (785 nm) at 20 mW for temperature dependent PL.

Figure 7.11 shows the temperature dependent PL spectra of the samples. All peaks are red shifted with increasing temperature. An increase in temperature results in a dilatation of the lattice, a change in the band gap following the Varshni law [12], and consequently in a decrease of the PL transition energy.

In order to examine the variation with temperature of the QD transition energy, the QD peak energy from the PL measurement and the transition energy obtained from the theoretical modelling are plotted against temperature as shown in Figure 7.11. We can deduce that the ARs of the samples are 2.7, 2.5 and 2.4 respectively for A0150, A0160 and A0224; which corresponds to the dot height of 0.9nm, 1.0nm and 1.1nm, respectively. On the other hand, by assuming the AR of the dots for all samples is 2 and the As composition in dot is varied to fit the experimental data. The results show that A0150 grown at high temperature contains the most As (~30%), followed by A0160 (~22%), and A0224 contains the least As (~16%) according to the assumption of dot AR=2.

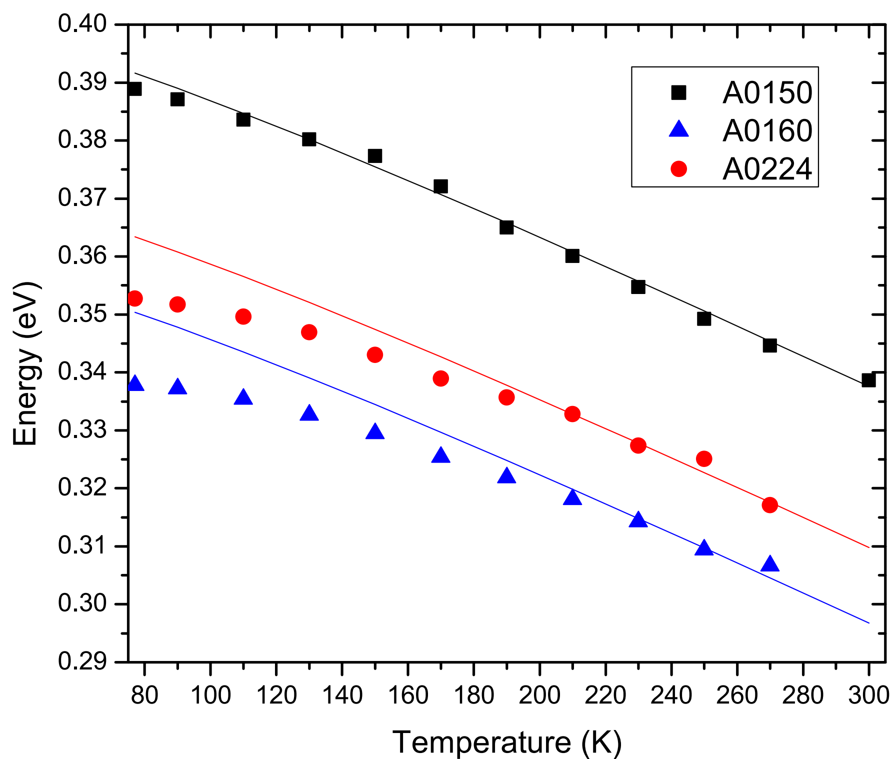

Figure 7.11 : Experimental and theoretical QD transition energy vs. temperature. The solid lines are modelling results according to Varshni law and the solid symbols represent the experimental data.

The QD transition energy obtained from theoretical modelling agree well with the result obtained from the PL measurement for A0150 for the whole temperature range studied. For both A0160 and A0224, the agreement is only for the temperature of 190–300K. This behaviour has been observed before for group III/V Sb family materials, such as GaAsSb and AlGaAsSb alloys, lattice matched to InP [13]. The behaviour has been related to the transitions of the localised defect states due to the variation in the alloy composition [13].

As outlined in the sample growth section, these InSb/InAs SAQD samples were grown by exploiting Sb-to-As anion exchange reaction at different substrate temperatures. A0150 was grown at a high temperature of 450 °C; this may leads to very efficient exchange reaction and homogeneous composition within the dot and the surrounding matrix. However, A0160 was grown at low substrate temperature of 345 °C and A0224 was grown using Sb-to-As anion exchange at 430 °C, followed by additional MEE deposition of 0.7 ML of InSb. The low substrate temperature may leads to insufficient Sb-to-As anion exchange reaction and caused the composition variation in sample A0160. The variation in composition may occur in sample A0224 during the additional MEE deposition of 0.7 ML of InSb after the high temperature Sb-to-As anion exchange reaction.

From the previous report [13], the discrepancy tends to decrease when the excitation density used to perform the temperature dependent PL is increased. Similar measurements as in Ref. [13] have been performed for sample A0224 and the results are plotted in Figure 7.12. As can be seen from the figure, the initial discrepancy of ~15 meV between the theoretical result and the experimental result for 9 mW excitation at 77K reduces to ~8 meV when the excitation power increases to 90 mW.

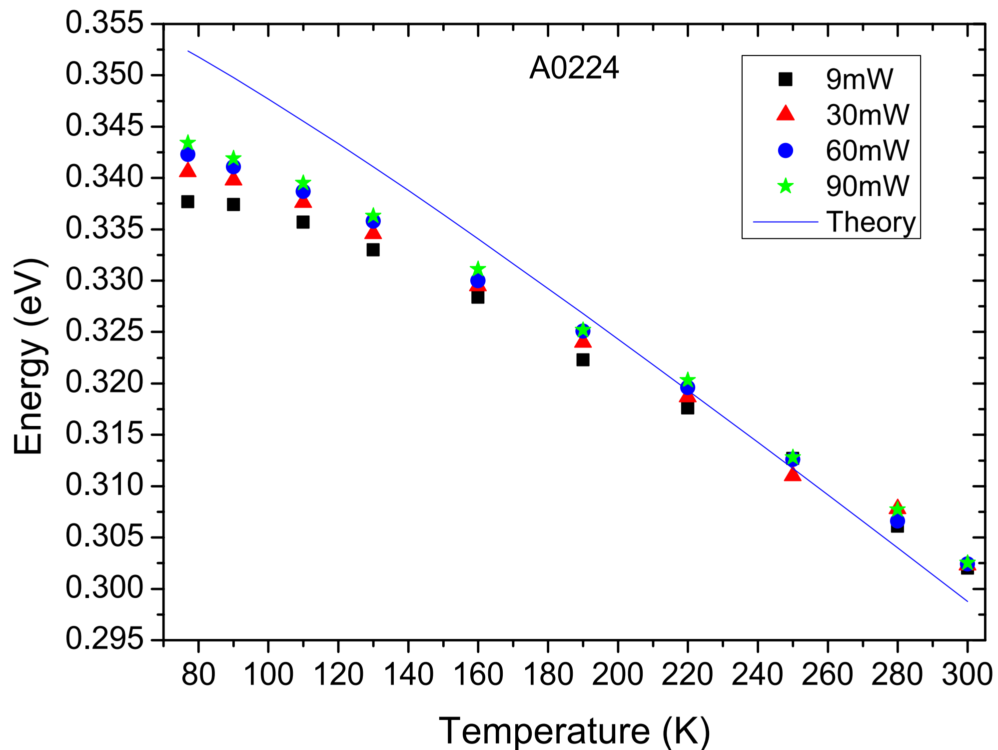

Figure 7.12 : Temperature dependent PL as a function of increasing excitation power.

In order to identify the mechanism of the PL quenching, the temperature dependence of the PL intensity was investigated by plotting the ratio between the dot emission peak and InAs peak as a function of inverse temperature as shown in Figure 7.13.

From Figure 7.13, the PL quenching is the smallest for A0150 with less than one order of magnitude, followed by A0160 with the quenching of less than two order of magnitude. The PL quenching is the highest for A0224 with the quenching of more than two orders of magnitude.

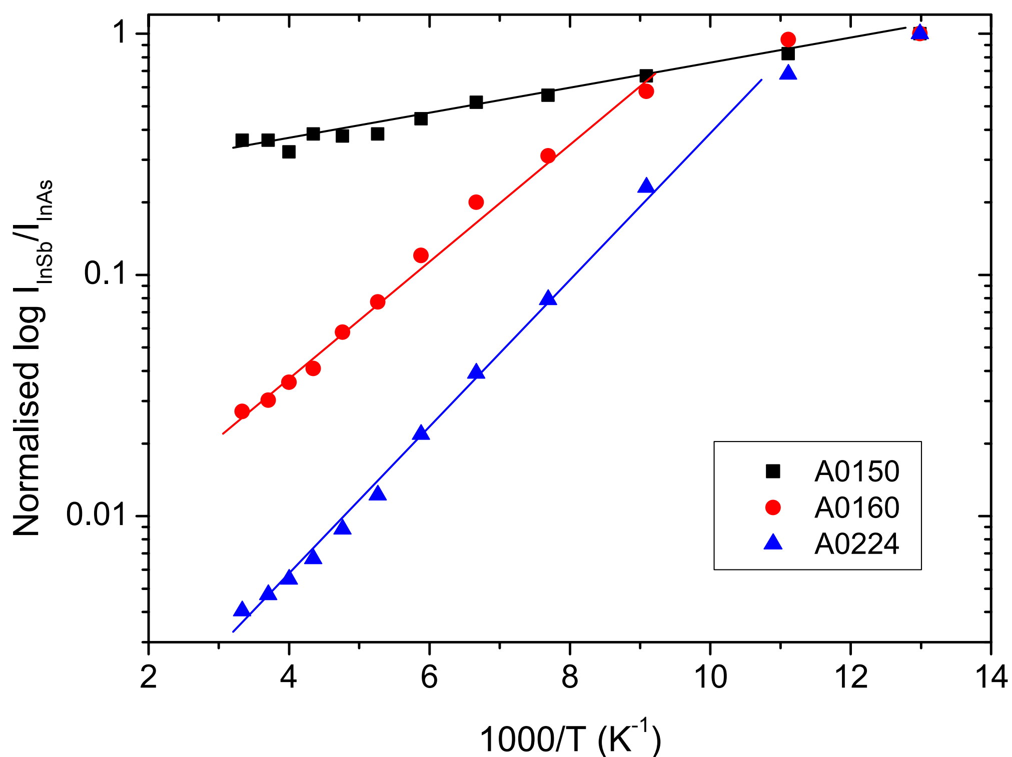

Figure 7.12 : Normalised log PL intensity of InSb/InAs SAQDs samples as a function of the inverse temperature.

The thermal activation energies for the samples have been estimated by determining the gradient of the fitting lines as shown in Figure 7.12. It was found that the activation energy also has a size-dependent behaviour. It was found that the larger dot size has a larger activation energy. The activation energies are 31 meV, 41 meV, and 60 meV, respectively for A0150, A0160 and A0224. In these samples, the energy different between the PL peak energy of the dot and the barrier band gap are 24 meV, 62 meV, and 77 meV for A0150, A0160 and A0224.

We can clearly see that the different between the PL peak energy of the dot and the band gap of barrier under investigation is close to the obtained activation energy. It is apparent that the PL quenching follows the commonly accepted interpretation, in which the charge carrier escapes from the confined states into the barriers followed by a nonradiative recombination.

7.4 SUMMARY

We have modelled the electronic structure of $InAs_xSb_{(1-x)}$/InAs SAQDs of various shapes, aspect ratios and compositions using strain-dependent multi-band ***k·p*** theory. $InAs_xSb_{(1-x)}$/InAs SAQDs exhibit a type-II broken-gap alignment. Our analysis shows that strong confinement exists for holes only, with electrons loosely bound around the dot. The hole confinement potential is not sensitive to details of the dot shape and is essentially defined only by the dot AR.

With increasing AR, strain-induced splitting of valence band increases, and a deeper confinement is formed. However, for a fixed lateral size, the optical transition energy increases with the aspect ratio, resulting from dominating contribution from the size-quantisation effect. Effect of variation in the dot composition is comparable to the effect of the aspect ratio on the hole levels. Hence, $InAs_xSb_{(1-x)}$/InAs SAQD system provides wide possibilities of band-gap engineering in the mid-infrared range.

Our calculations show that structural parameters of the dots can be estimated using the optical spectra.

The PL measurement shows that the dots luminescence are in the 0.34-0.39 eV range at 77K and red-shifted to 0.30-0.34 eV at 300K. The QD transition energy obtained from theoretical modelling agree well with the result obtained from the temperature dependent PL measurement for A0150 for the whole temperature range studied. For both A0160 and A0224, the agreement is only for the temperature of 190–300K. This may due to the transitions of the localised defect states due to the variation in the composition. However, the discrepancy decreases when the excitation density used to perform the temperature dependent PL is increased.

The different between the PL peak energy of the dot and the band gap of barrier

under investigation is close to the obtained activation energy. This shows that the PL quenching follows the commonly accepted interpretation, in which the charge carrier escapes from the confined states into the barriers followed by a nonradiative recombination

References:

[1] C. E. Pryor and M. -E. Pistol, Phys. Rev. B **72**, 205311 (2005).

[2] S. I. Rybchenko, G. H. Yeap, R. Gupta, I. E. Itskevich, and S. K. Haywood, *8th International Conference on Mid-Infrared Optoelectronics: Materials and Devices*, Bad Ischl, 2007 (unpublished).

[3] S. I. Rybchenko, R. Gupta, K. T. Lai, I. E. Itskevich, S. K. Haywood, V. Tasco, N. Deguffroy, A. N. Baranov, and E. Tournié, Phys. Rev. B **76**, 193309 (2007).

[4] J. R. Meyer, C. A. Hoffman, F. J. Bartoli, and L. R. Ram-Mohan, Appl. Phys. Lett. **67**, 757 (1995).

[5] S. V. Ivanov, A. N. Semenov, V. A. Solov'ev, O. G. Lyublinskaya, Ya. V. Terent'ev, B. Ya. Meltser, L. G. Prokopova, A. A. Sitnikova, A. A. Usikova, A. A. Toropov, and P. S. Kop'ev, J. Cryst. Growth **278**, 72 (2005).

[6] V. A. Solov'ev, O. G. Lyublinskaya, A. N. Semenov, B. Ya. Meltser, D. D. Solnyshkov, Ya. V. Terent'ev, L. A. Prokopova, A. A. Toropov, S. V. Ivanov, and P. S. Kop'ev, Appl. Phys. Lett. **86**, 011109 (2005).

[7] O. G. Lyublinskaya, V. A. Solov'ev, A. N. Semenov, B. Ya. Meltser, Ya. V. Terent'ev, L. A. Prokopova, A. A. Toropov, A. A. Sitnikova, O. V. Rykhova, and S. V. Ivanov, J. Appl. Phys. **99**, 093517 (2006).

[8] I. Vurgaftman, L. R. Ram-Mohan and J. R. Meyer, J. Appl. Phys. **89**, 5815 (2001).

[9] E. R. Glaser, B. R. Bennett, B. V. Shanabrook, and R. Magno, Appl. Phys. Lett. **68**, 3614 (1996).

[10] M. C. Kim, K. I.Han, S. Kim, S. –H. Choi, C. J. Park, H. T. Oh, and H. Y. Cho, J. Korean Phys. Soc. **48**, 1342 (2006).

[11] T. Baier, U. Mantz, K. Thonke, R. Sauer, F. Schaffler, and H. –J. Herzog, Phys. Rev. B **50**, 15191 (1994).

[12] Y. P. Varshni, Physica **34**, 149 (1967).

[13] D. O. Toginho Filho, I. F. L. Dias, E. Laureto, J. L. Duarte, S. A. Lourenço, L. C. Poças, S. S. Prabhu, and J. Klem, J. Appl. Phys. **97**, 123702 (2005).

CHAPTER 8

CONCLUSIONS
AND
FUTURE DEVELOPMENT OF THE MODEL

8.1 CONCLUSIONS

The InSb/GaSb conical and truncated conical SAQD heterostructures are analysed using 2-D axial symmetry using ANSYS and both 2-D and 3-D models using Comsol Multiphysics. Both packages provided results in very good agreement but Comsol Multiphysics is more powerful and preferable because it can be used in parallel with Matlab to perform band structure calculations. Though the 2-D model provides good approximation and satisfactory results but it may overlooked the symmetry property of zinc-blende crystal structure. On the other hand, 3-D model allows strain in any arbitrary plane through the model to be obtained easily. However, the 3-D model is sensitive to finite element meshing especially near the edges of the dot-matrix interface.

Due to the lattice mismatch, there is a tensile strain in the matrix just below and above the dot and compressive strain in the dot in xx- and yy-direction and the other way round in the zz-direction. There are various factors that may affect the strain distribution such as, height of the cap layer, the shape of the dot and the aspect ratio of the dot but only the shape and aspect ratio of the dot had been investigated.

We have examined the effect of the SAQD shape and AR on the strain-modified quantisation potential. For this purpose, the band profile was calculated for the InAs/GaAs (100) system for a number of realistic dot shapes. The most important features of the quantisation potential were analysed, and their variation with the dot geometry was examined. The underlying variations in the characteristic strain components within the SAQD were revealed. As a result, the AR was suggested as a governing geometric parameter of the SAQD shape. This was used to justify approximation of the SAQD shape by an ellipsoid, which is expected to be valid for a wide range of III-V zinc-blende SAQD systems. The conduction band moving down while valence band moving up in the energy colour scale with increasing AR; in other word, the band gap of InSb dot reduces with increasing aspect ratio. Effects from

incorporation of the wetting layer and from the growth plane orientation have been also analysed.

For the ellipsoidal shape, reproducibility of the quantisation potential was analysed using different approximations for the elastic problem. It was shown that most essential features of the quantisation potential are well reproduced in the isotropic elasticity approximation, provided the effective elastic moduli are selected according to orientation of the growth plane. This result is particularly important because the isotropic approximation allows a simple analytical solution of the elastic problem for an ellipsoidal QD. On the other hand, it was shown that further simplification of the elastic problem (such as the Similar-Elasticity approximation) results in a strain profile which is different both qualitatively and quantitatively. As a result, it reproduces the quantisation potential with significant distortion.

We have modelled the electronic structure of InSb/GaSb and $InAs_xSb_{1-x}$/InAs SAQDs of various shapes, aspect ratios and compositions using strain-dependent multi-band $\boldsymbol{k}\cdot\boldsymbol{p}$ theory. InSb/GaSb SAQDs is a type-I system with strong confinement exist for electrons and only weak confinement for hole. Our analysis shows that the hydrostatic strain lifted the Γ-conduction band inside the dot to higher energy and becomes close to the conduction band edge of the matrix. The shear strain split the valence band in the matrix near the heterointerface into heavy- and light-hole bands. This creates a "shell" feature around the dot because both the light- and heavy-hole bands within the dot are much shallower than the light-hole band in the matrix. This "shell" feature provides a potential minima in which holes tend to localised for the dot of low AR.

Also, the strain effect causing the crossover of the Γ- and L-conduction bands in the matrix. For all shapes, the L-band edges are far below the Γ-band edge. Therefore the L-band provides local potential minima for electrons.

These theoretical observations are confirmed by the PL measurements and hence the objective in obtaining MIR emission from InSb/GaSb SAQDs is achieved. The deep localisation of the electron states in the L-band give rises to the high temperature stability of the PL emission. Despite high density, excellent structural quality of the dot

and temperature stability, the dots are not suitable for device application because the overall PL intensity is very low.

$InAs_xSb_{1-x}/InAs$ SAQDs exhibit a type-II broken-gap alignment. Our analysis shows that strong confinement exists for holes only, with electrons loosely bound around the dot. The hole confinement potential is not sensitive to details of the dot shape and is essentially defined only by the dot aspect ratio.

With increasing aspect ratio, strain-induced splitting of valence band increases, and a deeper confinement is formed. However, for a fixed lateral size, the optical transition energy increases with the aspect ratio, resulting from dominating contribution from the size-quantisation effect. Effect of variation in the dot composition is comparable to the effect of the aspect ratio on the hole levels. Hence, InAsSb/InAs SAQD system provides wide possibilities of band-gap engineering in the mid-infrared range.

Our calculations show that structural parameters of the dots can be estimated using the optical spectra. Indeed, from the PL studies of three $InAs_xSb_{(1-x)}/InAs$ samples, we are able to deduce the AR of the samples if we assumed pure InSb dots and the composition of the samples if we assume some fixed AR of the dot. Nevertheless, these results are methodology or qualitative one as the reliable structural characterisation of these very small dots is not available up to now. This is due to the limitation of the TEM microscopy in detecting very small dots.

8.2 FUTURE DEVELOPMENT OF THE MODEL

There are several extensions to calculation of the strain distribution and electronic structure in SAQDs that may be possible. Piezoelectric effects induced by shear component of strains could be determined as this will affect the confining potential. Further investigations of other affecting factors on strain distribution such as the height of capping layer also may be performed as well as coupled and stacked QD structures.

Another useful approach to perform these calculations is the atomistic approach that based on the valence force field that account for coupling between bending and stretching in adjacent bonds, bond twisting and non-bonded interactions in order to

improve the accuracy of the model as the III-V semiconductors displays covalent bonding with only limited charge transfer. However, this approach only useful when fine feature of the dot, such geometry and size is known very accurately.

In order to use Sb-based SAQDs in the MIR 3-5 μm range, there are still a few designs can be considered. Designs that utilising type-I band alignment are also possible. These include dot-in-well (DWELL) structure and dilute-nitride materials.

DWELL structures can be achieved by incorporating strain reducing layer (SRL) such as AlInAs [1], InGaAs [1,2], InGaAsSb [3], etc to the SAQDs heterostructures. The SRL will reduced the residual compressive strain in the dots and hence reduces the conduction band shift (i.e., reduce bang gap) and extend the wavelength. SRL also suppressed the generation of defects and dislocations, thereby enhancing the radiative recombination. Besides, improved size uniformity as well as increased in dot density also had been observed for SAQDs covered by the SRL [1,3].

The proposed ellipsoidal model in Chapter 4 can take into account a homogeneous external strain that can be used for DWELL structures modelling. The band gap of $InAs_{0.5}Sb_{0.5}$ SAQD in InP matrix is predicted to reduced from ~0.45 eV to ~0.30 eV by incorporating the $Al_{0.15}In_{0.85}As$ SRL for the dot with AR = 8 [4].

Incorporation of dilute concentrations of nitrogen to III-V semiconductors will drastically reduce the band gap of the semiconductors due to the strong negative band gap bowing effects [5-8]. A decrease in band gap of 110 meV has been predicted for dilute InSb:N at 1% of N [9]. In this case, a negative band gap can be achieved by incorporate higher N content to InSb as incorporation of as high as 10% of nitrogen is possible [9]. However, this may gives rise to the difficulty in controlling the growth process when high content of N to be added to the epilayer. A systematic theoretical and experimental investigation is needed to utilising this dilute nitride semiconductors.

References:

[1] Z. D. Fang, Z. Gong, Z. H. Miao, L. M. Kong, X. H. Xu, H. Q. Ni, and Z. C. Niu, J. Phys. D: Appl. Phys. **37**, 1012 (2004).

[2] Y.-M. Liu, Z.-Y. Yu, and X.-M. Ren, Chin. Phys. Lett. **25**, 1850 (2008).

[3] K. Akahane, N. Yamamoto, S.-I. Gozu, A. Ueta, and N. Ohtani, Physica E **32**, 81 (2006).

[4] S. I. Rybchenko, G. H. Yeap, R. Gupta, I. E. Itskevich, and S. K. Haywood, *8th International Conference on Mid-Infrared Optoelectronics: Materials and Devices*, Bad Ischl, 2007 (unpublished).

[5] J. N. Baillargeon, P. J. Pearah, K. Y. Cheng, G. E. Hofler, K. C. Hsieh, J. Vac. Sci. Technol. **B10**, 829 (1992).

[6] M. Weyers, M. Sato, and H. Ando, Jpn. J. Appl. Phys. **31**, L853 (1992).

[7] L. Bellaiche, Appl. Phys. Lett. **75**, 2578 (1999).

[8] M. Kondow, K. Uomi, A. Niwa, T. Kitatani, S. Watahiki, and Y. Yazawa, J. Vac. Sci. Technol. A **35**, 1273 (1996).

[9] T. Ashley, T. M. Burke, G. J. Pryce, A. R. Adams, A. Andreev, B. N. Murdin, E. P. O'Reilly, and C. R. Pidgeon, Solid-State Electronics **47**, 387 (2003).

Appendix 1 – Strain Tensor for Oblate Ellipsoid

These expressions are only valid in a coordinate system whose axes (x, y, z) are parallel to the principal axes (a, b, c) of the ellipsoid. The original solution for general ellipsoid is adopted for the case of oblate ellipsoid (a = b > c). [3] We keep the original notations for strain components and constants. The usual tensor index notation and summation rules are employed. The following notation is used for scalar f and deviatoric ${}^{/}f_{ij}$ parts of second-order tensor f_{ij}:

$$f_{ij} = {}^{/}f_{ij} + \tfrac{1}{3} f \delta_{ij}, \tag{1}$$

where $f = f_{mm}$ and ${}^{/}f_{ij} = f_{ij} - \tfrac{1}{3} f \delta_{ij}$.

a) Definition of material parameters and intermediate coefficients

Lattice mismatch (initial) strain,

$$e^{*}_{ij}:\ e^{*}_{11} = e^{*}_{22} = e^{*}_{33} = \frac{a_m - a_i}{a_i}, \text{ and } e^{*}_{i \neq j} = 0, \tag{2}$$

where a_m and a_i are lattice constants of matrix and inclusion (QD) materials respectively.

Elastic constants,

In the matrix – $\kappa, \mu,$

In the inclusion –κ_ι, μ_ι.

$$\sigma = \frac{3k - 2\mu}{2(3k + \mu)} \tag{3}$$

Intermediate coefficients are:

$$\begin{aligned}
&S_{1111} = S_{2222} = Qa^2 I_{aa} + RI_a, \quad && S_{2233} = Qc^2 I_{ac} - RI_a, \\
&S_{1122} = S_{2211} = Qa^2 I_{ab} - RI_a, \quad && S_{3333} = Qc^2 I_{cc} + RI_c, \\
&S_{1133} = Qc^2 I_{ac} - RI_a, \quad && S_{3311} = S_{3322} = Qa^2 I_{ac} - RI_c, \\
&S_{1212} = Qa^2 I_{ab} + RI_a, && \\
&S_{1313} = S_{2323} = \tfrac{1}{2} Q(a^2 + c^2) I_{ac} + \tfrac{1}{2} R(I_a + I_c) &&
\end{aligned} \tag{4}$$

where

$$Q = \frac{3}{8\pi(1-\sigma)}, \quad R = \frac{1-2\sigma}{8\pi(1-\sigma)},$$

$$I_a = \frac{2\pi a^2 c}{(a^2 - c^2)^{3/2}} \left\{ \arccos\left(\frac{c}{a}\right) - \frac{c}{a}\left(1 - \frac{c^2}{a^2}\right)^{1/2} \right\},$$

$$I_c = 4\pi - 2I_a, \; I_{ac} = \frac{I_c - I_a}{3(a^2 - c^2)}, \; I_{cc} = \frac{4\pi}{3c^2} - 2I_{ac},$$

$$I_{aa} = \frac{4\pi}{3a^2} - I_{ab} - I_{ac}, \quad I_{ab} = \tfrac{1}{3} I_{aa}. \tag{5}$$

b) Strain components inside the inclusion (QD)

For the orientation of the ellipsoid employed with the (001) growth plane, only diagonal components of strain tensor $e_{ij}{}^{T}$ are nonzero inside the QD:

$$e_{11}^{T} = e_{22}^{T} = -\frac{E}{D} e_{33}^{T}, \quad e_{33}^{T} = \frac{3e^{*}CD}{AE - BD}, \tag{6}$$

where

$$A = 2\frac{\mu}{\mu - \mu_i} + 6S_{3311} - 2\frac{k}{k - k_i},$$

$$B = -2\frac{\mu}{\mu - \mu_i} + 3S_{3333} - \frac{k}{k - k_i},$$

$$C = \frac{k}{k - k_i},$$

$$D = S_{1111} + S_{1122} - 2S_{3311} - \frac{\mu}{\mu - \mu_i},$$

$$E = S_{1133} - S_{3333} + \frac{\mu}{\mu - \mu_i}. \tag{7}$$

c) Strain in the matrix at heterointerface

The components of strain tensor $e_{ij}^{C}(out)$ in matrix just near the interface can be found from their values $e_{ij}^{C}(in) \,/\, e_{ij}^{T}$ at an adjacent point inside the inclusion by using the following expressions: [3]

$$e^{C}(out) = e^{C}(in) - \tfrac{1}{3}\frac{1+\sigma}{1-\sigma} e^{T} - \frac{1-2\sigma}{1-\sigma}{}' e_{ij}^{T} n_i n_j, \text{ and}$$

$$ {}^{/}e_{ij}^{C}(out) = {}^{/}e_{ij}^{C}(in) + \frac{1}{1-\sigma}{}^{/}e_{jk}^{T} n_j n_k n_i n_l - {}^{/}e_{ik}^{T} n_k n_l - {}^{/}e_{lk}^{T} n_k n_i + \frac{1-2\sigma}{3(1-\sigma)}{}^{/}e_{jk}^{T} n_j n_k \delta_{il} - \tfrac{1}{3}\frac{1+\sigma}{1-\sigma} e^{T}(n_i n_l - \tfrac{1}{3}\delta_{il}) \quad (8) $$

where n_i are components of the normal to the ellipsoid surface at the point (x, y, z):

$$ n_1 = \frac{x}{a^2 h}, \quad n_2 = \frac{y}{b^2 h}, \quad n_3 = \frac{z}{c^2 h}, \quad h = \left(\frac{x^2}{a^4} + \frac{y^2}{b^4} + \frac{z^2}{c^4} \right)^{1/2}. \quad (9) $$

The relation between the constrained and stress-free strains in the inclusion is in the form,

$$ e_{il}^{C} = S_{ilmn} e_{mn}^{T} \quad (10) $$

Appendix 2 – List of Publications and Conference Presentations

Peer reviewed journals:

1. G. H. Yeap, S. I. Rybchenko, I. E. Itskevich, and S. K. Haywood, *Type–II $InAs_xSb_{(1-x)}$/InAs quantum dots for mid-infrared applications: Effect of morphology and composition on electronic and optical properties*, Phys. Rev. B **79**, 075305 (2009).

2. S. I. Rybchenko, G. Yeap, R. Gupta, I. E. Itskevich, and S. K. Haywood, *Importance of aspect ratio over shape in determining the quantization potential of self-assembled zinc-blende III-V quantum dots*, J. Appl. Phys. **102**, 013706 (2007).

Conference presentations:

1. G. H. Yeap, S. I. Rybchenko, R. Gupta, I. E. Itskevich and S. K. Haywood, *Multi-band **k·p** Calculations for Valence Band Structure of Strained Type-II InSb/InAs Quantum Dots*, Theory, Modelling and Computational Methods for Semiconductor Materials and Nanostructures (TMCS), University of Manchester, 31st Jan 2008. (Poster presentation)

2. G. H. Yeap, S. I. Rybchenko, R. Gupta, I. E. Itskevich and S. K. Haywood, *Valence Band Structure of Strained Type-II InSb/InAs Quantum Dots: A Multi-Band **k·p** Study*, One Day Quantum Dot Meeting, Imperial College London, 11th Jan 2008. (Poster presentation)

3. G. H. Yeap, S. I. Rybchenko, R. Gupta, I. E. Itskevich and S. K. Haywood, *Type-II InSb/InAs Quantum Dots for Mid-Infrared: Effect of Geometry and Composition on Electronic Structure*, Compound Semiconductor 2007 (CSUK 2007), Sheffield, 4th-5th July 2007. (Oral presentation)

4. S. I. Rychenko, G. H. Yeap, R. Gupta, I. E. Itskevich and S. K. Haywood, *Effect of geometry on quantization potential in compressively strained zinc-blende III-V quantum dots*, 8th International Conference on the Mid-Infrared Optoelectronics: Materials and Devices (MIOMD-VIII), Bad Ischl, Austria, 14th-16th May 2007. (Poster presentation)